

DISSERTATION

CONTINUOUS-WAVE CAVITY RING DOWN SPECTROSCOPY  
SENSOR FOR HALL THRUSTER EROSION MEASUREMENT

Submitted by

Lei Tao

Department of Mechanical Engineering

In Partial Fulfillment of the Requirements

For the Degree of Doctor of Philosophy

Colorado State University

Fort Collins, Colorado

Spring 2011

Doctoral Committee:

Advisor : Azer P. Yalin

Anthony J. Marchese

Carmen S. Menoni

John D. Williams

## ABSTRACT

### CONTINUOUS-WAVE CAVITY RING DOWN SPECTROSCOPY SENSOR FOR HALL THRUSTER EROSION MEASUREMENT

Hall thruster and other Electric propulsion (EP) devices have become appealing alternatives to traditional chemical propulsion thrusters for space applications due to this high specific impulse ( $I_{sp}$ ), which allows high fuel efficiency. However, the uncertainty of the lifetime for Hall thruster hinders its development in future applications requiring a long operational time (several thousands of hours). Sputter erosion of boron nitride (BN) acceleration channel wall is principal lifetime limitation for Hall thrusters. The sputtered particles can redeposit causing a critical contamination effect. There is an urgent need for improved experimental tools to understand the BN sputter erosion process and lifetime assessment for Hall thrusters. The present research applies continuous wave cavity ring down Spectroscopy (CW-CRDS) as a diagnostic tools to study the sputter erosion process for Hall thrusters.

Two CW-CRDS erosion sensors have been developed for *in situ* monitoring of sputtered manganese (Mn) and BN. As a stepping stone towards BN detection, a Mn erosion sensor was first developed. This sensor is based upon detection of Mn atoms via an absorption line from ground state at a wavelength of 403.076 nm. Measurements of sputtered Mn atom number

density and its hyperfine structure are presented. Additionally, end-point detection has been done for a multilayer target, which can be potentially applied to the industrial sputtering systems. The same system has also been applied for detecting eroded atoms from the acceleration channel wall in an anode layer type Hall thruster. The results show the validity of the CW-CRDS erosion sensor for Hall thruster lifetime estimation. A BN erosion sensor has also been developed for the detection of sputtered boron atoms from Hall thrusters by probing atomic absorption lines of boron (250 nm) with CW-CRDS. A photonic crystal fiber was used to couple the ultraviolet laser light to the cavity within the vacuum chamber. The experimental detection limits and signal-to-noise values show potential for Hall thruster BN erosion studies. Finally, the velocity distributions of sputtered boron atoms at different ion energies were measured with laser induced fluorescence (LIF). These velocity distribution are necessary for interpretation of signals from the BN erosion sensor.

## **ACKNOWLEDGEMENTS**

The path to a Ph.D. was a magnificent as well as challenging experience to me. In all these years, the support and contributions from many people have made this research possible. It is a great pleasure to thank who have helped me along the way.

First, I owe my deepest gratitude to my advisor Professor Azer Yalin for the knowledge and time he shared with me. He introduced me to the exciting world of laser diagnostic and showed me how to conduct a successful scientific research. This wonderful experience will accompany my whole life. It was only due to his constant support, valuable guidance and ever-friendly nature that I was able to complete my research work in a respectable manner.

Next, I would like to express my special thanks to Professor Naoji Yamamoto from Kyushu University, Japan. He helped me out in all aspects for the development of the laser diagnostic systems. He made it possible to conduct experiment with a real Hall thruster. I very much appreciate the knowledge he shared with me during the very delightful and fruitful collaboration.

I also want to thank Professor John Williams for invaluable discussions during my research. His generosity of sharing both knowledge and equipment

made my research more favorable. Thank the rest of my committee, Professor Carmen Menoni and Professor Anthony Marchese, who have been very supportive and provided helpful feedback to my research.

The many research members of LPDL have made the lab a fun and great environment to work in. I am indebted to Jim Topper, Brian Lee, Frank Loccisano, Dr. Sachin Josh, Dr. Binyamin Rubin and Dr. Vijay Surla as my colleges, who have supported me and provided lots of help to my research. I also must mention the valuable support that I received from Brian to proofread my dissertation.

Finally I wish to express my gratitude to my parents and my wife Aichun for their continuous moral support and encouragement throughout my professional endeavors.

# TABLE OF CONTENTS

ABSTRACT .....	ii
ACKNOWLEDGEMENTS .....	iv
LIST OF TABLES.....	viii
LIST OF FIGURES .....	ix
Chapter 1 Introduction to Hall Thruster Erosion Measurement.....	1
1.1. Objective .....	1
1.2. Spacecraft Propulsion.....	2
1.3. Hall Thruster and Its Lifetime .....	6
1.3.1. Hall Thruster .....	6
1.3.2. Sputter Erosion in Hall Thrusters.....	9
1.4. Previous Studies on Hall Thruster Erosion .....	12
1.4.1. Experimental Lifetime Measurements of Hall Thrusters.....	12
1.4.2. Numerical Models of Hall Thrusters .....	15
1.5. Outline of Thesis.....	16
Chapter 2 Cavity Ring Down Spectroscopy .....	18

2.1. History of Cavity Ring Down Spectroscopy .....	18
2.2. Theory of the CRDS Technique.....	21
2.2.1. Optical Cavity.....	21
2.2.2. Basic Scheme of CRDS.....	25
2.2.3. Mode Matching .....	28
2.3. CRDS Experimental Schemes.....	31
2.4. Summary .....	36
Chapter 3 Manganese CW-CRDS Sputter Erosion Sensor .....	37
3.1. Sputtering Apparatus .....	37
3.2. Mn Sputter Erosion Sensor .....	40
3.2.1. Laser Source for Mn Detection .....	40
3.2.2. Experimental Setup for the Mn Erosion Sensor .....	41
3.2.3. Data Acquisition System.....	43
3.3. Demonstrative Measurements of Mn Erosion Sensor .....	47
3.4. End-point Detection.....	51
3.5. Hall Thruster Erosion Measurement with Mn CRDS Sensor .....	55
3.5.1. Optical Rail System.....	55
3.5.2. Hall Thruster Erosion Test.....	57
3.6. Summary .....	63
Chapter 4 Boron Nitride CW-CRDS Erosion Sensor.....	65
4.1. Boron Nitride Detection Scheme.....	65

4.2. Boron Nitride CW-CRDS Erosion Sensor .....	68
4.2.1. Frequency-Quadrupled ECDL System.....	68
4.2.2. Experimental Setup of the Boron Erosion Sensor .....	70
4.3. Fiber Delivery for a Single Mode Laser Beam of 250 nm.....	72
4.3.1. Laser Delivery with Photonic Crystal Fiber .....	74
4.3.2. Single Mode Output Validation .....	76
4.3.3. Transmission of the PCF .....	77
4.3.4. Optical Damage of the PCF .....	80
4.4. Demonstrative Erosion Measurements and Validation.....	82
4.4.1. Number Density Measurements of Sputtered Boron.....	83
4.4.2. Preliminary Thruster Testing.....	86
4.4.3. Sensitivity Analysis.....	87
4.5. Summary .....	88
Chapter 5 LIF Velocity Measurements of Sputtered Boron Atoms .....	90
5.1. LIF Velocity Measurement for Sputtered Particles.....	91
5.1.1. LIF Velocity Measurement Technique.....	91
5.1.2. Velocity Distribution of Sputtered Particles.....	95
5.2. LIF Experiment Apparatus.....	96
5.3. Boron Reference Spectrum from Hollow Cathode Lamp .....	99
5.4. Results and Analysis of LIF Measurements .....	102
5.4.1. Demonstrative Measurement.....	102
5.4.2. BN LIF Spectrum.....	104
5.5. Summary .....	109

Chapter 6 Conclusion and Future Work .....	111
6.1. Conclusion .....	111
6.2. Future Work .....	113
6.2.1. Improvements to BN Erosion Sensor .....	113
6.2.2. Hall Thruster Testing.....	115
Bibliography.....	117

## LIST OF TABLES

Table 4.1: Table of boron atoms transitional information.....	67
Table 5.1: Fitting results for LIF measurements with Ar ion beam.....	105
Table 5.2: Fitting results for LIF measurements with Xe ion beam.....	108

## LIST OF FIGURES

Figure 1.1: Cross-section schematic of a SPT Hall thruster.....	7
Figure 1.2: Left: Schematic of Hall thruster wall erosion. Right: Hall thruster erosion after 500 hours of operation at Keldysh Research Center.....	11
Figure 2.1: Sample mode structure of an optical cavity.....	23
Figure 2.2: Basic scheme of CRDS. HR: high reflector, Det.: detector, $\tau_0$ and $\tau$ : decay time constants.....	25
Figure 2.3: Comparison between ring-down signals with / without mode beating. ....	30
Figure 2.4: Typical experimental setup of CW-CRDS.....	33
Figure 2.5: Schematic of an AOM. ....	35
Figure 3.1: Schematic of sputtering apparatus.....	38
Figure 3.2: Schematic of the ECDL.....	41
Figure 3.3: Schematic of CW-CRDS with mirrors outside the vacuum, PD: Photo detector, HR: High reflector. ....	41
Figure 3.4: Sample graph of collected signals in Labview.....	44

Figure 3.5: Graph of PZT signal and corresponding etalon signal. ....	46
Figure 3.6: Simplified schematic representation of the hysteresis loop. ....	46
Figure 3.7: Graph of fitting curves for wavelength calibration in Labview. ....	47
Figure 3.8: Aluminum honeycomb structure. ....	49
Figure 3.9: CRDS Mn hyperfine structure and the modeled spectrum.....	50
Figure 3.10: Dependence of path-integrated number density of Mn on ion beam current.....	51
Figure 3.11: Schematic diagram of sputtering multilayer target.....	52
Figure 3.12: End-point detection experimental result.....	53
Figure 3.13: Fiber-coupled rail for implementation within vacuum chamber. ....	57
Figure 3.14: Cross section of the anode layer type Hall thruster.....	58
Figure 3.15: Photograph of optical cavity hardware inside the vacuum chamber. .....	60
Figure 3.16: Sample spectrum of Mn from Hall thruster test.....	61
Figure 3.17: Measured erosion rates from CW-CRDS and from mass loss measurement at different discharge voltages.....	63
Figure 4.1: Partial energy level diagram of atomic boron. ....	67

Figure 4.2: Schematic of frequency-quadrupled ECDL system. ....	70
Figure 4.3: Experimental schematic of BN CW-CRDS erosion sensor.....	72
Figure 4.4: Schematic diagram of fiber launch for PCF characterization.....	75
Figure 4.5: Photograph of single-mode output beam from PCF. ....	76
Figure 4.6: Beam dimension versus relative position for $M^2$ determination. ....	77
Figure 4.7: Loss measurements: plot of fiber transmission versus fiber length.	79
Figure 4.8: Bend loss measurements: plot of bend loss versus radius of curvature.....	80
Figure 4.9: Left: photograph of red light emission near damaged fiber tip with the fiber jacket. Right: photograph of red light emission over length of damaged fiber without the fiber jacket. ....	81
Figure 4.10: Input power dependence of optical damage to the PCF. ....	82
Figure 4.11: Sample boron absorption spectrum. ....	84
Figure 4.12: (a): Dependence of path-integrated boron number density on the ion beam current at $V_b = 1200V$ , (b): Dependence of path-integrated boron number density on the ion beam voltage at $I_b = 40mA$ . ....	85
Figure 5.1: Simplified two level LIF model.....	91
Figure 5.2: Selected boron transitional lines for LIF.....	94

Figure 5.3: Experimental setup for boron LIF measurements.....	97
Figure 5.4: HCL frequency reference.....	100
Figure 5.5: Boron opto-galvanic spectrum from boron hollow cathode lamp..	102
Figure 5.6: Boron LIF spectrum and fit for Ar ions at 1200 eV.....	103
Figure 5.7: LIF signal intensity versus illuminated laser power.....	104
Figure 5.8: BN LIF spectra and fits at different Ar ion energies. ....	105
Figure 5.9: Best fit profiles for several values of $m$ for Ar ions at 800 eV. ....	106
Figure 5.10: Energy of Xe ions involved in thruster and in erosion versus discharge voltage.....	106
Figure 5.11: BN LIF spectra and fits for Xe and Ar ions at 1200 eV.....	107
Figure 5.12: BN LIF spectra and fits at different Xe ion energies. ....	108
Figure 6.1: Schematic of Brewster prism cavity.....	114

# Chapter 1

## Introduction to Hall Thruster Erosion Measurement

### 1.1. Objective

As human beings expand their knowledge and activities to outer space, an effective and reliable spacecraft propulsion method is of the utmost importance. A Hall thruster is one of the most promising types of spacecraft propulsion systems that has a high specific impulse and precise controllable thrust. However, the long term reliability of Hall thrusters is still under investigation and impacts their potential future applications. The objective of this thesis is to provide an innovative experimental way to measure the erosion of the acceleration channel wall in Hall thrusters for the ultimate purpose of evaluating a Hall thruster's lifetime. The erosion of the acceleration channel wall is the primary life-limiting factor for Hall thrusters<sup>[1-3]</sup>. Right now, there is a lack of effective and affordable experimental methods to characterize the erosion process within Hall thrusters quickly and accurately. Similarly numerical models lack adequate experimental results to give precise predictions. In this thesis, laser diagnostic sensors are developed for real-time Hall thruster erosion measurements. The sensors should also benefit the optimizations of

Hall thrusters' operation conditions, development of future longer lifetime thrusters, and the numerical modeling of Hall thruster erosion. Continued development of Hall thrusters will contribute to further space exploration and utilization.

## 1.2. Spacecraft Propulsion

Spacecraft propulsion provides a means to change the motion of spacecraft and artificial satellites. All the propulsion methods gain thrust,  $\vec{T}$ , based on Newton's third law of motion as well as the conservation of total momentum:

$$\vec{T} = \dot{m}_p \vec{v}_p = M \frac{d\vec{v}_R}{dt} \quad (1.1)$$

Where  $\dot{m}_p$  is the mass flow rate of the propellant ejected from the spacecraft of a time dependent mass  $M$ ;  $\vec{v}_p$ , the effective exhaust velocity of the propellant;  $\vec{v}_R$ , the velocity of the spacecraft. As a result, the spacecraft with a time dependent mass of  $M$ , which follows the relation of  $dM/dt = \dot{m}_p$ , gets an acceleration of  $d\vec{v}_R/dt$ . With an assumption of constant effective exhaust velocity  $\vec{v}_p$ , the integration of thrust over the full thruster operation time (under no influence from other force) results in the famous Tsiolkovski rocket equation<sup>[4]</sup>:

$$\Delta v_R = v_p \ln \frac{M_i}{M_f} \quad (1.2)$$

where  $\Delta v_R$  is total change in velocity of the rocket (delta-v). Without any external interference,  $\Delta v_R$ , depends on the effective exhaust velocity  $v_p$ , the initial rocket mass  $M_i$  and its final mass  $M_f$ . The final mass includes the mass of the useful equipment (payload) and the mass of thruster related structure. A high payload mass to total initial mass ratio is very desirable. Specific impulse, termed  $I_{SP}$ , is a measure of thruster efficiency and is defined as the ratio of the thrust to the rate of propellant consumption<sup>[2]</sup>, which is equivalent to the ratio of the exhaust velocity to the acceleration due to gravity on earth surface:

$$I_{SP} = \frac{T}{\dot{m}_p g_0} = \frac{v_p}{g_0} \quad (1.3)$$

For a specific delta-v mission, a propulsion method with a higher specific impulse means higher propellant efficiency and less propellant mass required. High specific impulse contributes to reduced total mass and increased payload mass to total mass ratio, thereby reducing the launch cost of a spacecraft or satellite.

Two of the most important and widely-used spacecraft propulsion methods are chemical propulsion, which employs chemical reactions to generate thrust, and electric propulsion (EP), which produces thrust primarily from electric power. Chemical propulsion rockets can be very powerful and have been most extensively used. They can generate very high thrust ( $T$  up to

$\sim 10^7$  N). All current spacecraft use chemical propulsion rockets in the launch period to overcome the Earth's gravitational force and quickly accelerate the spacecraft. However, the effective exhaust velocity of a chemical rocket is limited by the finite internal energy released from the chemical reaction (combustion). Thus chemical rockets have low specific impulses of  $I_{sp} \sim 500$  s or less, which requires a large amount of propellant mass for specific missions. When the spacecraft launches in low gravity, the priority shifts from high thrust to high propulsion efficiency, since the total fuel mass is limited. As a result, EP was developed to achieve thrust with high specific impulse and allow for a low ratio of propellant mass to the total mass of the spacecraft. In addition to the advantage of propellant mass conservation for space missions, EP offers other attractive benefits, including precise thrust control, generous shutdown and restart capabilities, and the use of chemically passive propellants<sup>[5]</sup>.

The attractiveness of EP for a broad variety of space transportation applications was recognized in early nineteenth century<sup>[2]</sup>. As technologies develop, many different EP devices have been developed, tested and used in space applications. All EP devices can be generally categorized into three main types: electrothermal, electrostatic and electromagnetic, based on terms of the acceleration method used to produce the thrust<sup>[2, 5]</sup>. Electrothermal thrusters, such as resistojets and arcjets, heat the propellant with electric power and expel the propellant through a suitable nozzle. They can have specific impulses ranging from a few hundred to around one thousand seconds. Electrostatic

thrusters, such as ion thrusters and field emission electric propulsion (FEEP) thrusters, accelerate the ionized propellant with electrostatic forces and reach thousands or tens of thousands seconds of specific impulses. Electromagnetic thrusters, such as Hall thrusters, pulsed plasma thrusters (PPT) and magnetoplasmadynamic (MPD) thrusters, apply both electric and magnetic fields to accelerate charged propellant with specific impulses of thousands seconds.

Although EP systems provide very high specific impulses, they generally produce very low thrust (single to tens of Newtons, or less) due to the limitation of thrust densities or the electric power from spacecraft<sup>[2]</sup>. EP systems are not suitable for launch or rapid maneuvers of any spacecraft near strong gravitational fields. Thus, the near-planet applications of EP are limited to missions, such as attitude control, station keeping and drag compensation, which require low thrust with precision, propellant mass conservation, and long operational lifetime<sup>[5]</sup>. Whereas on ambitious interplanetary missions and deep space explorations, EP shows great advantages over chemical propulsion due to much higher specific impulse. One of the most successful examples on space exploration with EP is the Hayabusa mission, in which the Japan Aerospace Exploration Agency (JAXA) used a spacecraft Hayabusa with four xenon ion engines to collect sample from the small near-earth asteroid Itokawa and return to Earth<sup>[6]</sup>. With the low thrust output from EP, these ambitious space missions have to operate the EP thrusters for a long time. The Hayabusa

mission concluded successfully on June 13, 2010 after more than 7 years of space travel with EP. Therefore, the lifetime of EP devices is an extremely critical factor for all these applications and need to be carefully validated for space missions.

### **1.3. Hall Thruster and Its Lifetime**

#### **1.3.1. Hall Thruster**

Early development of Hall thrusters began independently in both the former Soviet Union and the United State during the 1950s and 1960s<sup>[2]</sup>. The basic concept of a Hall thruster, which came from plasma physics development related to controlled fusion reaction studies, was first developed into an efficient propulsion device in the Soviet Union. Over 200 Hall thrusters have been operated in space since 1971, when Soviets flew the first pair of Hall thrusters on the Meteor satellite<sup>[7]</sup>. Not until the 1990s were the Soviet-built thrusters introduced to the United States, Europe, and Japan. Since then, a large amount of research efforts on Hall thrusters has been done throughout the world to improve thruster performance and lifetime. Now Hall thrusters are one of the most commonly used EP thrusters including in commercial applications.

A Hall thruster, sometimes referred to a “closed-electron-drift” device, is a type of EP thruster that produces plasma and generates thrust with a form of the “Hall effect”, which derives from the ability of the current-carrying electrons to execute significant portions of their cycloidal motions before collision with other heavy particles<sup>[5]</sup>. Hall thrusters have a relatively simple structure

consisting of an annular acceleration channel housing an interior anode, a magnetic circuit producing radial magnetic field, and an external cathode. Two different types of Hall thrusters are the Stationary Plasma Thruster (SPT) and the thruster with anode layer (TAL)<sup>[2, 7, 8]</sup>. Figure 1.1 shows a basic cross-section schematic of a SPT type thruster, which is more commonly used and studied.

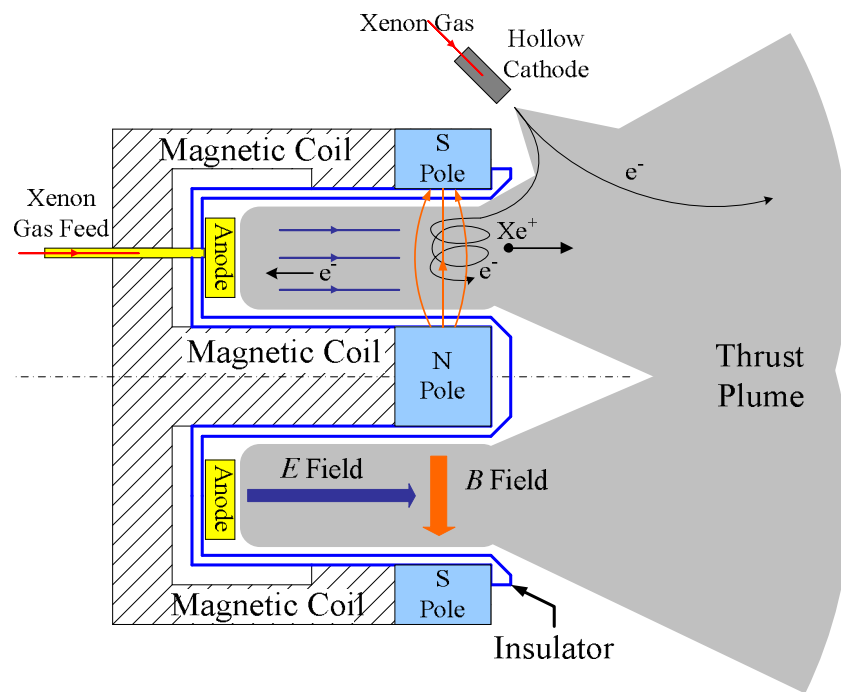


**Figure 1.1: Cross-section schematic of a SPT Hall thruster<sup>[2]</sup>.**

As shown in Fig. 1.1, the positive voltage applied to the anode creates an electric field for ion acceleration along the acceleration channel, which is lined by two concentric ceramic tubes. While an orthogonal magnetic field is generated with a magnetic coil protected with channel wall. In SPTs, dielectric insulating materials such as boron nitride (BN) or borosil (BN-SiO<sub>2</sub>) ceramic<sup>[2]</sup>

are used in channel wall material, because of the excellent thermal and chemical stability with high electrical resistance. Due to the “Hall effect”, electrons from the external cathode are trapped within the channel of the Hall thruster by an orthogonal electromagnetic field and ionize the propellant gas (usually xenon). Heavy positive ions with a large Larmor radius are accelerated by the axial electric field along the acceleration channel to a very high speed (~15 to 30 km/s) and produce thrust. The ion beam is neutralized with electrons from the hollow cathode to balance the charge of the system. Since ion acceleration takes place in a quasi-neutral plasma, Hall thrusters are not limited by space-charge build-up<sup>[2]</sup>. Hence, higher current and thrust densities than conventional ion thrusters can be achieved at discharge voltages from hundreds volts to a few kilovolts. Generally, SPT and TAL apply many of the same basic ideas and principles, including the basic ion generation and acceleration method, however they have different channel wall materials and acceleration channel lengths. The TAL has a conductive metallic channel wall and a shorter channel wall. The details of the channel structure, wall material and magnetic field shape determine the performance, efficiency, and lifetime. More differences between two types of Hall thrusters have been described in the literature<sup>[8, 9]</sup>.

The thrust, with a typical value on the order of 0.01 N to 0.1 N, is produced by Hall thrusters with high efficiency (exceeding 50%) for a given electrical power<sup>[2]</sup>. As a result of low thrust, a prolonged thruster operation time

is needed for large delta-v missions as well as for long-term missions like satellite station keeping and drag compensation. It is critical for Hall thrusters to be reliable during the required operation time, which can reach thousands to tens of thousands of hours. Therefore, a correct estimation of the lifetime is critical in the design of new Hall thrusters and their assessment for applications.

### **1.3.2. Sputter Erosion in Hall Thrusters**

There are many factors that can cause failures in Hall thrusters, such as a faulty power process unit, depletion of the cathode, and malfunction of a solar array. However, the primary insurmountable lifetime limitation for Hall thrusters is the erosion of the acceleration channel wall (BN) caused by sputtering of the ions.

Sputtering describes a phenomenon in which atoms are removed or ejected from a solid material when struck by energetic particles<sup>[10-12]</sup>. Sputtering can be divided into two categories: physical and chemical. Physical sputtering, which is of interest in Hall thrusters, is caused by collisions between energetic (incident) particles and (target) atoms from the material surface through a transfer of kinetic energy. Whereas, chemical sputtering invokes a chemical reaction induced by the impinging particles which can produce an unstable compound at the target surface<sup>[11]</sup>. Physical sputtering processes are classified by the behavior of the displaced target atoms into three qualitative regimes: knock-on regime, linear cascade regime, and spike regime. Sputtering of

metals and semiconductors in the keV energy range can be well described by Sigmund's linear collision cascade theory<sup>[10-12]</sup>. In Hall thruster, the sputtering processes fall into the linear cascade regime, in which the energetic ion/atom hits the target surface and initiates collision cascades that eject atoms and electrons through the surface. Sputtering is complicated physical process and more details can be found in the literature<sup>[10-12]</sup>.

In order to quantify the sputter erosion rate, a total sputter yield  $Y$  is defined as the mean number of atoms removed from the surface of a material per number of incident particle as:

$$Y = \frac{\text{Number of removed atoms}}{\text{Number of incident particles}} \quad (1.4)$$

The number of removed atoms must be proportional to the number of incident particles in order to make the definition of sputter yield meaningful. Generally, the sputter yield  $Y$  depends on the type and state of the bombarded materials (especially the detailed structure and the surface composition), the characteristic of the incident particles (the mass, energy etc.), and the experimental geometry (incidence angle etc.)<sup>[12]</sup>. However, the total sputter yield does not include any information on the trajectories of the emitted particles from the surface of the target and the energy of the emitted particles. As a result, differential sputtering yields  $y(\alpha, \varphi, E)$  are defined as the number of particles sputtered per incident ion per steradian ( $\alpha$  is the polar angle,  $\varphi$  is the azimuthal angle). Differential sputter yield profiles are of basic interest for physical understanding of the sputtering process as well as in sputtering

applications (such as sputter deposition and contamination, electric propulsion erosion modeling, etc.).

In Hall thrusters, some of the ions impact the channel wall with enough energy to sputter the wall material. Even though dielectric wall materials (like BN) with a relatively low sputter yield are selected and used in SPTs, the slow sputtering erosion of the channel wall becomes a significant process during the long-term operation of Hall thrusters<sup>[1, 13-15]</sup>. Figure 1.2 shows a schematic of Hall thruster wall erosion<sup>[16]</sup> and an example of Hall thruster BN wall erosion after 500 hours of operation at Keldysh Research Center<sup>[17]</sup>.

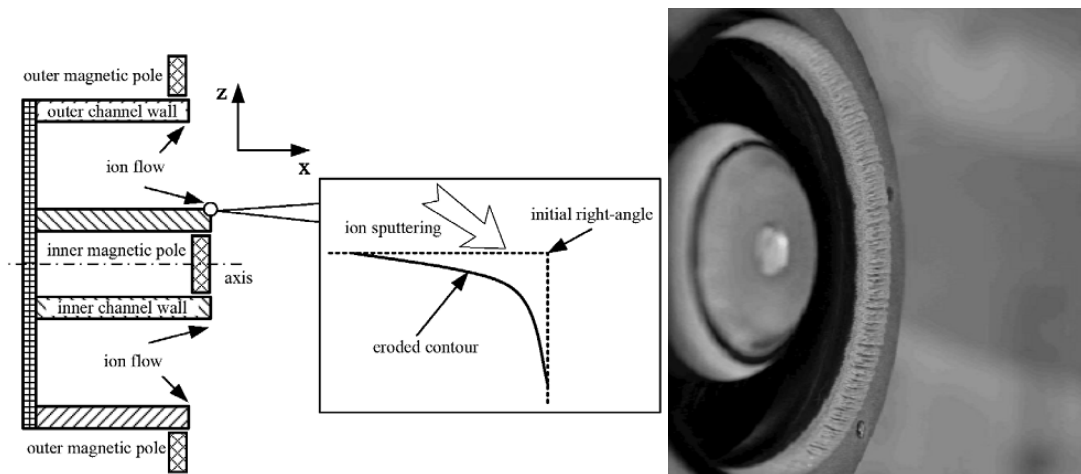


**Figure 1.2: Left: Schematic of Hall thruster wall erosion. Right: Hall thruster erosion after 500 hours of operation at Keldysh Research Center.**

The channel consists of two ceramic tubes placed one inside the other and centered about the thruster axis. Typically, the erosion depth gradually increases along the thruster axis and reaches its maximum at the initial right-angle of the corner. The channel wall has a limited thickness (several mm). Once the wall is etched through, the circuitry beneath the wall will be destroyed

by the plasma, which ends the life of a Hall thruster. Additionally, the eroded materials can cause re-deposition and form unwanted coatings on spacecraft surfaces such as solar arrays and sensitive sensor optics, thereby posing a serious risk to spacecraft operation. As a result, there is a need to understand the sputter erosion process in Hall thrusters. Owing to its widespread use, BN is the primary material of interest.

#### **1.4. Previous Studies on Hall Thruster Erosion**

Over the past few decades, various efforts have been done to test and predict the lifetime of Hall thrusters either by performing experimental measurements of sputter erosion or by building numerical models for Hall thruster erosion process. A brief review of these studies on Hall thruster erosion is presented here.

##### **1.4.1. Experimental Lifetime Measurements of Hall Thrusters**

Techniques used to measure sputtering fall into two general categories. One category is direct observation of (mass or size) changes of the sputter target, i.e. mass loss measurement and thickness change measurement. These techniques are evident and widely applied in direct lifetime measurements and wear tests of Hall thrusters<sup>[1, 13, 14]</sup>. The other category is based on measuring (or number density) of sputtered particles, i.e. collector plates<sup>[18]</sup> and quartz crystal microbalance (QCM)<sup>[19, 20]</sup>. Such experimental techniques have been employed to measure the real time erosion rates of Hall thrusters and predict the lifetime indirectly.

Direct lifetime measurement is very challenging. Currently, a ground based lifetime (endurance) test of a Hall thruster is the only accepted way to quantify the erosion process and measure the lifetime of Hall thruster<sup>[1, 13-15]</sup>. In ground based lifetime tests, Hall thrusters are operated continuously at full power for the desired full thruster operation duration in a vacuum facility. With proposed thrust durations now as long as 5-10+ years, ground-based life tests over the full thruster duration are becoming increasingly expensive and limiting in terms of technology insertion schedules. For example, an SPT-100 was operated for over 5,700 hours and performed nearly 7,000 start cycles at the Jet Propulsion Laboratory (JPL) as part of a flight qualification process.<sup>[1]</sup> The mass and/or volumetric changes of the wall material from sputter erosion are recorded during experiments. Previous studies shows that the erosion depends on operating condition, magnetic field configuration, wall material, anode configuration, and channel geometry. Understanding these dependences is essential for the future applications of Hall thrusters. However, there are many obvious limitations for such ground based tests including high cost and long duration as well as only the possibility of a *post-facto* bulk analysis for a fixed operational condition as opposed to real time analysis as operating points are varied. With this method of testing it is not practicable to validate all the lifetime at multiple conditions or different thruster designs.

Accordingly, other indirect lifetime measurement methods have been developed by studying the sputtered particles. The ideal diagnostic should

allow *in situ* erosion rate studies rather than the *post-facto* analysis provided by ground based tests. It should also have high sensitivity to measure low erosion rates, the possibility of integration to a thruster test-facility, and fast time-response to explore a range of operating conditions. Techniques such as collector plates, QCM, radioactive tracers<sup>[21]</sup>, mass spectrometry<sup>[22]</sup>, and Rutherford backscattering<sup>[23]</sup> each have certain advantages and can be appropriate for material sputter characterization studies, but none readily meets all of the above criteria for erosion measurement in Hall thrusters. The need for a sensitive non-intrusive measurement suggests the use of optical techniques. Optical emission spectroscopy (OES)<sup>[24-26]</sup>, laser induced fluorescence (LIF)<sup>[27-31]</sup> and laser absorption spectroscopy (LAS)<sup>[32, 33]</sup> have all been used for the plasma studies in Hall thruster. OES spectroscopy is attractive owing to its experimental simplicity and has also been used for *in-situ* thruster erosion measurements. Research from Murat *et al.*<sup>[26]</sup> and Pagnon *et al.*<sup>[34]</sup> shows the capability of relative wall erosion rate measurement with OES. The use of LIF has been particularly extensive, and has proven to be very effective for velocity measurement and number density measurement. However, neither OES nor LIF directly gives the absolute erosion rates. The absolute calibration is hard for complex plasma conditions within Hall thrusters. On the other hand, LAS does not require absolute calibration and measures the ground state of sputtered particle. Previous research done by Yamamoto *et al.*<sup>[32]</sup> shows great potential of using LAS for the real-time erosion measurement of Hall thruster. However, the

sensitivity of conventional LAS spectroscopy is relatively low, making it difficult to measure low densities of eroded particles (e.g. sputtered boron atoms).

#### **1.4.2. Numerical Models of Hall Thrusters**

Numerical models of Hall thrusters have been developed to overcome the limitation of experimental techniques (cost and time requirement). Different numerical models have been established and aimed to predict the thruster performance, simulate the erosion process and estimate the lifetime for Hall thrusters. However, the lack of data about impinging ion flow distribution, energy distribution of these ions, sputter process of BN, and change of the geometrical shape makes the numerical models difficult for correct lifetime estimation of Hall thrusters. Two pivotal problems in modeling are to model the plasma and wall flux relation, and the sputtering process of the wall material.

A considerable effort has been made to develop fluid, kinetic, hybrid and particle-in-cell (PIC) models to simulate the plasma and calculate the ion flux to the wall. A few examples are presented here. Manzella *et al.*<sup>[35]</sup> tried to predict the lifetime of Hall thruster with a fluid-based model, which assumed that diverted ions from an uniform plasma flow impact the wall and cause erosion. Bouf and Garrigues treated electrons as a fluid and ions as collisionless kinetic particles and developed a one-dimensional (1-D) hybrid model<sup>[36]</sup>. A two-dimensional PIC mode was developed by Hirakawa and Arakawa<sup>[37]</sup>. The most widely used and developed model is called *HPHall*, which is a 2-D transient hybrid model originated by Fife and Martinez-Sanchez<sup>[38]</sup>. Reasonable

agreements of the model results to the experimental erosion contour of SPT-100 Hall thruster has been achieved<sup>[3]</sup>. However, more experimental measurements are needed for model validation, which is also an important motivation of the present work.

Another complication lies in the sputtering behavior of the wall material, especially for BN in the needed low ion energy region ( $\sim 100$  eV)<sup>[3, 39]</sup>. The sputter yield data are exiguous and hard to measure accurately in the low energy region. In addition, the effect of the BN ceramic temperature on the sputtering is not clear. Currently, most of the sputtering models are based on Sigmund's work<sup>[12]</sup> of the sputtering mechanisms, though molecular dynamics approaches have also been developed<sup>[40]</sup>. Nevertheless, more experimental measurements to characterize the sputtering properties of BN at low energy are required for the numerical modeling.

## **1.5. Outline of Thesis**

This thesis focuses on the development of a Hall thruster erosion sensors using cavity ring down spectroscopy (CRDS), which provides ultra-sensitive measurement of sputtered particles in (near) real-time. A brief overview of CRDS history and methods is presented in Chapter 2. Chapter 3 describes a Mn CRDS detection system and experimental results including the first CRDS erosion measurement of a Hall thruster. Chapter 4 describes the boron CRDS detection system and provides demonstrative experimental results. A complementary LIF velocity measurement of sputtered boron atoms

is given in Chapter 5. Finally, Chapter 6 is a summary of contributions and suggestions for future work.

## Chapter 2

### Cavity Ring Down Spectroscopy

#### 2.1. History of Cavity Ring Down Spectroscopy

Since about 1960, modern spectroscopic investigations have been greatly expanded owing to the development of laser technology. Since then, many lasers at different wavelengths have been used as light sources to provide intense, collimated, monochromatic radiation sources for spectroscopic studies. Laser spectroscopy can provide many advantages including non-intrusive species-specific detection, fast *in situ* measurement, and remote sensing. Thus, various spectroscopic techniques have been applied to analyze a multitude of samples qualitatively and/or quantitatively for a wide range of applications. Among all the laser spectroscopic techniques, CDRS is a relatively recent and attractive method that combines direct absorption spectroscopy with an enhanced optical cavity. Direct absorption spectroscopy quantitatively measures the frequency-dependent absorption of radiation through a sample (e.g. atoms and molecules in the gas phase). In a conventional absorption experiment, the intensity attenuation of the light through a sample is measured to calculate the number density of particles. The

sensitivity is generally limited by the accuracy of the light intensity measurement. In the case of a weak absorber (e.g. very low density plasma), the intensity attenuation from the absorber is too weak to accurately measure over a large background. As a result, CRDS, a sensitivity-enhancing method, has been developed to improve the sensitivity by increasing the effective absorption path length with an optical cavity. Instead of detecting the light intensity attenuation, CRDS measures the decay rate of the light intensity inside of a high-finesse optical cavity. Many publications have been published experiments using this technique. Here, a brief review of CRDS development is presented, while more details of CRDS can be found in several good review papers<sup>[41-44]</sup>.

The earliest version of CRDS originated from the need for precise measurement of high reflectance from dielectric mirror coatings. Herbelin *et al.*<sup>[45]</sup> in 1980, and Anderson *et al.*<sup>[46]</sup> in 1984, respectively demonstrated the reflectance measurement of mirrors using optical cavities with laser. In 1988, O'Keefe and Deacon first introduced the CRDS technique for spectroscopic application<sup>[47]</sup>. They measured the absorption spectrum of oxygen molecules inside an optical cavity with a pulsed dye laser. Concentrations of about 450 ppm at 690 nm and 75 ppm at 630 nm were achieved, corresponding to a minimum detectable absorption coefficient of  $\sim 10^{-6} \text{ cm}^{-1}$ <sup>[47]</sup>. Due to the simple experimental design and high sensitivity of CRDS with pulsed laser sources (P-CRDS), the detection scheme soon thrived in many applications such as

combustion diagnostics and trace gas detection for atmospheric and environmental studies. Further extensions of the P-CRDS techniques, including Fourier transform (FT) CRDS<sup>[48]</sup> and polarization dependant CRDS<sup>[49]</sup>, were developed for different applications.

At the same time as O'Keefe and Deacon's introduction of P-CRDS, Le Grand and Le Floch used a continuous wave (CW) light source (single frequency He-Ne laser) to measure the residual reflectivity of an anti-reflective (AR) coated quarter wave plate inside a high finesse optical cavity<sup>[50]</sup>. Laser light was coupled into the cavity through scanning the cavity length with a piezoelectric transducer (PZT). A 1-ppm level sensitivity of absorbance was achieved with their experimental scheme. In 1990, the same French group developed a more sophisticated and improved version of CRDS with a CW laser source (CW-CRDS)<sup>[51]</sup>. An acousto-optic modulator (AOM) along with a threshold detection circuit was used to extinguish resonant light and yield ring-down events. This technique was later adopted by Romanini *et al.* for spectroscopic study, measuring the spectrum for a section of the weak C<sub>2</sub>H<sub>2</sub> overtone transition near 570 nm in 1997<sup>[52]</sup>. Thereafter, many publications have reported various applications of CW-CRDS and its derivatives.

The CRDS technique has been introduced as a diagnostic tool for the non-intrusive *in-situ* study of sputtering processes at Colorado State University. Initially, a P-CRDS system<sup>[53-59]</sup> was used with a broadly tunable optical parametric oscillator (OPO) laser system, which was pumped with a pulsed

Nd:Yag laser. The P-CRDS system was integrated with a sputtering apparatus (similar to the system mentioned in Chapter 3). Number densities of sputtered particles from multiple metallic targets (including iron, aluminum, titanium and molybdenum) have been measured<sup>[54-56]</sup>. Velocity information of sputtered particles was also inferred from Doppler shift contributions to the CRDS absorption line<sup>[57]</sup>. The spatial resolution of number density measurements from CRDS was demonstrated through differential sputter yield measurements<sup>[59]</sup>. In 2007, the group at Colorado State University started to build CW-CRDS systems as sensors for Hall thruster sputter erosion measurements.

## **2.2. Theory of the CRDS Technique**

CRDS is a direct absorption spectroscopy measurement technique, which can be performed with both pulsed and continuous-wave light sources. It provides measurements with extremely high sensitivity by employing enhanced optical-path length. The basic theory of CRDS technique is explained here.

### **2.2.1. Optical Cavity**

An optical cavity, similar to that used in many laser sources and etalons, plays a very important role in CRDS. An optical cavity (or resonator) is an arrangement of optical components (e.g. mirrors, prisms, fibers) which allows light inside to circulate in a closed path. Two opposing mirrors can form the simplest optical cavity. The properties of a two-mirror cavity is briefly discussed under the paraxial condition in following paragraphs.

The arrangement of mirrors in an optical cavity determines its stability. For a stable optical cavity, light inside the cavity has a limited transverse offset and angle after many round trips. Whereas in unstable cavities, light leaves the optical cavity due to an unlimited increase in transverse offset or angle. In CRDS, a stable cavity is generally required to hold the light inside the cavity and extend the effective path length through the sample. A cavity g-parameter is defined as a function of both the cavity length  $L$  and the mirror's radius of curvature (ROC)  $r$ :

$$g = 1 - \frac{L}{r} \quad (2.1)$$

The stability condition of an optical cavity can be derived from ABCD ray tracing matrices<sup>[60]</sup>. The stability condition is related to the product of two mirrors' g-parameters and expressed as:

$$0 \leq g_1 \cdot g_2 \leq 1 \quad (2.2)$$

For example, a symmetric cavity ( $g_1 = g_2$ ) was formed with two 1-m ROC mirrors during my research. The cavity length for a stable cavity needs to be shorter than 2 m. A cavity length around 75 cm is typically used in my experiments.

An optical cavity can also be viewed as a *trapping box* for light radiation. The cavity is capable of sustaining stationary or weakly damped transverse electromagnetic (TEM) field configurations at selected optical frequencies. Such TEM modes are labeled as  $TEM_{pql}$ .  $p$ ,  $q$  and  $l$  are non-

negative integers, corresponding to the azimuthal, radial and fundamental mode numbers. The field distributions of TEM modes with rectangular symmetry, which happen in most laser cavities, can be given as a product of two Gaussian functions and two Hermite polynomials with orders  $p$  and  $q$ . Thus, these cavity modes are also called Hermite-Gaussian modes. The lowest order,  $TEM_{00l}$ , is the Gaussian mode (also known as the fundamental mode) while all the other non-Gaussian modes are called transverse modes (or higher-order modes). Each mode has its own resonance frequency  $\nu_{pql}$ , which is given as:

$$\nu_{pql} = \frac{c}{2nL} \left[ p + \frac{1+q+l}{\pi} \cos^{-1} \left( \pm \sqrt{g_1 g_2} \right) \right] \quad (2.3)$$

where  $c$  is the speed of light;  $n$  is the index of reflection;  $L$  is the length of the optical cavity;  $g_1$  and  $g_2$  are the g-parameters for two cavity mirrors. Consecutive fundamental modes ( $q = 0, l = 0$ ) differ by a constant frequency called the free spectral range (FSR):

$$FSR = \frac{c}{2nL} \quad (2.4)$$

A simple schematic of the mode structure inside the cavity is show in Fig. 2.1.

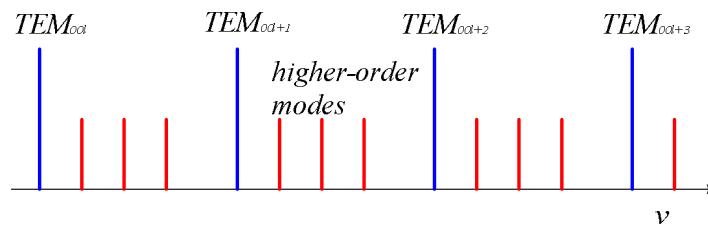


**Figure 2.1: Sample mode structure of an optical cavity.**

For example, a 75-cm cavity in qi4 formed by two 1-m ROC mirrors has a FSR of 200 MHz. The spacing between the successive higher-modes is about 84 MHz. The mode structure of an optical cavity plays a important role when coupling laser into the cavity. In order to obtain efficient coupling, it is necessary to match the laser to the cavity modes and this procedure is known as mode matching. In a mode-matching process, the electric field distribution of a laser beam needs to match spatially with that of selected cavity modes. A proper mode-matching process in CRDS will not only couple laser power into the cavity efficiently but also avoid multiple mode beating and improve the signal-to-noise ratio (SNR), which is discussed later in this chapter.

Another important parameter of an optical cavity is its finesse, which is an indication of the quality of the cavity. The finesse of a two-mirror cavity is a function of mirrors' reflectivities  $R_1$  and  $R_2$ :

$$F = \frac{\pi(R_1 R_2)^{1/4}}{1 - \sqrt{R_1 R_2}} \quad (2.5)$$

The finesse is also a measure of the effective path length for the light inside the cavity. In a high finesse cavity, the effective path length is proportional to the finesse of the cavity. Long effective path length is desired in a ring-down cavity. As a result, mirrors with high reflectivity are preferred. Dielectric mirrors, which have high reflectivity and small scatter and absorption losses, are commonly used to form the high finesse cavity. Dielectric mirrors are made from super-polished substrates with a typical surface roughness at the angstrom level. A

multilayer thin-film dielectric coating, designed to maximize reflectivity from interference, is deposited on the substrate surface with thin-film deposition techniques (e.g. sputter deposition, chemical vapor deposition). Ultra-high reflectivity (99.999% or better) over a narrow range of wavelengths ( $\sim 10$  nm) can be achieved over most of the infrared (IR) and visible spectral range. However, the best available reflectivity of dielectric mirrors drops as the wavelength moves into the ultraviolet (UV) range due to absorption of the dielectric coating. For example, the best mirrors at 250 nm wavelength range have a reflectivity of  $\sim 99.8\%$ . The relatively low reflectivity of such cavity mirrors is one of the major factors limiting the sensitivity of CRDS measurements in the UV range.

### 2.2.2. Basic Scheme of CRDS

The basic idea of CRDS is to place the absorbing samples (e.g. sputtered particles) within a high-finesse cavity as shown in Fig. 2.2.

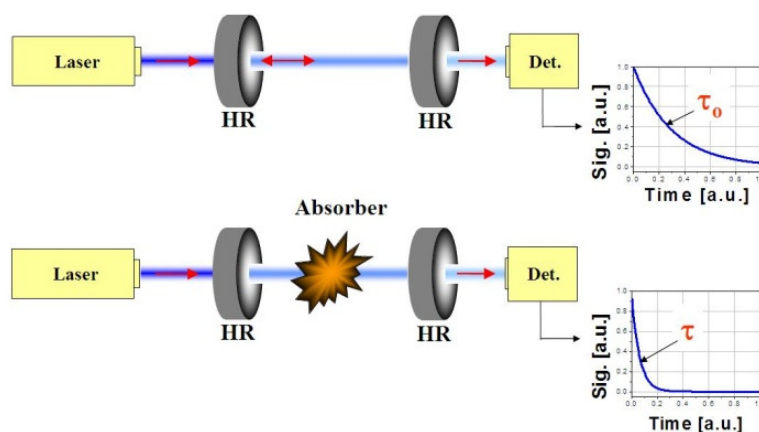


Figure 2.2: Basic scheme of CRDS. HR: high reflector, Det.: detector,  $\tau_0$  and  $\tau$ : decay time constants.

A short pulse of the probe laser beam is coupled into the optical cavity where it is reflected back and forth many times, e.g.  $\sim 10^4$  passes for a mirror reflectivity of  $R \approx 0.9999$ . The high number of passes through the cavity greatly increases the effective path length and thus greatly increases the absorption detection sensitivity. Each time when the light inside the cavity reaches a mirror, a small fraction leaks out. A detector placed behind the cavity measures the intensity of light exiting the cavity, which is termed the ring-down signal. When there is an absorber present inside the cavity, the ring-down signal decays faster compared to an empty cavity. Under appropriate conditions, this ring-down signal  $I(t, \nu)$  decays exponentially versus time following the Beer-Lambert law with a initial intensity of  $I_0$  as:

$$I(t, \nu) = I_0 \exp\left[-\frac{t}{\tau(\nu)}\right] \quad (2.6)$$

where  $\tau(\nu)$  is the  $1/e$  time of the decay. The ring-down time  $\tau(\nu)$  is extracted by performing an exponential fit to the measured ring-down signal. The “empty cavity ring-down time”,  $\tau_0$ , denotes the ring-down time of a cavity with no absorbing medium inside the cavity. It is related to the transmission loss and the length of the cavity. The absorption coefficient  $k(x, \nu)$  of the absorber can be a function of position  $x$  along the optical axis and frequency  $\nu$ . The ring-down time  $\tau(\nu)$  associated with the total absorption loss along the optical axis is:

$$\tau_0 = \frac{L}{c \cdot (1-R)}; \quad \tau(\nu) = \frac{L}{c \cdot \left[ (1-R) + \int k(x, \nu) dx \right]} \quad (2.7)$$

The sample absorbance along the optical axis,  $Abs(\nu)$ , can be derived from the change of ring-down time:

$$Abs(\nu) \equiv \int k(x, \nu) dx = \frac{L}{c} \left[ \frac{1}{\tau(\nu)} - \frac{1}{\tau_0} \right] \quad (2.8)$$

A typical way to obtain an absorption spectrum is to scan the laser frequency across one of absorption lines of the sample and measure the ring-down time at different frequencies.  $\tau_0$  is often measured by detuning the laser away from resonance frequency of the absorber. In this way, the frequency (or wavelength) dependent absorption spectrum is measured. Using known (atomic or molecular) spectroscopic parameters for the selected transition from a lower state  $i$  to an upper state  $k$ , the measured absorption line area,  $\int Abs(\nu) d\nu$ , can be converted to the path-integrated concentration of the absorbers (at the lower state  $i$ ) along the optical axis  $\int N_i dx$  by:

$$\int N_i dx = 8\pi \frac{g_i}{g_k} \frac{\nu_{ki}^2}{A_{ki} c^2} \left( \int Abs(\nu) d\nu \right) \quad (2.9)$$

where  $g_i$ ,  $g_k$  are the level degeneracies,  $\nu_{ki}$  is the transition frequency, and  $A_{ki}$  is the transition Einstein A coefficient. An estimation of the minimum detectable absorbance can be found from the noise of ring-down time in the CRDS detection system. The minimum detectable absorbance,  $Abs_{Min}$ , is calculated as<sup>[61]</sup>:

$$Abs_{Min} \equiv \frac{\Delta\tau}{\tau}(1 - R) \quad (2.10)$$

where  $\Delta\tau$  is the uncertainty (noise) in measurement of ring-down time  $\tau$ . From eqn. 2.10, it is easy to understand that higher mirror reflectivity provides smaller minimum detectable absorbance.

Like other laser absorption methods, CRDS can provide directly quantitative measurements by probing ground states, as a large fraction of the species population can be directly measured (in contrast to OES, which measures only small population fractions of excited states). Furthermore, the CRDS technique is self-referencing, i.e. It does not require any external calibration to calculate a number density. The high sensitivity and quantitative nature of CRDS makes it amenable to measuring the low number densities of sputtered particles encountered in EP thrusters, and the non-intrusive optical probing also allows *in situ* measurements.

### **2.2.3. Mode Matching**

The spectral mode structure of the optical cavity must also be taken into consideration for CRDS. It becomes problematic for coupling the laser light into the cavity and producing noise free ring-down signals. Experimentally, there are two general ways to couple light into a cavity. One can either use a relatively broad linewidth light source to excite multiple cavities modes, or a narrow linewidth light source to couple to a single fundamental cavity mode with proper mode-matching optics.

A typical tunable pulsed system generates a broad bandwidth (e.g.  $\sim 0.1 \text{ cm}^{-1}$  for many commercial pulsed dye lasers) laser pulse much larger than the cavity mode spacing. Such a laser pulse is capable of exciting several cavity modes (fundamental and transverse modes) simultaneously. In such cases, there is no need for special mode-matching process to couple the laser pulse into a cavity. However, the energy coupling efficiency is very low ( $\sim 10^{-5}$  or less) since the majority of the laser power does not fall on top of the comb-shape cavity modes. The energy coupling efficiency can be increased a little by using a “quasi-continuum” optical cavity with a very dense mode spectrum, which can be achieved either by properly adjusting the length of the cavity<sup>[62]</sup> or by applying a mechanically unstable cavity<sup>[63]</sup>. Another problem arises with multimode excitation. Theoretically, all the cavity modes are orthogonal to each other, which can be proven from the equations for the mode field distributions, so that there should not be interference between different modes. However, the transverse modes are spatially more extended than the fundamental modes. As a result, many experimental factors, including spatial imperfection of mirrors and detector surface, small detector size and spatial variation of the sample, will break the orthogonality between cavity modes and lead to mode beating in the ring-down signal<sup>[64]</sup>. Figure 2.3 shows a comparison of the ring-down signals with/without mode beating. The mode beating can introduce more error in extraction of the actual ring-down time and reduce the sensitivity of the measurement. In order to avoid the disadvantage of mode beating, single

fundamental mode excitation of P-CRDS was demonstrated by Zee *et al.*<sup>[65]</sup> and Lee *et al.*<sup>[66]</sup> with spatial filters (pinholes) either outside or inside the cavity to filter higher-order modes. The problem of mode beating also motivated the use of a narrow bandwidth light source .

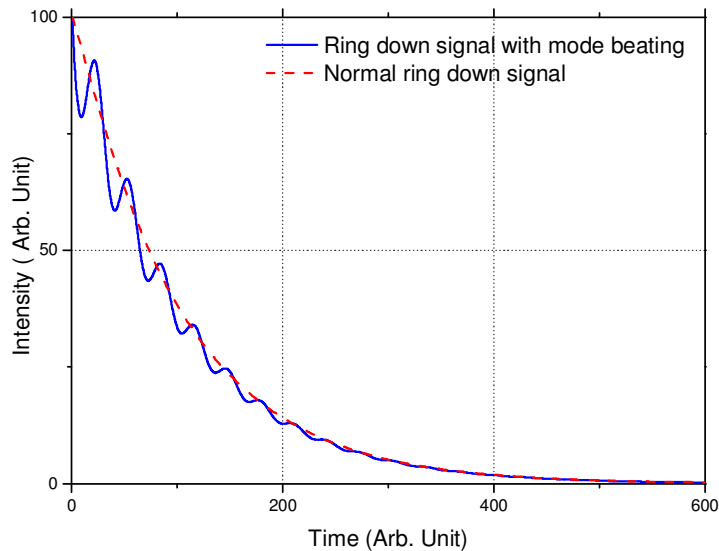


**Figure 2.3: Comparison between ring-down signals with / without mode beating.**

Continuous-wave lasers used in CW-CRDS have a smaller spectral linewidth (typically less than  $\sim 1-10$  MHz) as compared to the spacing of cavity modes. The narrow linewidth makes possible the excitation of a single fundamental mode with high energy coupling efficiency. CW lasers can be coupled into a high-finesse cavity both passively and actively. In either case, a good input beam quality is essential for high efficiency mode matching to the fundamental cavity modes. Generally, the laser beam is shaped to a Gaussian beam either by applying some spatial filters or by passing through a single-mode fiber. Optical components (usually a lens) are placed in a proper position

relative to the optical cavity and reshape the Gaussian beam to spatially match its parameters with the parameters of the fundamental modes inside the cavity. The position of mode matching optics can be calculated with ray tracing techniques, the detail of which are given in a review paper for optical resonators<sup>[60]</sup>. In a passive mode matching scheme, the laser scans its frequency through the cavity modes. High coupling efficiency only occurs with the intermittent resonance of the laser frequency with a fundamental mode in the cavity during the laser scan. The rate of laser / cavity resonance can be increased by modulating the cavity length with PZT attached to one mirror during the laser frequency scan. Whereas in an active mode matching scheme, high coupling efficiency can be achieved continuously with active mode locking methods (e.g Pound-Drever-Hall locking scheme) that lock the cavity modes to the laser or vice versa<sup>[67-70]</sup>.

The difference between mode matching of pulsed laser sources and CW laser sources results in two different experimental schemes with different features. My research focuses on the development of CW-CRDS systems which are further discussed in the following section.

### **2.3. CRDS Experimental Schemes**

The experimental setup of P-CRDS is simple and conceptually similar to the scheme in Fig. 2.2, although some mode matching optics may be involved. The tunable pulsed lasers can have a very broad tuning range, which enables a P-CRDS system to detect many different species at different wavelengths. For

example, multiple metallic materials have been studied at different wavelengths with a P-CRDS using the OPO laser system in our lab<sup>[54-56]</sup>. Despite these advantages, P-CRDS has several obvious drawbacks limiting its sensitivity. First, the very low energy coupling efficiency and short energy build-up time results in low signal-to-noise ratio (SNR) of the detector, which needs to operate at a higher gain. Second, the mode beating noise from multimode excitation leads to a larger uncertainty in ring-down time measurement. Third, most pulsed lasers have a relatively low repetition rate (~10 Hz), which limits the acquisition rate of ring-down events. The method of averaging multiple ring-down signals is commonly adopted to increase the accuracy of the measurement. The low acquisition rates can cause either longer measurement time or lower accuracy. Fourth, tunable pulsed lasers are usually expensive and physically large, which makes an economic portable design difficult.

The development of CW-CRDS requirements provide increased sensitivity relative to P-CRDS though more stringent mode-matching. In contrast to P-CRDS, the experimental setup of CW-CRDS is more complicated, as shown in Fig. 2.4.

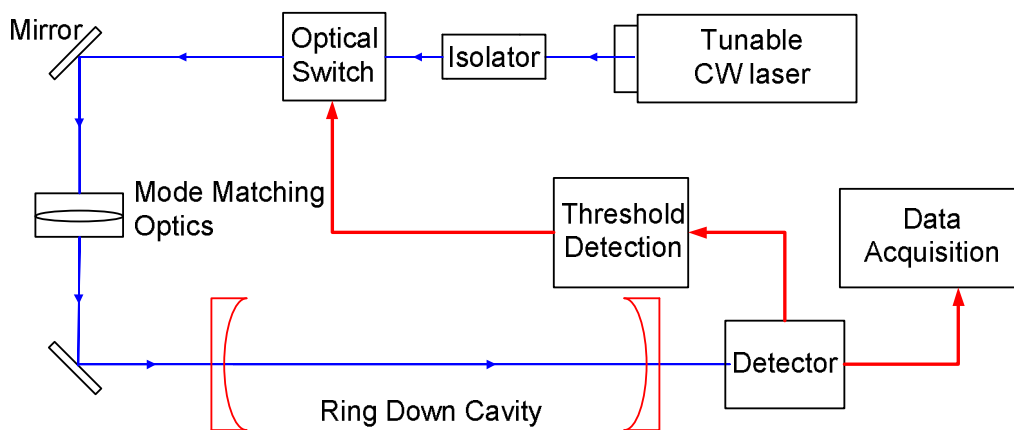


**Figure 2.4: Typical experimental setup of CW-CRDS.**

The emergence of tunable semiconductor lasers, including external-cavity diode lasers (ECDL), distributed feedback lasers (DFB), vertical-cavity surface-emitting lasers (VCSEL) and so on, has provided more choices of light sources for CW-CRDS besides tunable dye lasers. Tunable diode lasers generally have very narrow linewidth (1.0 to 20 MHz) and fast frequency scan speed ( $\sim 10^8$  GHz/s or higher), which easily increases the ring-down acquisition rate to several hundred Hz or higher. However, the tuning range of a diode laser is small and limited to a few nm or less. One needs to select a specific diode laser that usually works only for one target species. In addition, an isolator after the laser output is required to prevent unwanted reflection feedback into the laser source, which would otherwise affect the laser's coherence, or even damage the diode itself. Overall, diode lasers are very reliable, inexpensive, and compact. Diode lasers are amenable to practical *in-situ* detection systems.

In order to yield a clean ring-down event, the incident light should be extinguished during the ring-down event. One of the common solutions for this problem is adding an optical switch along with threshold detection as shown in Fig. 2.4. The threshold detection is typically a comparator that generates a switching signal (e.g. a TTL pulse), when the intensity of light inside the cavity (or the amplitude of the signal from detector) reaches a certain value (threshold). The switching signal controls an optical switch to quickly block the laser from entering the cavity for a period of time and yield a smooth ring-down decay. Another function of this threshold detection is mode selection. The energy coupling efficiency for fundamental modes in CW-CRDS is much higher than that for higher order modes. The threshold is set such that only the excitation of fundamental modes can trigger a ring-down event and be measured.

Among different optical switches, an acousto-optic modulator (AOM) is commonly used in CW-CRDS due to its fast switching speed and high extinction ratio (~40-100 dB). An AOM uses the acousto-optic effect to control the transmitted power, frequency or spatial direction of a laser beam with a radio frequency (RF) electric drive signal as shown in Fig. 2.5.

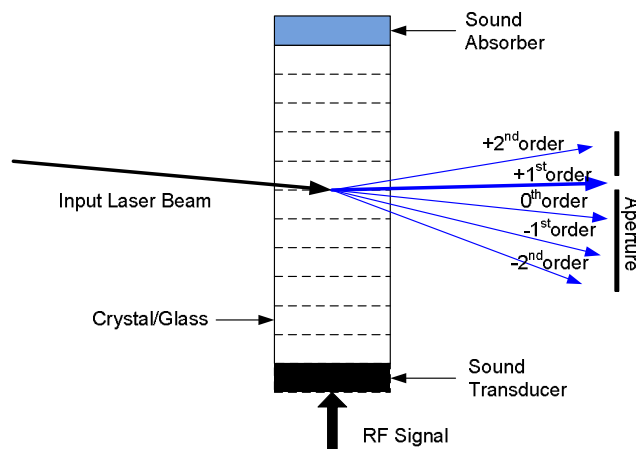


**Figure 2.5: Schematic of an AOM.**

A sound transducer (usually a PZT) converts the RF signal into sound wave in the crystal, which forms a refractive index variation across the crystal. A sound absorber is placed on the other side of the crystal and absorbs residual sound wave to suppress reflection. The input laser is deflected into different directions (orders) by the Bragg scatter from the crystal grating. The RF power, which determines the diffracted light power, is adjusted to maximize the laser power of the +1<sup>st</sup> order beam, which is then aligned to the ring-down cavity. The beam to the cavity (the +1<sup>st</sup> order beam) can be turned on/off very fast by controlling the RF signal on/off. Depending on the acoustic velocity inside the crystal, the contact position and the laser beam diameter, a typical switching time of an AOM is around 10 - 100 ns and fast enough for most CW-CRDS applications, although other optical switches (e.g. a Pockels cell) can also be used.

## **2.4. Summary**

CRDS techniques have been developed for roughly 20 years and used in various applications. There are many variations in actual experimental setups over the basic CRDS scheme discussed here. Generally speaking, CW-CRDS systems are faster, more sensitive, and more compact and less expensive than P-CRDS systems. They are capable of non-intrusively detecting low density particles in real time. As a result, we use CW-CRDS for real-time sputter erosion diagnostics of Hall thrusters.

## Chapter 3

### Manganese CW-CRDS Sputter Erosion Sensor

The CW-CRDS sputter erosion sensor is an opto-electronic system, which must also be integrated with a vacuum facility for sputter erosion diagnostics. Two different CW-CRDS setup configurations have been developed to detect sputtered manganese (Mn) atoms and boron (B) atoms. The Mn CRDS erosion sensor was developed first. The sensor detects the Mn atomic transition line  $3d^64s^2 \rightarrow 3d^5(^6S)4s4p(^3P)$  at 403.076 nm (air wavelength). The parameters for this transition line,  $E_i$ ,  $E_k$ ,  $A_{ki}$ ,  $g_i$ ,  $g_k$  are 0 eV, 3.075 eV,  $1.7 \times 10^7 \text{ s}^{-1}$ , 6, and 8, respectively, as quoted from the NIST database<sup>[71]</sup>. It is a strong absorption line in a relatively easy spectral range for CW-CRDS implementation. Thus, the Mn CRDS erosion sensor also acts as a stepping stone for the development of a BN CRDS erosion sensor. This chapter is devoted to the development and validation of the Mn CW-CRDS system.

#### 3.1. Sputtering Apparatus

For the purpose of sputtering diagnostic development, a simple sputtering apparatus with an ion source, as opposed to a full thruster, is used

The primary components of the sputtering apparatus and associated vacuum facility is shown in Fig. 3.1.

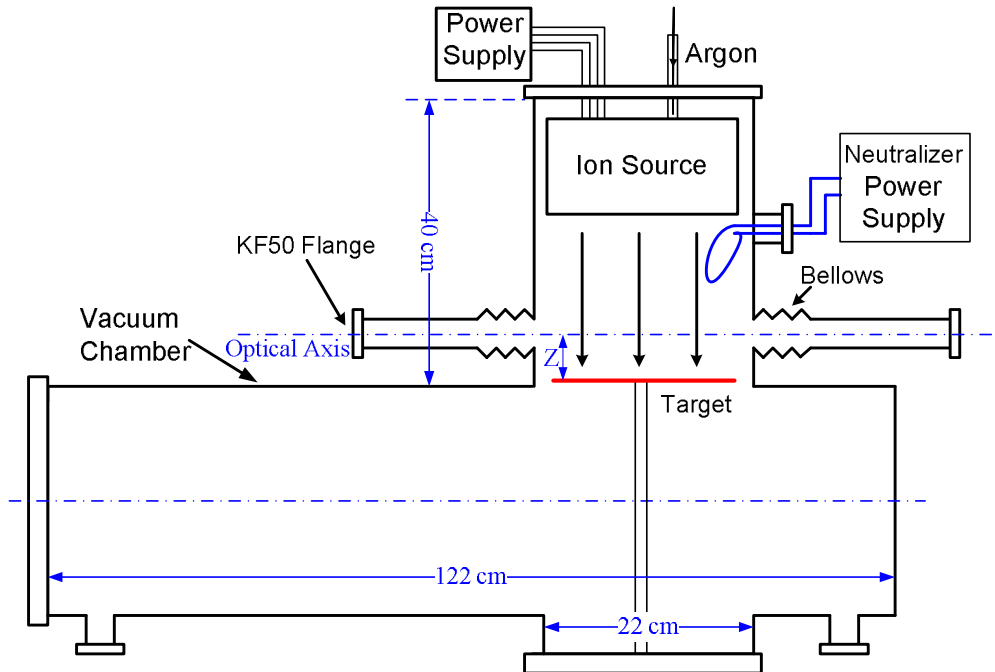


**Figure 3.1: Schematic of sputtering apparatus.**

The vacuum chamber comprises two separate cylindrical chambers. The 40-cm long smaller chamber has all the electric and gas feed-throughs for the ion source, while the 122-cm long larger chamber provides more room for the experimental apparatus. A roughing (mechanical) pump and a turbo-molecular pump (Turbo-V550) are connected in series to the vacuum chamber and bring the pressure of the whole chamber to approximately 0.1 mPa under no-flow conditions and to approximately 1 mPa under a small gas flow for the ion source. At both conditions, the sputtered atoms are in a free-molecular regime (Knudsen number  $\ll 1$ ), making the system representative of space conditions.

An 8-cm diameter structurally integrated two-grid ion source obtained from NASA generates the ion beam from an inert gas. A refractory metal (tungsten) filament is used as the cathode inside the ion source to provide electrons for ionization. Another tungsten filament is placed in front of the ion source as an ion beam neutralizer instead of a hollow cathode used in the original design. The ion source is powered by commercial power supply (MPS 3000), with typical beam currents and voltages of about 10-100 mA and 300-1200 V, respectively. A thermal mass-flow controller controls the flow rate of high-purity (99.995%) argon or xenon gas. The ion beam is normally incident upon the sputter target, which is held several centimeters downstream of the optical axis on a length adjustable post.

Two extended arms with flexible bellows are connected to the small chamber and form an 83 cm-long optical detection channel. Two mirror mounts, custom made for 1 inch diameter mirrors and blank KF 50 flanges, are connected at both ends of the detection channel. The mirror mounts are mechanically and thermally isolated from the main chamber body with flexible vacuum bellows. Inside each extended arm, several baffles (irises) with a ~10 mm center hole are used to (geometrically) protect the mirrors from sputtered particles and emission light from plasmas. A special optical rail system has been developed for thruster testing and, in some experiments, serves as the optical axis inside the large chamber. Fiber optics are used to deliver light in/out of the vacuum chamber. Details of the rail system are discussed later.

## 3.2. Mn Sputter Erosion Sensor

The Mn sputter erosion sensor has been developed and tested with the aforementioned sputtering apparatus. The sensor is designed to perform real-time measurements of sputtered Mn atoms. It is similar to the basic CW-CRDS scheme explained in Chapter 2, while more details are explained here.

### 3.2.1. Laser Source for Mn Detection

A tunable external cavity diode laser (ECDL) operating at around 403 nm is used as the light source to detect sputtered Mn atoms with CW-CRDS. CW light is generated in a single mode Fabry–Pérot laser diode, which is temperature controlled by a Peltier thermoelectric cooler. The tunable ECDL (Toptica, DL-100) has a Littrow configuration<sup>[72]</sup> as shown in Fig. 3.2. The Littrow configuration contains a collimating lens and a diffraction grating as the end mirror. The first-order diffracted beam from the diffraction grating provides optical feedback to the laser diode, which has an anti-reflection coating. The emission frequency of the laser is first tuned close to the selected resonance frequency of Mn atoms by changing the grating alignment with fine adjusting screws. The wavelength is swept across the resonance frequency by rotating the diffraction grating with a PZT, which is driven with a triangle wave voltage signal (~100V) generated from the controller of the ECDL. The Topitca DL-100 is capable of a ~30 GHz mode-hop free scan (single frequency laser output) with ~10 mW of output power. An optical isolator has also been integrated into

the ECDL system to prevent unwanted optical feedback. At the output end of DL-100, the beam is coupled into a single mode fiber.

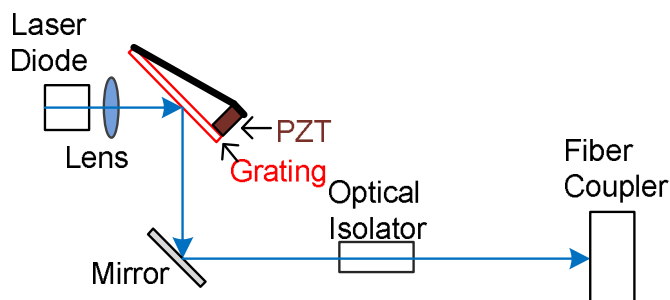


Figure 3.2: Schematic of the ECDL.

### 3.2.2. Experimental Setup for the Mn Erosion Sensor

A schematic of the experimental setup for the Mn CW-CRDS system is shown in Fig. 3.3.

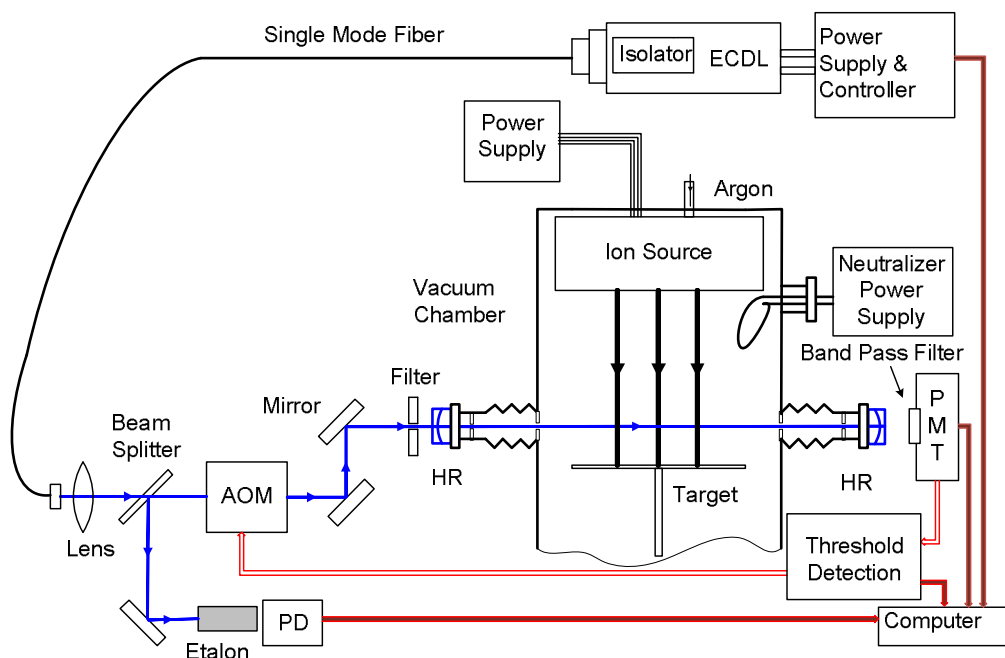


Figure 3.3: Schematic of CW-CRDS with mirrors outside the vacuum, PD: Photo detector, HR: High reflector.

The single-mode fiber guides the laser from the ECDL to an aspheric lens, which collimates the beam and matches the beam to the fundamental mode of the optical cavity. A beam splitter directs about 10% of the beam power to a solid fused silica Fabry–Pérot etalon (length 45mm, finesse  $\sim 2$  at 390 nm). A frequency reference signal for the laser is generated by the Fabry–Pérot etalon and detected by a photo-diode detector. The remaining 90% of the beam goes to an AOM which, along with a custom detection circuit, is used as a fast optical switch to extinguish the beam. The AOM (NEOS Tech.) is designed for 400-850 nm with a diffraction efficiency of 85% for light, which is polarized perpendicular to acoustic propagation. Only the first order output beam from the AOM is delivered to the optical cavity. The total response time of AOM and the trigger circuit is less than 400 ns. The optical cavity length is 0.83 m and is formed by a pair of high reflectivity mirrors (Los Gatos Research,  $R > 99.995$ ), each 25.4 mm in diameter with 1 m radius of curvature. A photomultiplier tube (PMT, Hamamatsu R9110 with a DA-type socket C7247) with a dielectric interference filter (center wavelength at 405 nm and a transmission bandwidth of 30 nm) is placed behind the cavity to detect the ring-down signal. When the signal from the PMT is higher than the pre-set threshold value, the threshold detection circuit generates a trigger pulse with a width much longer than the ring-down time. The trigger pulse turns off the AOM and yields a ring-down signal. The empty-cavity ring-down time of this system is typically  $\sim 20 \mu\text{s}$ , corresponding to  $R \sim 99.986\%$  (close to the specifications). The

experimental scheme employed here provides sufficient sensitivity and spectral resolution for our purposes. In comparison to methods in which a cavity mirror is scanned on a PZT, it is simpler and less expensive as desired for a robust (industrially oriented) monitor.

### **3.2.3. Data Acquisition System**

A computer based data acquisition system has been developed with a custom Labview program to collect and analyze experimental data. As shown in Fig. 3.3, multiple signals are analyzed by the computer system. We use an analog-to-digital (AD) acquisition board (Adlink PCI-9812), which has four single-ended simultaneous channels with sampling rate up to 20 MHz and a resolution of 12-bit for a bipolar signal input ( $\pm 5V$  and  $\pm 1V$  selectable). All measurements are made by scanning the laser wavelength; ring-down signals are measured each time the laser spectrally overlaps with a cavity transmission peak. In other words, the ring-down acquisitions are spaced by the cavity free spectral range. The trigger pulse, generated for each ring-down signal from the threshold detection circuit, also serves as the digital trigger in the AD acquisition board. When the A/D board is triggered, it digitalizes the signal from PMT, thus collecting a ring-down signal to the computer. Figure 3.4 is an example of the collected cavity transmission in Labview as the laser wavelength is swept.

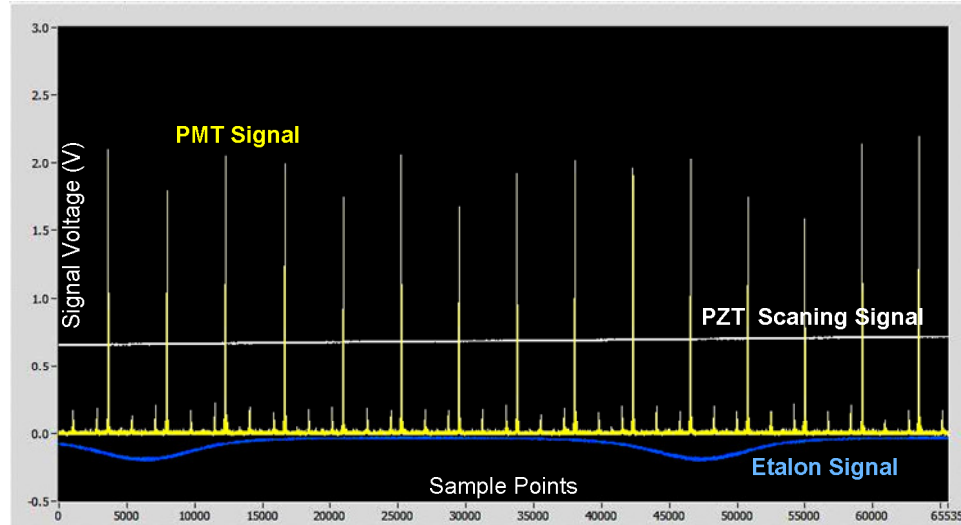


**Figure 3.4: Sample graph of collected signals in Labview.**

The regularly spaced taller transmission peaks are fundamental cavity modes, while other small cavity peaks originate from higher-order cavity modes. The amplitude of the fundamental cavity modes is usually more than 15 times higher than that of higher cavity modes with a good mode matching process. For the conditions in Fig. 3.4, a threshold voltage in the range of 0.5-2 V allows for an unambiguous selection on the fundamental cavity modes. The ring-down time is extracted from an exponential fit with the nonlinear Levenberg–Marquardt fit in Labview.

In addition, the signal from the photo-detector placed behind the etalon and the PZT voltage scan signal are also captured by the AD card in order to obtain the frequency information of the laser as in Fig. 3.4. Both signals are scaled into the measurement range of AD card with custom amplifier circuits. In laser spectroscopy, one of the central problems is accurate determination of

wavelength (or frequency). The most common way is to read the absolute wavelength of the laser through a wavemeter. The wavemeter we have is neither fast nor precise enough for real time monitoring for CW-CRDS system, which generates ring-down signals at a rate of hundreds of times per second. The relative laser frequency-PZT voltage relation is characterized at a certain temperature before each experiment as a wavelength calibration procedure. Figure 3.4 shows both the PZT voltage signal and the corresponding etalon signal for one scan period. The position of each etalon transmission peak and the corresponding PZT voltage can be identified with Labview. The frequency difference between successive transmission peaks of the Fabry–Pérot etalon is  $\sim 2.26$  GHz, which provides a measurement for the relative frequency of the laser. From this, the relation between the PZT voltage signal and the relative laser frequency can be determined.

However, the displacement of the PZT (and therefore laser frequency) is nonlinear with applied voltage and suffers from hysteresis and drift<sup>[73]</sup>, due to the open-loop control of the PZT. If the voltage applied to an open-loop PZT is increased from zero, the PZT displacement versus voltage curve follows path 1 as shown in the bottom of Fig. 3.6. Then, if the voltage is decreased, path 2 is followed. Path 3 is followed when the voltage is increased again. If the voltage is scanning between two fixed points, the PZT displacement follows the closed loop defined by path 2 and 3.

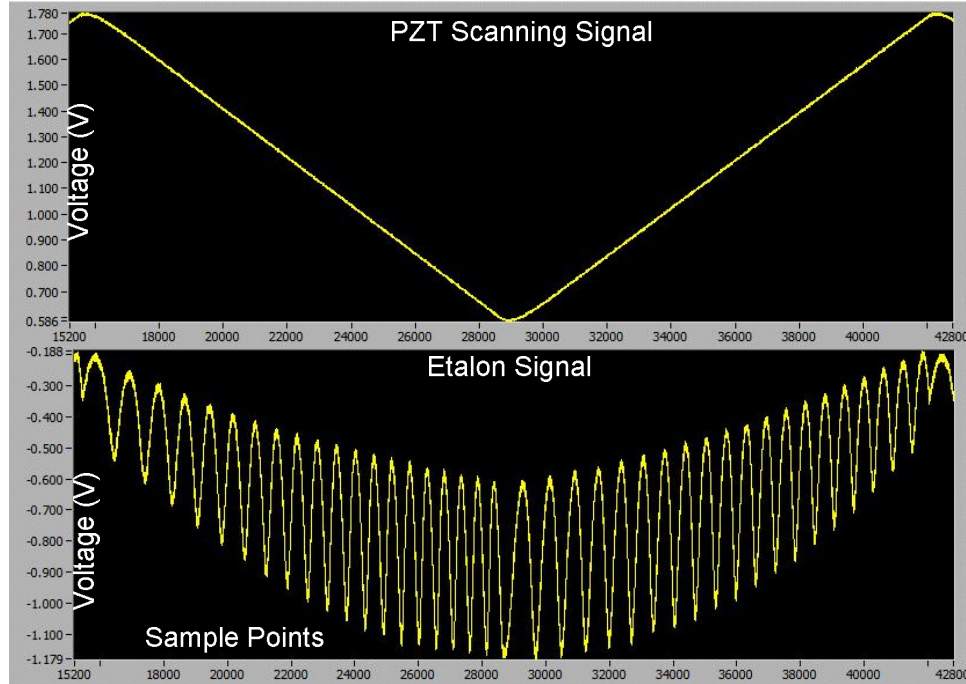


Figure 3.5: Graph of PZT signal and corresponding etalon signal.

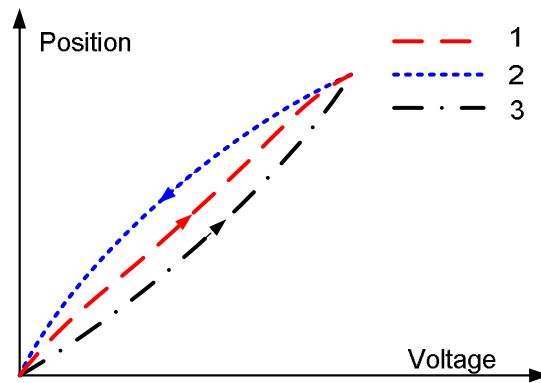
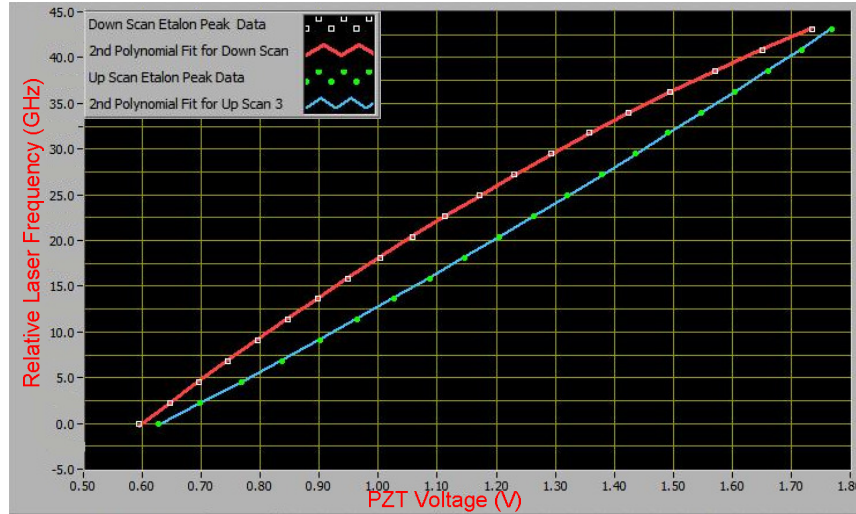


Figure 3.6: Simplified schematic representation of the hysteresis loop.

Accordingly, the frequency tuning of the ECDL, which is directly related to the PZT displacement, has a similar hysteresis relation versus PZT voltage. Different fittings are needed for ramping up and ramping down of the PZT voltage signal. Figure 3.7 shows fitting curves between relative laser frequency

and the PZT voltage with the same data as in Fig. 3.6. Two separate second-order polynomial fittings are used to characterize the relative laser frequency-PZT voltage relation for different voltage scan directions.



**Figure 3.7:** Graph of fitting curves for wavelength calibration in Labview.

The wavelength calibration is performed before each measurement campaign, while the temperature and voltage scan range are already stabilized. While the ring-down signal is captured, the AD card also records the corresponding PZT voltage, the derivative of which shows scan direction. Using the fitting parameters from the wavelength calibration, the relative frequency of the laser is calculated.

### **3.3. Demonstrative Measurements of Mn Erosion Sensor**

Demonstrative tests of the Mn CW-CRDS erosion sensor have been done, including measuring the Mn hyperfine spectrum and relation studies between the measured Mn number density and ion beam parameters.

The targeted Mn transition line  $3d^5 4s^2 \rightarrow 3d^5 ({}^6S) 4s 4p ({}^3P)$  at 403.076 nm has hyperfine structure. Hyperfine structure may be due either to slight differences between the spectra of different isotopes, or to the interaction of the electronic angular momentum with the nuclear spin. Mn, with only one common isotope, does not display the isotopic effect. The nuclear spin interaction causes splitting on the order of 50 pm or less between spectral lines. The Mn transition line is split into multiple hyperfine structure lines, which can be treated as 5 strong lines. These hyperfine splittings relative to 403.076 nm and their relative strengths are as follows: 0 pm (100), 1.580 pm (84.6), 2.883 pm (69.2), 3.917 pm (53.8), 4.686 pm (38.5), and 5.197 pm (23.1)<sup>[74]</sup>.

The hyperfine structure of the Mn was detected from a sputtered manganese-iron alloy target (8 cm × 4 cm, 50% Mn and 50% Fe by mole ratio). An aluminum honeycomb structure (3 cm high, 1 cm edge hexagon) was used as shown in Fig. 3.8. It was mounted on top of the Mn/Fe target to reduce Doppler broadening<sup>[57]</sup> which would dominate the hyperfine structure of the spectrum and preclude its detection. The axis of the honeycomb cells was aligned normal to the target surface so that the incident ion beam is minimally affected en route to the target. The side-walls of the honeycomb acted as a directional filter allowing only particles emitted approximately normally to the target surface to escape. The result is that the particles in the CRDS measurement region are more orthogonal to the optical axis and have smaller Doppler shift contributions, preserving the hyperfine structure.



**Figure 3.8: Aluminum honeycomb structure.**

The diode laser was set for a 30 GHz mode hop free frequency scan every 0.5 second. The absorption spectrum (and path-integrated number density) of Mn was measured. The optical axis was 2 cm above the top surface of the honeycomb structure. The ring-down acquisition rates of this system reached as high as  $\sim 300$  Hz. During the experiment, the ion beam current and voltage were set at 120 mA and 750V, respectively. Figure 3.9 shows the measured Mn hyperfine spectrum with a modeled spectrum. To construct the spectrum, we used a binning approach in which the frequency axis was divided into a series of bins, each with width 1 GHz, and signals falling within the bin were averaged. The wavelength-integrated area of the spectrum (found by numerical integration) yielded the path-integrated concentration. The model uses hyperfine shifts and relative strengths mentioned above. To incorporate the geometry of the honeycomb, we assume that particles sputtered with angles larger than 20 degrees from the surface normal make no contribution to the signal. The laser lineshape is not included in the model owing to its small

width (~5 MHz) relative to the measured and modeled features. The relatively good agreement between modeled and measured spectra is taken as validation of the main features of the CRDS measurement system. The wider wings of the experimental lineshapes in the data relative to the model are primarily owing to a background Mn signal caused by the outer portions of the ion beam hitting the (stainless steel) chamber wall. The existence of the background signal has been verified by masking the target with Kapton foil, in which case a weak Mn absorption was still measured with the feature of an amplitude consistent with providing the aforementioned wings.

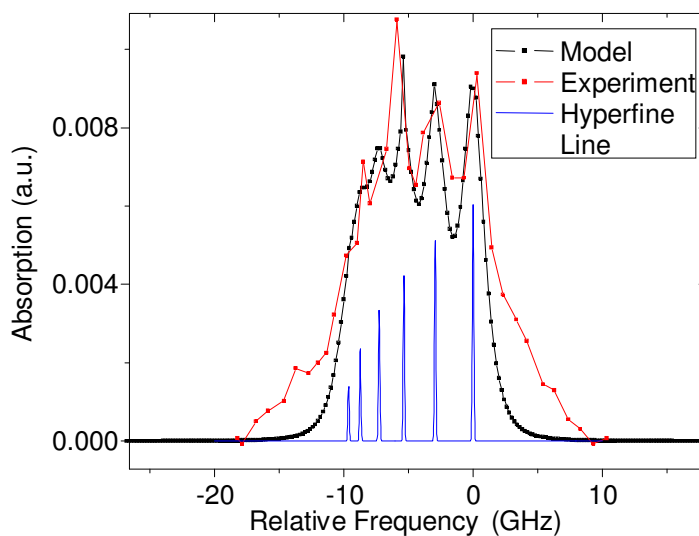


**Figure 3.9: CRDS Mn hyperfine structure and the modeled spectrum.**

The path-integrated concentration of sputtered Mn atoms can be readily calculated from the wavelength-integrated area of the spectrum with eqn. 2.7. Figure 3.10 shows an example of the dependence of the measured Mn

concentration on ion beam current. Each point was measured in 1-s. The linear density of Mn is proportional to the beam current (the fit correlation >99.8% in the linear fitting) as expected based on operation of this source in this current range. The fitted line doesn't go through the origin due to the backstreaming of the ion source. The actual current of ion beam was smaller than the recorded one from the power supply. The measured values of Mn concentration compare favorably with simple estimates based on the ion beam current profile, target dimension, and tabulated sputter yields. Data in Fig. 3.9 were obtained with a honeycomb on the target but the same method is used without the honeycomb.

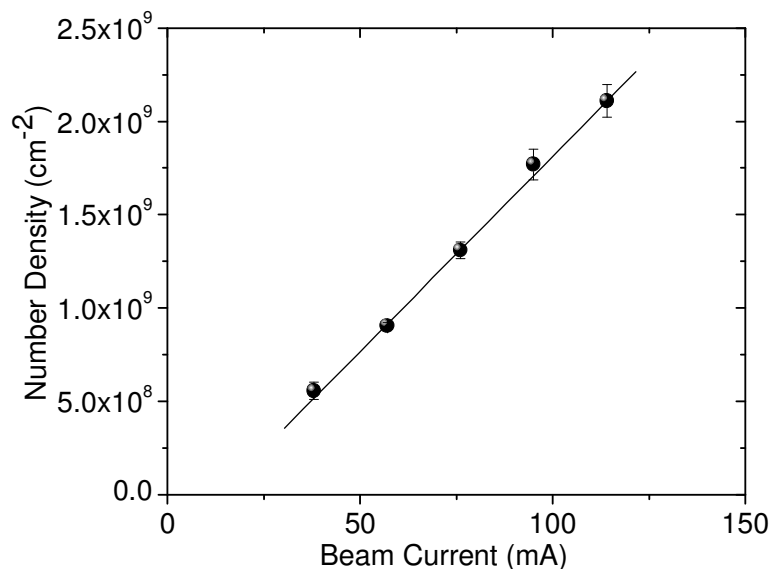


**Figure 3.10: Dependence of path-integrated number density of Mn on ion beam current.**

### **3.4. End-point Detection**

The purpose of developing a Mn sputter detection system is useful not only for real-time sputtering monitoring in EP thrusters, but also for end-point

detection in sputter coating system. For the latter application, Mn is of interest owing to its relatively common use as a layer in producing multilayer thin film head structures in commercial ion beam etch systems. A particular need in industrial ion beam sputtering systems is end-point detection<sup>[75]</sup>, i.e. the capability of detecting when a given layer of a multi-layer target has been fully etched through (reached its end-point) and a new underlying layer has been exposed. Current monitoring and end-point detection methods are typically based on either optical emission spectroscopy (OES) or secondary ionization mass spectrometry (SIMS). The OES method works well under certain conditions, but can suffer from interferences of background beam/plasma interactions within the etch process chamber. The primary shortcoming of the SIMS approach is the relatively high complexity and cost.

An end-point demonstration based on CRDS detection of Mn has been demonstrated with a multilayer target comprised of alternating layers of Mn/Fe (500 Å thick) and titanium (200 Å) as shown in Fig. 3.11.

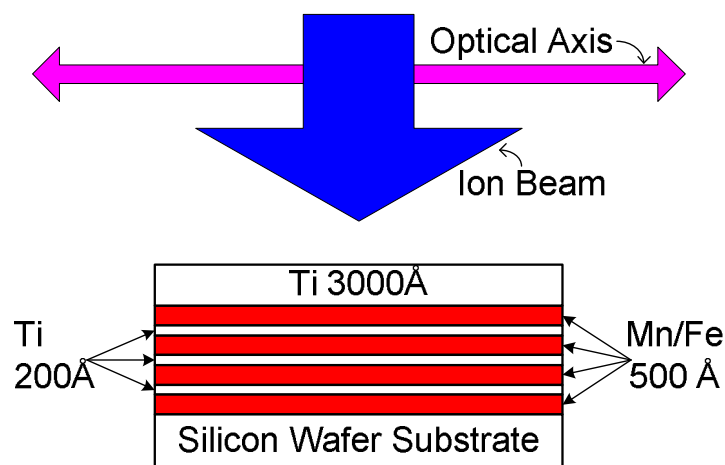


**Figure 3.11: Schematic diagram of sputtering multilayer target.**

The layers were initially sputter deposited onto a silicon wafer substrate. A top layer of titanium (300 nm) must be sputtered before reaching the alternating layers containing Mn. The dimensions of the target surface were 0.5 cm by 0.5 cm. The end-point detection was based upon measuring the time-dependence of sputtered Mn atom concentration, while the target was etched by the ion beam. A baseline contribution ( $\sim 10^8 \text{ cm}^{-2}$ ) is subtracted, which is associated with residual Mn deposited on the vacuum chamber walls being sputtered by divergent ions. In this experiment, the diode laser scan interval was 30 GHz with a scan period of 1 s. The ion beam current and voltage were 100 mA and 600 V respectively. Figure 3.12 is a plot of measured path-integrated Mn number density versus time. Blue guide lines mark the presence of Mn layers.

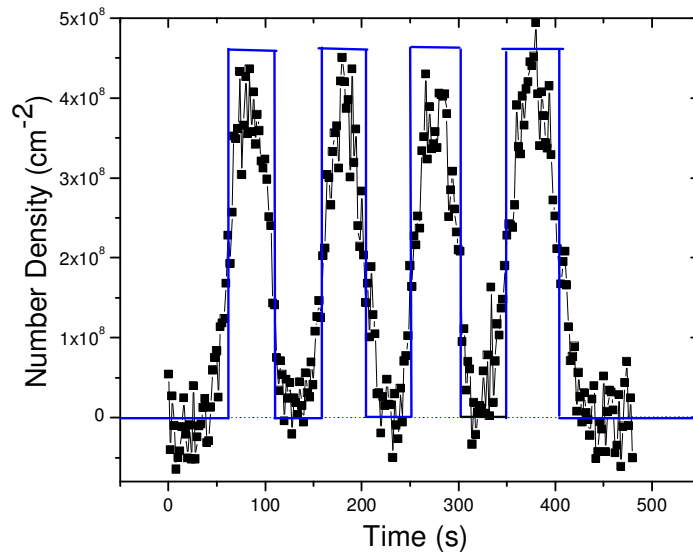


**Figure 3.12: End-point detection experimental result.**

The CW-CRDS detection system can readily detect the appearance and ending of the Mn-containing layers. To construct the spectrum, we again used a binning approach. The rounded profile of each layer may be due to non-uniformity of the ion beam current density and ion mixing in different layers. The non-uniformity leads to varying sputter rates over the target area so that layers start and finish at slightly different times at different locations on the target.

The time duration of each Mn/Fe layer was approximately 50 seconds, corresponding to etching rates of approximately  $\sim 10 \text{ \AA/s}$  for the  $500 \text{ \AA}$  thick layers. The observed etch rates of  $\sim 10 \text{ \AA/s}$  agree reasonably with a simple numerical estimate of  $\sim 15 \text{ \AA/s}$  based on the average ion current density ( $j = 1.3 \text{ mA/cm}^2$ ), expected sputter yield ( $Y = 1.51 \text{ atoms/ion}$  based on averaging single-species yields of  $Y_{Mn} = 2.01 \text{ atoms/ion}$  and  $Y_{Fe} = 1.00 \text{ atoms/ion}$  for 600 eV argon ions<sup>[76]</sup>), effective molar mass and density (using average of Mn and Fe values), and the target thickness. The experimental titanium etch rate of  $\sim 4 \text{ \AA/s}$  ( $\sim 200 \text{ \AA} / 50 \text{ s}$ ) is also reasonably consistent with a similar numerical estimate of etch rate of  $\sim 7 \text{ \AA/s}$  (found analogously to that described above but with titanium properties and  $Y_T = 0.53 \text{ atoms/ion}$ <sup>[76]</sup>)

The experimental result shows great potential in applying CW-CRDS erosion sensors to real-time sputtering diagnostics. Industrial ion beam etch systems typically have sputter (etch) rates of  $\sim 100 \text{ \AA/Min}$  and employ targets with  $\sim 10\%$  exposed area corresponding to concentrations of sputtered particles

of  $\sim 10^8 \text{ cm}^{-3}$  (for typical materials). Typical target sizes are  $\sim 10\text{-}30 \text{ cm}$  corresponding to path-integrated number densities of  $\sim 1\text{-}3 \times 10^9 \text{ cm}^{-2}$ . Layer thicknesses are  $\sim 10\text{-}100 \text{ \AA}$  so that a measurement rate of  $\sim 1 \text{ s}^{-1}$  is desired. Relative to these parameters, the demonstrated CRDS monitor is very adequate with a detection limit of approximately  $3 \times 10^7 \text{ cm}^{-2}$  for 1-s measurement times (corresponding to optical absorption sensitivity of  $< \sim 10^{-8} \text{ cm}^{-1}$ ). The system exhibits sufficient signal-to-noise for unambiguous endpoint detection at comparable or lower number densities to those in industrial etch systems. (Of course such evaluations would need to be performed for different species of interest, but Mn is reasonably representative in its properties.) In comparison to industrial systems, we used higher etch rates but smaller targets. For applications using small features on large substrates, or non-uniform ion beams, the effects of smeared end-point signals would need to be examined. Similar implementations could be used for other etching configurations, for example diode etching.

### **3.5. Hall Thruster Erosion Measurement with Mn CRDS Sensor**

Further demonstrations with the Mn CRDS Sensor have been done by performing Hall thruster erosion measurements. A different and larger vacuum facility (described below) was used to house the Hall thruster. A custom optical rail system was developed for fiber implementation of the Mn CRDS sensor to work in the Hall thruster vacuum facilities.

#### **3.5.1. Optical Rail System**

The optical rail system is a custom-designed self-contained unit that allows the cavity and delivery optics to be conveniently installed inside the vacuum chamber. The goal is to have a portable and flexible system that can be used in different vacuum facilities. As shown in Fig. 3.13, the rail system includes custom made aluminum end plates connected by carbon fiber rods and a base plate. The three carbon fiber rods have a near-zero coefficient of thermal expansion (0 CTE)<sup>[77]</sup>, which helps prevent optical misalignment from rod deflection under heat loading by the Hall thruster (or ion source). The end plates are designed to slide axially along the three rods, allowing for an adjustable cavity length. On these end plates, a 30 mm optical cage system (Thorlabs) is mounted to house optics, including fiber connectors, alignment optics, and high reflectivity cavity mirrors. Two 10 cm long tubes containing a series of 2 mm irises inside are mounted to the wall plates in front of each mirror in order to protect the mirrors from sputter deposition and excess exposure to ultraviolet light, both of which can degrade mirror reflectivity. This allows longer operation time (tens of hours) with minimal degradation of mirror reflectivity, which would cause a reduction in detection sensitivity. Under the base plate, four rubber damping feet are used to minimize vibrations, especially those from the pump system. Two custom made feed throughs for the multimode fiber and single-mode fiber help deliver the fibers inside the chamber and seal the vacuum.

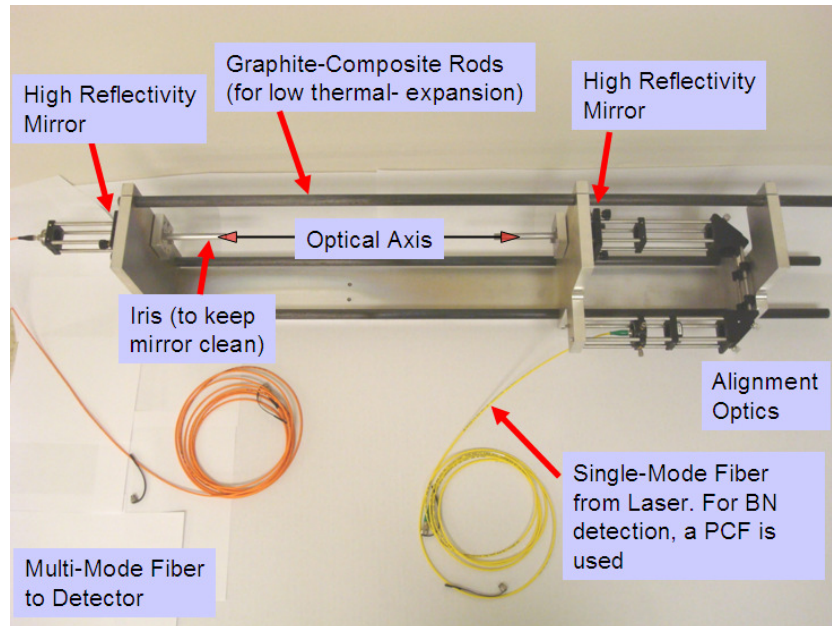


**Figure 3.13: Fiber-coupled rail for implementation within vacuum chamber.**

The modular design allows experiments to be conducted in various vacuum facilities with little or no modification. Moreover, the rail system allows for the optical setup to be tested and adjusted outside of the vacuum chamber while maintaining alignment as the chamber is pumped down. This is in contrast to the previous setup, in which the cavity mirrors were mounted on the outer walls of the vacuum chamber and suffered from alignment degradation as the chamber was pumped down or heated (and the walls deflected).

### **3.5.2. Hall Thruster Erosion Test**

A Hall thruster erosion test has been performed with a 1 kW class anode layer type Hall thruster developed at Kyushu University, Japan<sup>[78, 79]</sup>. In this Hall thruster, the acceleration channel is formed by a conductive material. The proof of principle CRDS experiments employed a stainless steel (SUS316) channel

and measured the sputtered Mn atoms from the stainless steel. The SUS 316 contains about ~1% Mn (0.81% from manufacturer's datasheet) and the CW-CRDS measurements are based on detection of the Mn sputtered from the channel wall. Figure 3.14 shows a cross section of the anode layer type Hall thruster<sup>[78]</sup>. The inner and outer diameters of the acceleration channel are 48 mm and 72 mm respectively. An inner solenoid coil and four outer solenoid coils create a predominantly radial magnetic field in the acceleration channel. The magnetic flux density is varied by changing the coil current. The separation between the acceleration channel wall and the anode is 1 mm. The thruster has a hollow annular anode, which consists of two cylindrical rings, with a propellant gas fed through them. The width of the hollow anode is 8 mm, and the gap between the tip of the anode and the exit of the acceleration channel is fixed at 3 mm. A hollow cathode is used as the electron source and pure argon gas is used as the propellant with thermal mass flow controllers (Brooks 5850E).

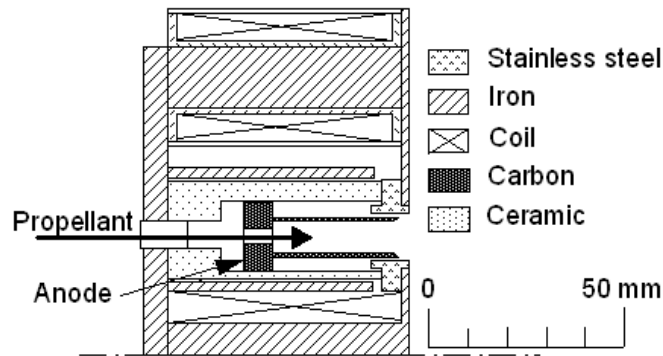


**Figure 3.14: Cross section of the anode layer type Hall thruster.**

The experiments were conducted in a larger vacuum chamber (1.5 m diameter by 4.6 m length) at the Colorado State University Electric Propulsion & Plasma Engineering (CEPPE) Laboratory. The pumping system includes a dry mechanical pump (Edwards GV250), assisted by a mechanical booster pump (Edwards EH-1200) and two diffusion pumps (Varian HS-20). The chamber baseline pressure is below  $7 \times 10^{-4}$  Pa. Figure 3.15 shows a photograph emphasizing the CRDS aspects. The laser was coupled to a polarization maintaining (PM) single mode FC/APC fiber, which went through the feed-through into the vacuum chamber. The entire rail system was mechanically and thermally isolated from the main chamber body with polyurethane dampers and Kapton foil cover. The optical axis was 3 cm downstream of the thruster and it intersected with the thruster centerline. Light exiting the cavity travelled through a multi-mode (MM) optical fiber to the PMT outside the vacuum chamber.

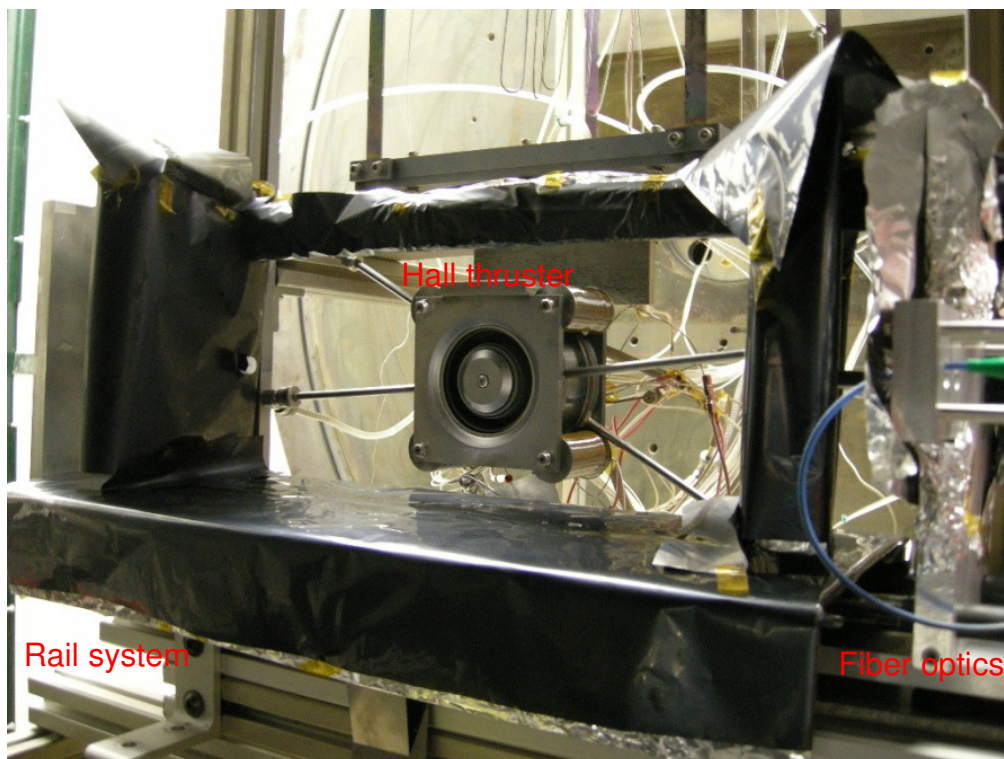


**Figure 3.15: Photograph of optical cavity hardware inside the vacuum chamber.**

A sample CRDS spectrum from Hall thruster testing is shown in Fig. 3.16. For this test the discharge voltage was 150 V and argon mass flow rate was 70 sccm. Again, to construct the spectrum, a binning approach was used by dividing the frequency axis into a series of bins, each with width 1 GHz, and signals falling within the bin were averaged. The laser tuning range was not sufficiently large enough to scan over the full line width, which was considerably broadened in the Hall thruster (primarily due to geometric effects leading to larger Doppler shifts). As a result, the spectrum area was calculated by doubling the value found by numerical integration of half of the lineshape (the low-frequency side). For the data in Fig. 3.16, the path-integrated Mn

concentration was calculated to be  $8.2 \pm 1.5 \times 10^{12} \text{ m}^{-2}$  (where the uncertainty is partly due to the area fitting but still dominated by the 18% uncertainty in  $A_{ki}$ ).

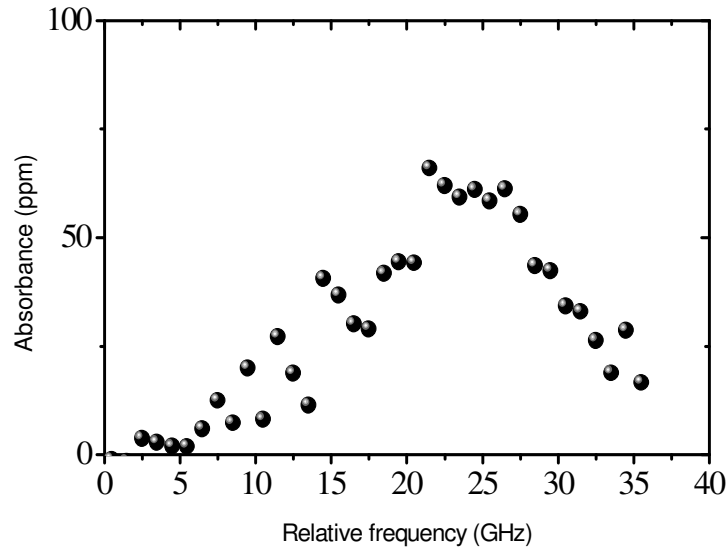


**Figure 3.16: Sample spectrum of Mn from Hall thruster test.**

In principle the measured Mn concentration should correspond to the number density of Mn atoms at the ground state. A Boltzmann analysis for a characteristic temperature of 1500 K shows that the ground state comprises >99% of the overall population. There is little reason to assume Boltzmann distributions for the sputtered particles due to lack of equilibrium in the sputtering process (and lack of collisions after ejection). Nonetheless, past research has generally shown distributions similar to a Boltzmann distribution with “temperatures” generally in the range ~500-1500 K.<sup>[58]</sup> In some cases elevated “anomalous” populations of sputtered particles in upper energy levels have been observed, but the agreement between our CRDS and mass-loss makes it unlikely that such effects are significant in these experiments. The

possible effect of sputtered ground state atoms being excited to a higher level (or ionized) prior to reaching the measurement location should also be taken in consideration. Simple calculations show the “loss” of ground state atoms owing to these effects will change the signal by <10% at our conditions.

An initial study of dependence of sputter erosion on discharge voltage (150 V, 200 V and 250V) has been performed. Figure 3.17 shows the sputtered Mn number density measured through the thruster plume and mass-loss of one-hour duration for three different discharge voltages. The sputtered particle number density increases roughly linearly with discharge voltage. The reason is that the sputter yield of Mn increases with the bombarding argon ion energy, which increases with the discharge voltage. For CRDS validation, mass loss measurements were also performed at the corresponding conditions (with uncertainty of 5%) by weighting the stainless steel channel before and after one-hour thruster operation. The error bars on the CRDS erosion values ( $\pm 40\%$ ) were found from contributions due to possible variation of the sputter flux from each surface (we consider cases where each surface sputters at a rate of twice the others ( $\pm 16\%$ )), changes from diffuse sputter yield to an over- or under-cosine profile ( $\pm 5\%$ ), changing the exponent used in the Thomson distribution ( $\pm 32\%$ ), and the uncertainty in corresponding CRDS number density measurement ( $\pm 18\%$ ). The trend of mass-loss versus discharge voltage is in broad agreement with that for the CRDS results. Future measurements will spatially scan the exit plane of the Hall thruster by

translating the sensor up and down relative to the thruster. In that case, a spatial distribution of sputtered particles can be obtained. Related future efforts are discussed in Chapter 6.

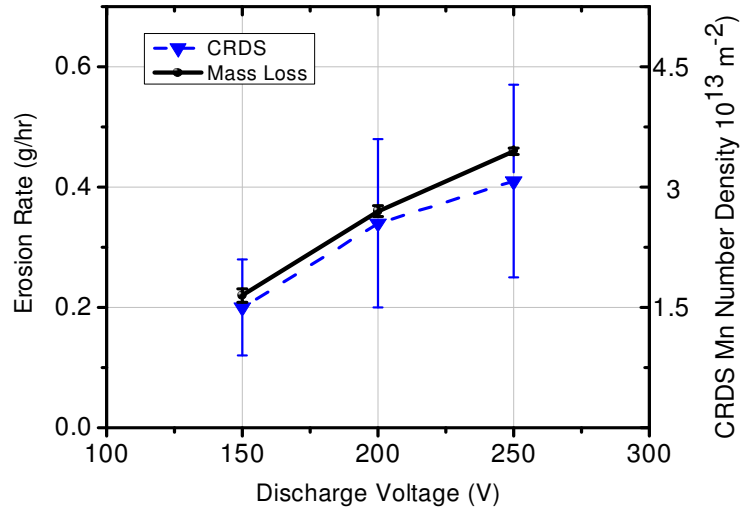


**Figure 3.17: Measured erosion rates from CW-CRDS and from mass loss measurement at different discharge voltages.**

### 3.6. Summary

In this chapter, the Mn CW-CRDS erosion sensor has been presented. It uses an ECDL as the light source to probe sputtered Mn atoms at the vicinity of 403 nm. A custom Labview program was used to collect ring-down signals and laser frequency with an AD acquisition board. Demonstrated validation experiments were performed including measurement of the hyperfine spectrum and the Mn atom number density dependence on incident ion beam in a simple sputtering apparatus. End-point detection is also demonstrated for potential industrial application for real-time detection in sputtering multi-layer targets.

The Mn erosion sensor exhibits sufficient signal-to-noise and time resolution for unambiguous endpoint detection.

In addition, demonstrative erosion tests for a 1 kW class anode layer Hall thruster have been done by detecting sputtered Mn atoms from the stainless steel acceleration channel. Fiber optics and a custom optical rail system were used for flexible implementation in a vacuum chamber facility. The measured Mn atoms number densities from the CW-CRDS sensor showed good agreement with mass-loss results. Both the CRDS number density and mass-loss showed a relatively linear dependence against discharge voltage as expected based on a simple analysis. The high time response and *in situ* nature of the CRDS sensor can be of great utility in understanding erosion rate trends, i.e. monitoring how the erosion signal varies with changes in thruster operating conditions.

## **Chapter 4**

### **Boron Nitride CW-CRDS Erosion Sensor**

The Mn CW-CRDS erosion sensor shows the possibility of a near real-time sputter diagnostic for industrial ion beam etch systems as well as an erosion sensor for detecting sputtered particles from an anode layer type Hall thruster. BN is the material of interest in most Hall thrusters (SPTs). In comparison to the aforementioned experimental work of probing Mn atoms at around 403 nm, the measurement scheme for sputtered BN is significantly more challenging as the needed absorption lines are in the ultraviolet region (250 nm). Challenges with CRDS in the ultraviolet include lower cavity mirror reflectivity (and therefore poorer detection limits) as well as difficulties in single-mode fiber optic delivery which. This chapter describes to the development of a BN CW-CRDS erosion sensor.

#### **4.1. Boron Nitride Detection Scheme**

The approach for detection of BN is based on CRDS absorption measurement of sputtered boron atoms. The exact composition of the sputtered particles from BN, i.e. proportions of B, N,  $B_xN_y$  etc., is not well understood and may vary with sputtering conditions. However, sputter yield

measurements with a quartz crystal microbalance (QCM) indicate that the majority of sputtered boron is in the form of boron atoms, perhaps with a small fraction of  $B_xN_y$  clusters [80, 81]. In addition, from the OES study of BN erosion in Hall thruster, optical emission light from excited Boron atoms was also reported [26, 34, 82]. The bombarding ions in the present experiments are mainly argon, while the past studies [80, 81] used xenon ions. In either case, both are heavy species relative to boron and nitrogen atoms. And it is reasonable to expect similar sputter products. It is possible that the sputtered nitrogen is in the form  $N_2$  or  $N_x$ , but this does not affect our measurements. Since atomic nitrogen is not a readily optically accessible species, atomic boron is chosen as the measurement species. In the analysis, we assume all sputtered particles are atoms so that each sputtered boron atom corresponds to ejection of one boron atom and one nitrogen atom from the BN surface. This assumption can later be refined based on species-specific sputter yield measurements and modeling [39].

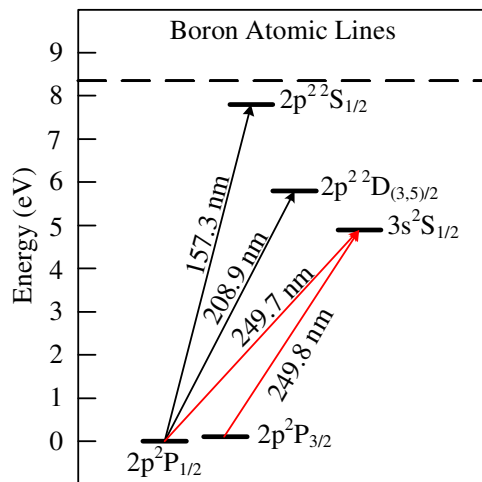


**Figure 4.1: Partial energy level diagram of atomic boron.**

A partial energy level diagram for neutral boron (B I) is shown in Fig. 4.1. The ground term has two distinct fine structure levels:  $2s^2P_{1/2}^0$  (0 eV) and  $2s^2P_{3/2}^0$  (0.00189 eV). The dashed line represents for the ionization energy of boron atoms. The fine-structure splitting results in two distinct B I absorption lines near 250 nm: the  $2s^2P_{1/2}^0 \rightarrow 3s^2S_{1/2}$  transition at 249.753 nm, and the  $2s^2P_{3/2}^0 \rightarrow 3s^2S_{1/2}$  transition at 249.848 nm. These lines are selected for CRDS measurement based on their optical accessibility and high absorption strength. Table 4.1 shows detailed energy levels, spontaneous emission rates (Einstein A coefficients), and wavelengths for the targeted absorption lines.

**Table 4.1: Table of boron atoms transitional information.**

$E_i$ ( $\text{cm}^{-1}$ )	$J_i$	$E_k$ ( $\text{cm}^{-1}$ )	$A_{ki}$ ( $\text{s}^{-1}$ )	$\lambda$ (nm)
0	1/2	40039.52	9.552E7	249.7533
15.15	3/2	40039.52	1.904E8	249.8478

The sputtered particles are in a non-equilibrium state due the collisionless environment of the vacuum chamber. Previous research<sup>[58, 83]</sup> shows that the actual population distributions of sputtered atoms sometime do not follow equilibrium Boltzmann distributions. In a Boltzmann distribution, the fractional number of particles  $N_i/N$  occupying a set of state  $i$  possessing energy  $E_i$  is calculated using a partition function  $Z(T)$ :

$$\frac{N_i}{N} = \frac{g_i e^{-E_i / (k_B T)}}{Z(T)} = \frac{g_i e^{-E_i / (k_B T)}}{\sum_i g_i e^{-E_i / (k_B T)}} \quad (4.1)$$

Despite the lack of rigorous validity of the Boltzmann statistics, a characteristic Boltzmann temperature  $T$  is often used. The minimum energy required to excite boron atoms from ground states to excited states is more than 4.5 eV. From the energy level information of boron atoms, more than 99.9% of the boron population is calculated to reside in the split ground state (66.6% of all population in  $2s^2P_{3/2}^0$ ) based on Boltzmann statistics with a characteristic temperature of 1500 K. To a good approximation, it can be assumed that the sputtered atom population will reside in the split ground state, meaning that the measured states will provide a direct measurement of the overall boron population. (This is in contrast to OES approaches which probe a small fraction of the sputtered particles residing in upper energy-levels.)

## 4.2. Boron Nitride CW-CRDS Erosion Sensor

A CW-CRDS erosion sensor was built to detect sputtered boron atoms from BN erosion in the vicinity of 250 nm. At this wavelength, the probe laser system is more complicated than the one used in Mn erosion sensor. Also The dielectric mirrors have poorer reflectivity, which results in short ring-down times and low sensitivity. As part of these experiments, a novel mean-of-signal mode fiber delivery for a single-mode laser beam at 250 nm was accomplished for the first time.

### 4.2.1. Frequency-Quadrupled ECDL System

Currently, there is no diode laser directly capable of emitting 250 nm light as needed for the selected boron absorption lines. As a result, a frequency-quadrupled ECDL system (Toptica TA-FHG110) was chosen as the continuous-wave light source for boron detection. This system comprises a 1- $\mu\text{m}$  ECDL system, a tapered amplifier diode and two second harmonic generator (SHG) cavities as shown in Fig. 4.2. The ECDL system has the same structure as the laser used in Mn erosion sensor and generates  $\sim 10$  mW laser light at the wavelength of  $\sim 1$   $\mu\text{m}$ . A tapered amplifier diode is used to amplify the 1- $\mu\text{m}$  laser power to  $\sim 300$  mW. After that, two SHGs quadruple the laser frequency and produce light around 250 nm. Each of SHGs has a bow-tie cavity that hosts the doubling crystal for second harmonic generation. The bow-tie cavities are actively locked to the laser using the Pound-Drever-Hall locking scheme<sup>[67]</sup> with a PZT attached to one cavity mirror. This laser system can generate a 60 GHz mode-hop free tuning range around the targeted transition lines of boron atoms, with a linewidth less than 5 MHz, and an output power of  $\sim 10$  mW. Because of the limitation of the laser scan range, it is not possible to probe both of the ground levels. As a result, the diode laser system was initially tuned to scan mode-hop free around the 249.848 nm, which is the stronger absorption line. However, the scan frequency of the laser system is limited, due to the stabilization of the laser locking scheme. Each scan takes about 12 s (up and down).

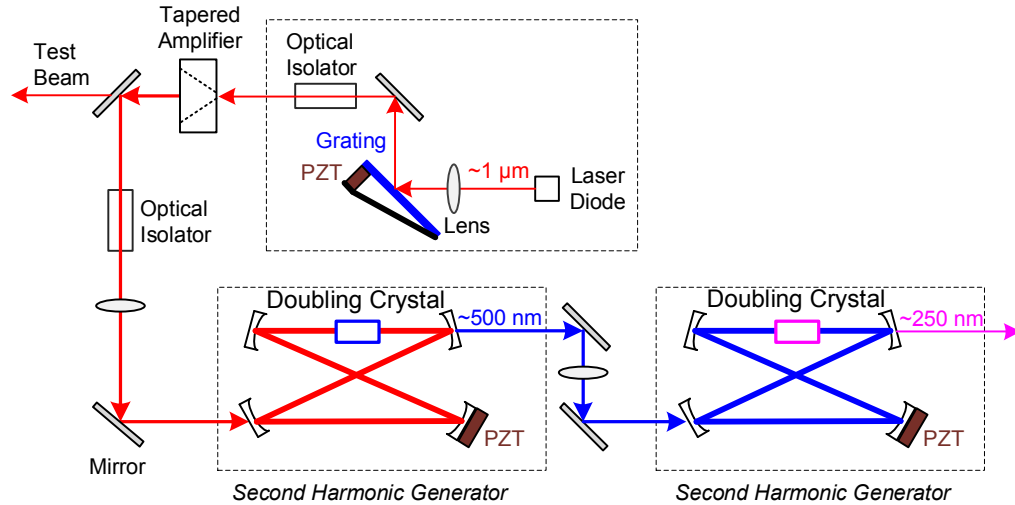


**Figure 4.2: Schematic of frequency-quadrupled ECDL system.**

#### 4.2.2. Experimental Setup of the Boron Erosion Sensor

The elements of the boron CW-CRDS setup are shown in Fig. 4.3. A beam splitter is placed in front of the laser and sends about 10% of the laser power through a solid Fabry–Pérot etalon (finesse  $\sim 10$  at 250 nm) onto a photodiode to generate a frequency reference signal. The rest of the laser beam goes through an AOM with a diffraction efficiency of  $\sim 70\%$  to the first order output beam. The first-order beam is coupled into the vacuum chamber using a 4 m single-mode photonic-crystal fiber (PCF) with a core diameter of  $\sim 10 \mu\text{m}$ . Specifics of the PCF delivery are given in the next section. All the optics in vacuum are hosted by the same custom rail system specified in Chapter 3. At the output of the PCF, two plane-convex fused silica lenses ( $f = 20 \text{ mm}$ ,  $f = 500 \text{ mm}$ ) are used to mode match the laser beam to the fundamental longitudinal mode (TEM<sub>00</sub>) of the cavity. The optical cavity is 75

cm long and is formed by two high reflectivity mirrors each 2.54 cm in diameter with 1 m radius of curvature. In this setup, an empty-cavity ring-down time of around 1.3  $\mu$ s is achieved, corresponding to R=99.8% for each mirror. The reflectivity is low relative to achievable values (>99.99%) in the visible and near-infrared, but is reasonable for dielectric layer mirrors in this spectral region. Behind the cavity, the output beam is coupled into an ultraviolet multimode fiber, which delivers light to a photomultiplier tube (PMT model Hamamatsu R9110) with a dielectric interference filter (Andover Corporation, AM-62344, with 30 nm band pass) to suppress the background light. Ring-down signals are measured each time the laser spectrally overlaps a cavity transmission peak during the wavelength scans of the ECDL. The trigger circuit causes the AOM to extinguish the light, resulting in a ring-down event measured by the PMT. A Labview based data acquisitions system, similar to the one in the Mn CW-CRDS erosion sensor, is used to record and analyze all measurements.



wavelength of light,  $a$  is the fiber core radius, and  $NA$  is the numerical aperture of the fiber. Fibers that allows single-mode operation should have a  $V$  value less than 2.405. In principle, a lower cutoff wavelength can be achieved by either reducing the value of  $NA$  at fixed core dimension, or vice versa. In the former case, the bending losses of the fiber increase and make the total loss of the fiber too high to be usable. While in the latter case, the size of the fiber becomes too small to get efficiency coupling of light into the fiber, and nonlinearity and UV damage must also be taken into account. For example, Bartula *et al.*<sup>[84]</sup> used a commercial single-mode fiber at 337 nm, but the core diameter of  $\sim 2 \mu\text{m}$  limited the coupling efficiency to  $< \sim 10\%$  owing to the difficulties of achieving diffraction limited spot sizes. (The exact coupling efficiency was not given in the aforementioned work, but the overall efficiency was 4% with a transmission loss of  $\sim 40\text{-}70\%$ .)

During the development of the boron erosion sensor, we have found that photonic crystal fibers (PCFs) can be used for single-mode delivery at the needed UV wavelengths<sup>[85]</sup>. Typical PCFs have a uniform patterned microstructure of holes (looks like a crystal) running axially along the fiber channel with a missing hole in the center providing a core region. In an equivalent index-of-refraction picture, the microstructure imposes a strong wavelength dependence on the index-of-refraction of the cladding, and for high light frequencies (short wavelengths) the cladding index approaches the core index. With appropriate fiber design, the fiber core can support a single guided

mode over all optical frequencies, a characteristic referred to as “endless single-mode operation”. For triangular, high-index core PCFs with circular hole defects, endless single-mode operation is achieved for  $d/\Lambda < \sim 0.4$ , where  $d$  is the hole diameter and  $\Lambda$  is the lattice spacing<sup>[86]</sup>. A useful feature of these fibers is that the endless single-mode characteristic can apply even for relatively large core dimensions (for which step-index fibers would be multimode) in which case they are termed LMA (large mode area) PCFs. A common use of LMA PCFs is to deliver high-power visible or infrared pulses, e.g. within fiber lasers. Whereas delivery of single-mode laser light around 250 nm through a PCF has never been done by anyone before.

#### **4.3.1. Laser Delivery with Photonic Crystal Fiber**

A LMA PCF (Crystal Fibre LMA-10 UV) with a core diameter of  $\sim 10 \mu\text{m}$  was employed for delivery of light from the laser to the cavity within the vacuum chamber for the Boron erosion CRDS sensor. The fiber has a single cell triangular structure with lattice spacing (pitch) of  $6.26 \mu\text{m}$ , hole size of  $3.04 \mu\text{m}$  ( $d/\Lambda = 0.485$ ) and is optimized for ultraviolet and visible operation<sup>[87]</sup>. For 250 nm operation, the fiber NA and mode field diameter (MFD) are  $\sim 0.03$  and  $\sim 8 \mu\text{m}$  respectively. Modeling shows these fibers to be endlessly single-mode with the relatively large  $d/\Lambda$  value mitigating the bending loss edge at short wavelengths, to promote UV operation.

The PCF fiber was tested with a setup as shown in Fig. 4.4. The frequency-quadrupled ECDL system operating at 249.7 nm was used as the

light source. Because the laser output beam has some astigmatism, a cylindrical lens ( $f = 100$  mm) near the laser output was used to roughly collimate the laser output. Although, the laser output was close to a single-mode Gaussian beam, a  $10\text{-}\mu\text{m}$  diameter pinhole as a spatial filter was placed at the focal point of the telescope to improve the beam quality for fiber launch. Even though the laser beam needs to pass through an AOM (prior to the spatial filter) in CW-CRDS experiments, the AOM does not appreciably affect the beams spatial quality. The fiber launch was designed to mode match the beam to the fiber input and used a plano-convex quartz lens ( $f = 50$  mm) for free-space coupling to the fiber. During the experiments, the fiber was mounted in a V-groove fiber holder on a precision 5-axis stage.

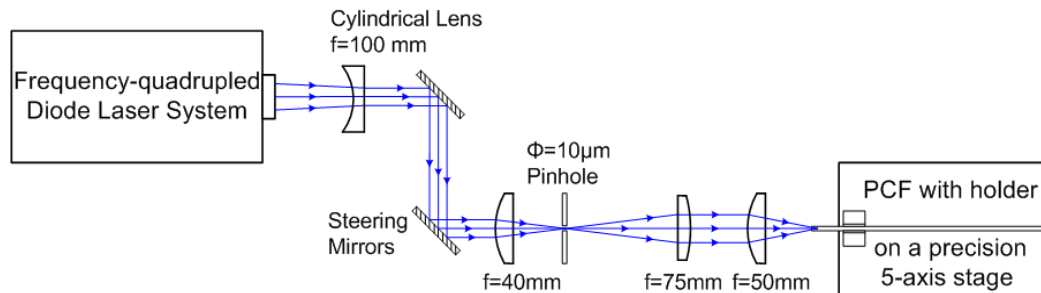


**Figure 4.4: Schematic diagram of fiber launch for PCF characterization.**

A photograph of the  $250$  nm PCF output as seen on a card several centimeters downstream of the fiber exit is shown in Fig. 4.5. The imaged light is due to fluorescence from dye on the card. The image is over saturated in the center region. The hexagonal shape of the beam pattern is typical of single-mode output from a triangular PCF<sup>[88]</sup>.

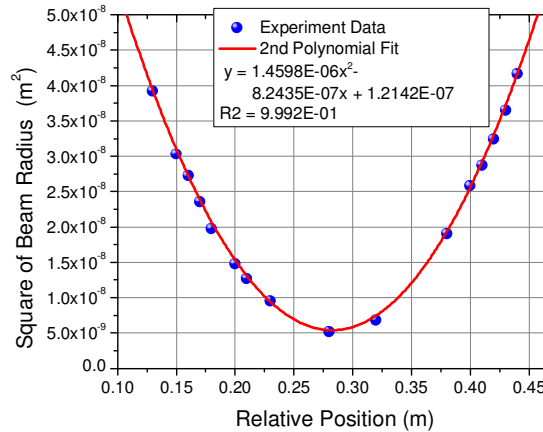


Figure 4.5: Photograph of single-mode output beam from PCF.

#### 4.3.2. Single Mode Output Validation

Single-mode output via the PCF was further confirmed in several different ways. First, the power transmission through a downstream pinhole was checked. A first lens was used to collimate the fiber output to a diameter of 0.8 mm and then a second lens of focal length 45 mm focused the light through a 30- $\mu\text{m}$  pinhole. In this way, a transmission efficiency of more than 90% of the laser power through the pinhole was achieved. Second, we have mode-matched the fiber output to a high-finesse CRDS optical cavity and coupled the light predominantly to the fundamental cavity modes (higher order modes exiting the fiber would couple to higher order cavity modes). Finally, as shown in Fig. 4.6, we have used a beam profiler (Spiricon SCOR20) to measure the beam quality factor (or beam propagation factor)  $M^2$  of the light exiting the fiber (length 1.3 m). The output beam was weakly focused using a plano-convex lens ( $f = 200$  mm) and the dependence of beam diameter on position resulted

in  $M^2 = 1.08$  ( $M^2 = 1$  for a perfect Gaussian beam) confirming (near) single-mode output. When the fiber launch was misaligned, we could still couple power through the fiber but the output did not appear to be single-mode and the NA tended to be lower. In these cases, light was presumed to be transmitted through the cladding. The fiber coupling was also very sensitive to mechanical conditions. Over-tightening of the spring-loaded V-groove could degrade the 249 nm delivery (both efficiency and output mode), while having no appreciable effect on 633 nm delivery, due to micro-bending losses<sup>[89]</sup>.



**Figure 4.6: Beam dimension versus relative position for  $M^2$  determination.**

#### 4.3.3. Transmission of the PCF

The transmission through the LMA PCF for the 250 nm laser has also been studied. Instead of performing a cutback test, the power transmission through fibers with several different lengths were measured to calculate the fiber coupling and transmission loss. Figure 4.7 shows the results for fibers of length between 0.45 m and 4 m. The laser power at the fiber input was ~1 mW.

For testing fiber lengths of  $< 3$  m, the fiber was held relatively straight, while for testing lengths of  $\geq 3$  m, the fiber was moderately bent with radius-of-curvature of roughly 0.5 m. Fiber bend loss is further discussed below. The transmission data are reasonably fit (the fit correlation equals 0.96) with a straight-line of intercept  $-1.8 \pm 0.6$  dB and slope of  $-1.5 \pm 0.2$  dB/m, corresponding to a coupling loss of  $\sim 34\%$  and transmission loss of  $\sim 29\%$  loss per meter. The scatter in the data may be due to optimization of alignment for each fiber, but is also likely related to optical damage discussed below. The coupling loss is reasonable for single-mode coupling at these short wavelengths, though some optimization may be possible with better mode-matching (e.g. reduction of aberration or improved combination of launch lens and beam diameter). The transmission loss can be converted to a (Beer's Law) absorption coefficient of  $a_\lambda = 0.35 \pm 0.05$  m<sup>-1</sup>. To find the corresponding absorption index (imaginary component of the index-of-refraction)  $k_\lambda$ , we use  $k_\lambda = \lambda/4\pi \cdot a_\lambda$ , where  $\lambda$  is the (free-space) wavelength, and find  $k_\lambda = (7 \pm 1) \times 10^{-9}$ . The value is somewhat low relative to published values for silica glass<sup>[90]</sup>, but there is considerable scatter and uncertainty in these measurements owing to the type of silica (natural versus synthetic), impurities, and measurement method (e.g. transmission based measurements cannot adequately resolve small losses). Another comparison can be made with extrapolation of the fiber data-sheet<sup>[87]</sup> using a  $\lambda^{-4}$  scaling (i.e. assuming loss is dominated by Rayleigh scattering) which gives  $\sim 0.25$  dB/m ( $k_\lambda = 1.2 \times 10^{-9}$ ) indicating that there is an

additional absorption contribution, likely from impurities (e.g. Cl) and micro-bending.

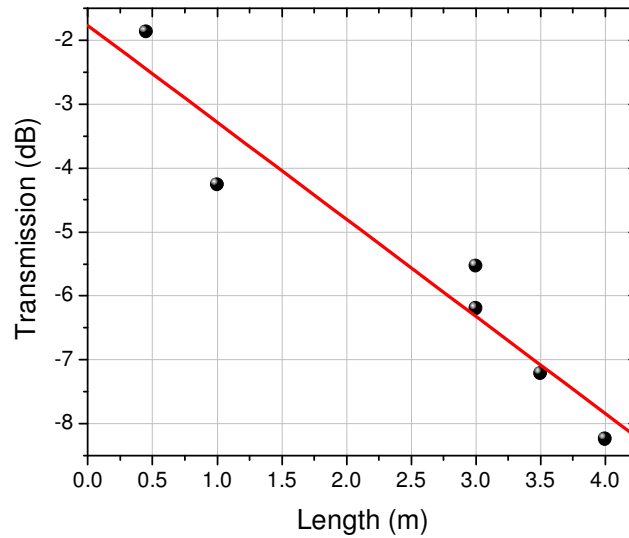


**Figure 4.7: Loss measurements: plot of fiber transmission versus fiber length.**

The fiber bending loss was also studied. Fiber transmission was measured for a fiber with a single-loop ( $360^\circ$  of bending) of different radii. The upstream and downstream segments of the fiber were held approximately straight. The bend loss results are shown in Fig. 4.8 and are determined based on the additional transmission loss caused by bending. A critical bend radius for the PCF was found to be approximately 6 cm.

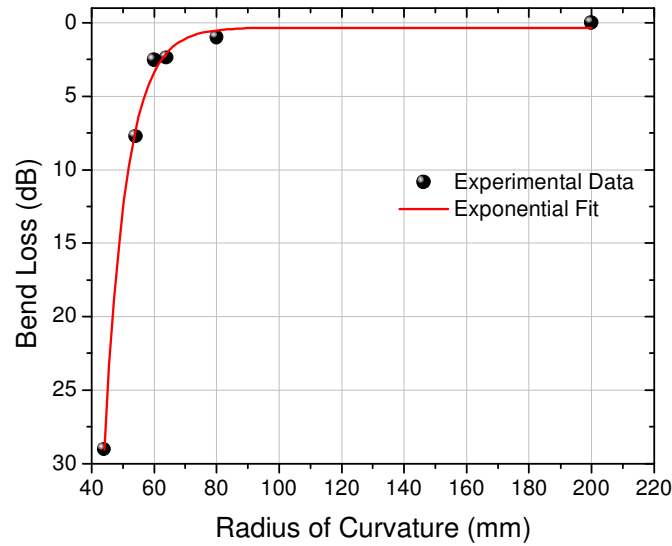


**Figure 4.8: Bend loss measurements: plot of bend loss versus radius of curvature.**

#### 4.3.4. Optical Damage of the PCF

An important issue when operating silica fibers in the UV is the possibility of optically induced damage by UV photons, i.e. effects color centers (absorbing defect centers) or solarization. Past studies involving irradiation of fused-silica (bulk samples and multimode fibers) by krypton fluoride (KrF) lasers at 248 nm found optical damage attributed to  $E'$  centers, i.e. an unpaired electron in a silicon dangling bond (absorption centered at  $\sim 210$  nm), or nonbridging oxygen hole center (NBOHC), i.e. an unpaired electron in an oxygen dangling bond (absorption centered at  $\sim 265$  nm)<sup>[91, 92]</sup>. Our observations are consistent with past excimer laser studies showing reduced UV transmission, but unchanged transmission of 633 nm light. Additionally, as shown in the Fig. 4.9 a weak red fluorescence from the fiber tip was observed resulting from the fiber damage<sup>[92, 93]</sup>. The effect was more clear when the

jacket of the fiber was removed. An extended path of red fluorescence can be seen in the right photograph of Fig. 4.9.

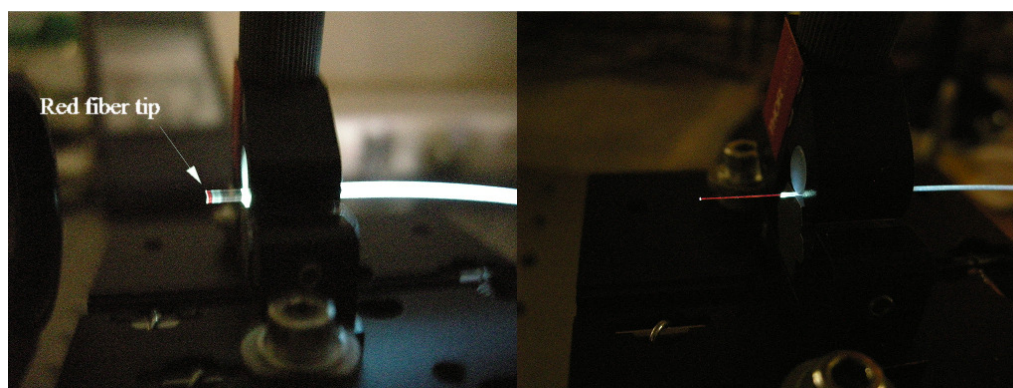


**Figure 4.9: Left: photograph of red light emission near damaged fiber tip with the fiber jacket. Right: photograph of red light emission over length of damaged fiber without the fiber jacket.**

Several studies were performed to characterize the optical damage. Figure 4.10 shows the power dependence of the optical damage. The transmission data are for (previously) unused fibers of length 1.3 m and the plotted transmissions are normalized by the initial transmission (approximately 45%). The short timescale fluctuations of each transmission curve are owing to small drifts in laser power or input alignment (both of which were periodically monitored and corrected). Higher optical power leads to more rapid damage, but the damage is not simply dependent on the overall fluence. Operation with input power of 0.3 mW leads to an initial drop followed by stable operation over more than 40 hours at about 65% of the initial transmission. Similar UV damage characteristics with differing short- and then long- term behaviors (slopes) have been reported in commercial silica fibers<sup>[94]</sup>. One way to extend

the fiber lifetime is to cleave the fiber input; however, the reduction in transmission after successive cleavings (i.e. to about 85% of the original baseline value after the first cleave and about 75% after the second cleave) is indicative of a longer term damage process occurring in the length of the fiber which ultimately leads to end of fiber life. Clearly such optical damage is challenging in long-term applications (e.g. communication links), but the PCFs do allow sufficient operation times for our cw-CRDS BN sensor where typical measurement campaigns to study several thruster operating conditions require approximately one to several hours.

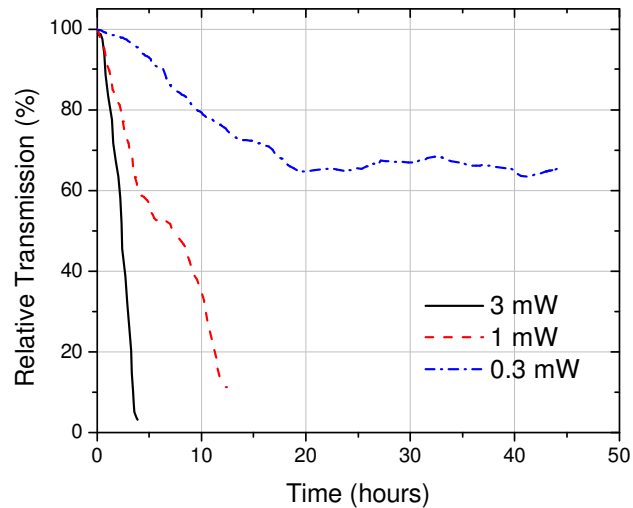


Figure 4.10: Input power dependence of optical damage to the PCF.

#### 4.4. Demonstrative Erosion Measurements and Validation

In order to validate the capability of the BN CW-CRDS erosion sensor, demonstrative measurements were performed by measuring boron atom

number density as sputtered from a BN target. The experimental results were also compared with calculations from a mathematical model.

#### **4.4.1. Number Density Measurements of Sputtered Boron**

An example of boron spectrum measured by the CRDS sensor is shown in Fig. 4.11. The boron spectrum was measured for a 20 s collection time in the diagnostic testbed using an argon ion beam of current 50 mA and energy of 1200 eV for sputtering of the BN target. The absorbance spectrum is plotted in units of parts per million (ppm). To construct the spectrum, a binning approach dividing the frequency axis into a series of 1 GHz-wide bins, was used. Within each bin, the data points were averaged both by frequency and ring-down time. A Voigt profile was fitted to the data points. Path-integrated concentrations were calculated from eqn. 2.9 using the wavelength-integrated area of the spectrum. The true lineshape is not a single Voigt lineshape, but a Voigt lineshape is used as a convenient means to fit the data and determine the area. In some cases, we have also numerically integrated to find area and the consistency of the two methods is within our experimental error.

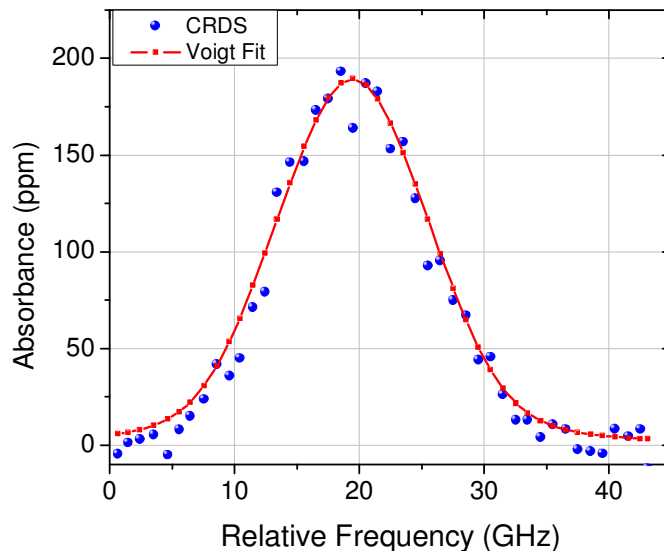


**Figure 4.11: Sample boron absorption spectrum.**

Tests were made to validate our CW-CRDS sensor results. Measurements of boron number density were made as the beam current and voltage were varied. Figure 4.12(a) shows a plot of the dependence of path-integrated boron number density on the ion current. The ion beam voltage was kept at 1200V, while the ion beam current varied from 30 mA to 60 mA. The sputter yield per incident ion does not change with beam current density. Therefore, the path-integrated number density of boron is expected to be proportional to the beam current and the correlation coefficient  $R$  is 99.8% from linear fitting. Similarly, Fig. 4.12(b) shows a plot of dependence of path-integrated boron number density on the ion beam voltage. The sputter yields per incident ion changes almost linearly in this voltage range and again the path-integrated number density shows good linearity with a correlation

coefficient of 99.6%. These results contribute to validation of the basic performance of the CW-CRDS sensor.

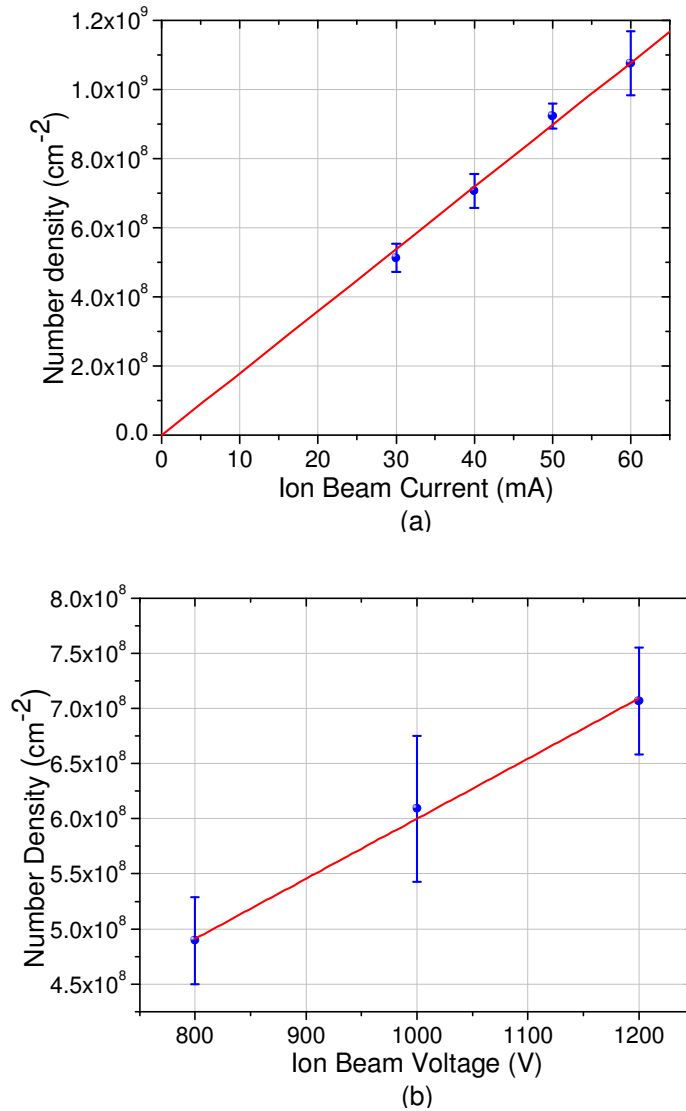


**Figure 4.12: (a): Dependence of path-integrated boron number density on the ion beam current at  $V_b = 1200\text{V}$ , (b): Dependence of path-integrated boron number density on the ion beam voltage at  $I_b = 40\text{mA}$ .**

#### 4.4.2. Preliminary Thruster Testing

A preliminary thruster test of the BN CW-CRDS erosion sensor has also been performed with the same 1 kW class anode layer type Hall thruster described in Chapter 3. A BN channel wall was used in the Hall thruster instead of stainless steel. The system setup was similar to the Mn thruster test. A 5 m long PCF fiber delivered the probe laser light to the optical rail system inside the vacuum chamber. Although no boron spectrum was obtained due to the schedule and the complications during the thruster test, we gained some valuable experience.

In the experiment, the ring-down time began at around 1.2  $\mu\text{s}$  with the thruster off. Vibration from the pump system did little to influence the cavity alignment. Several thermocouples, placed in different spots of the optical rail system, were used to monitor the temperature during Hall thruster operation. The ring-down time dropped as soon as the thruster turned on. The cavity mode match became worse and the signal to noise ratio decreased considerably. The temperature increase of the rail system due to the Hall thruster was about 5  $^{\circ}\text{C}$  with thermal insulation such as metallic and kapton foil, compare this to a temperature change of  $\sim 65$   $^{\circ}\text{C}$  without insulation. The ring down time didn't show a strong correlation with temperature change. When the Hall thruster was turned off, the ring down time slowly recovered to 0.8  $\mu\text{s}$ . A possible explanation for this phenomenon is UV induced damage. Hall thrusters generate considerable UV radiation during operation<sup>[26]</sup>. The intense

UV light can degrade the dielectric coating of the cavity mirrors and cause short ring down times. In future, a proper protection from UV damage is needed.

#### 4.4.3. Sensitivity Analysis

Estimates of minimum detectable optical absorbance can be found from the noise in the cw-CRDS detection system using eqn. 2.10. The standard error represents the expected standard deviation between the measured estimates and the true value, and is computed as the standard deviation divided by the square-root of the number of measurements. The standard deviation of our CW-CRDS system is approximately 1% of the ring-down time  $\tau$ . For a fixed frequency, the minimum detectable absorbance is about 0.6 ppm in 20 s measurement time ( $\sim 1000$  ring-down events). In a typical frequency scan over 50 GHz, there are about 20 ring-down measurements within each 1 GHz bin in 20 s. The resulting minimum detectable absorbance due to the BN absorption line is about 5 ppm for 20 s measurement time.

To assess the expected signal-to-noise ratio (SNR) for thruster studies we consider the expected boron concentration in the thruster plume. Based on scaling of wall erosion rates modeled by Yim *et al.*<sup>[3]</sup>, a path-integrated number density of boron atoms at the thruster exit plane of  $10^9 \text{ cm}^{-2}$  to  $10^{10} \text{ cm}^{-2}$  was predicted. The corresponding peak absorbance of the boron absorption line at 249.848 nm is estimated to be  $\sim 15\text{-}150$  ppm (based on an expected full-width half maximum of 100 GHz). Thus, for expected thruster conditions the SNR of our CRDS boron sensor would be  $\approx 3\text{-}30$  for a 20 s measurement time, and can

be increased with longer measurement durations. It is also interesting that, especially for long measurement times, the detection limit of our CRDS system is sufficiently low, that if the sensor does not yield a measurable signal, then we will have confirmed that the boron concentrations ( $\sim 10^6 \text{ cm}^{-3}$ ) and associated erosion rates ( $\sim 0.1 \text{ }\mu\text{m/hr}$ ) are low enough to correspond to very long thruster lifetimes ( $>9,000$  hours).

#### **4.5. Summary**

Techniques providing *in situ* quantitative measurements of Hall thruster erosion rates are of importance for predicting the lifetime and for optimizing operation conditions and thrusters designs. The CW-CRDS sensor presented in this chapter will contribute to filling the current gap in the ability to rapidly measure BN erosion in Hall thruster. A BN erosion sensor has been developed based on CRDS using a frequency-quadrupled ECDL system in the vicinity of the boron atomic transition ( $\sim 250 \text{ nm}$ ). The optical cavity is housed on a custom rail system with fiber coupling in and out of the vacuum chamber. A PCF was used to deliver single-mode UV laser light into the cavity. The flexibility of such an approach allows implementation in different types of vacuum chamber facilities.

The absorption spectrum of boron atoms sputtered by an ion beam from a BN target sample has been measured as an initial demonstration of the sensor. The dependence of sputtered particle number density on ion beam current and voltage was measured and found to be in accordance with

expectations. The measurements were also validated against finite-element sputter model. The sensor has a minimum detectable absorbance of 0.6 ppm in 20 s measurement time, which should be very adequate for erosion studies of Hall thrusters. The sensitivity is largely limited by the relatively poor reflectivity of the ultraviolet mirrors.

The BN CW-CRDS erosion sensor directly measures the path-integrated number density of particles along the optical axis. However, computation of the corresponding BN erosion rate requires the flux density of the sputtered particles, which depends on both the number density and velocity of sputtered particles. Therefore, the velocity (distribution) of sputtered boron atoms (from BN materials) is a critical parameter for interpretation of measurements from BN CRDS erosion sensors. The experimental measurements for the velocity of sputtered boron atoms are presented in the next chapter for the implementation of the BN CW-CRDS erosion sensor.

## Chapter 5

### LIF Velocity Measurements of Sputtered Boron Atoms

The BN CW-CRDS erosion sensor directly measures the path-integrated number density of particles along the optical axis. However, computation of the corresponding BN erosion rate requires the flux density of the sputtered particles, which depends on both the particle number density and velocity. Therefore, the velocity (distribution) of sputtered boron atoms (from BN materials) is a critical parameter when interpreting measurements from the BN CRDS erosion sensor. While ejection velocities and binding energies are generally known for single-component targets, the situation is more difficult for multi-component targets, and we are unaware of any past measurements for BN. Additionally, velocity spectra of sputtered atoms give direct and detailed insight into the basic sputtering mechanism<sup>[10, 95]</sup>. The velocity (energy) distribution of sputtered boron allows determination of the surface binding energy  $E_B$  and, when combined with angular (differential) sputter yield data, provides a rich description of the BN sputtering process. For these reasons, velocity measurements of sputtered boron from BN targets are needed in Hall thruster research. Laser Induced Fluorescence (LIF) is applied for

measurements of velocity distributions of sputtered boron atoms from ion beam bombardment of a BN target. The LIF technique provides *in situ* non-intrusive velocity resolved measurements.

## 5.1. LIF Velocity Measurement for Sputtered Particles

### 5.1.1. LIF Velocity Measurement Technique

Laser induced fluorescence is a highly sensitive technique that has been widely used to measure particle number densities in plasma. The laser light excites the target species at a selected resonance frequency. Then the excited state, which needs to have a short lifetime, decays and emits fluorescence light, which is measured for number density analysis. LIF has also been used to measure the velocity of target species and provides a non-intrusive diagnostic for velocity distribution measurements of sputtered particles in vacuum conditions<sup>[27-30, 96-98]</sup>.

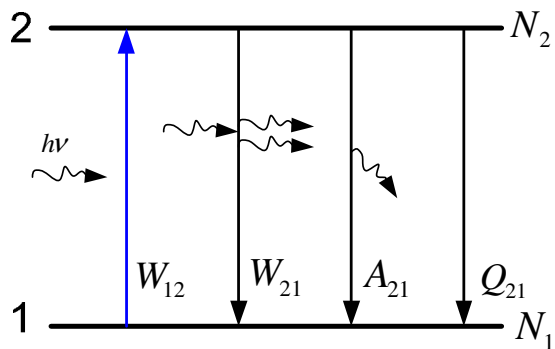


Figure 5.1: Simplified two level LIF model.

A two level LIF mode is considered in Fig. 5.1. with  $N_1$  and  $N_2$  being the population of atoms in the ground state (level 1) and excited state (level 2) respectively. The atoms in the ground state can absorb the incident light of frequency  $\nu$  and be excited to the upper state. In a simplified two-level system, atoms in the excited state, which can be depopulated by stimulated emission ( $W_{21}$ ), spontaneous emission ( $A_{21}$ ), and collisional quenching ( $Q_{21}$ ), have only one decay channel (back to the ground state). In LIF experiments, the intensity of light from spontaneous emission is measured with a photon detector. The total fluorescence power,  $S_f$ , is proportional to the number density of atoms  $N_2$  in the excited state and is given by:

$$S_f = \eta A_{21} h \nu_{21} N_2 = \eta \frac{B_{12}}{B_{12} + B_{21}} \frac{A_{21}}{1 + \frac{I_{sat}}{I_\nu}} h \nu_{21} N_1 \quad (5.1)$$

where  $A_{21}$ ,  $B_{12}$  and  $B_{21}$  as the Einstein A and B coefficients,  $h$  is Planck's constant,  $I_{sat}$  is the saturation spectral irradiance,  $I_\nu$  is the actual spectral irradiance, and  $\eta$  is a factor accounting for detector efficiency factor and geometrical collection. The saturation spectral irradiance  $I_{sat}$  is defined as:

$$I_{sat} = \frac{A_{21} + Q_{21}}{B_{12} + B_{21}} c \quad (5.2)$$

where  $Q_{21}$  is the quenching rate from level 2 to level 1 and  $c$  is the speed of light.

LIF is generally performed in two different regimes: the linear regime or the saturated regime. When the laser irradiance,  $I_\nu$ , is much smaller than the

saturation spectral irradiance,  $I_{sat}$ , the fluorescence is said to be in the linear regime and the fluorescence signal is linearly proportional to the input laser irradiance. In the saturated regime, the laser irradiance,  $I_v$ , is much larger than the saturation spectral irradiance,  $I_{sat}$ . In that case, the fluorescence signal is independent of the laser irradiance and quenching and information associated with the lineshape is lost. However, one needs to capture the velocity information from the lineshape analysis which is related to the Doppler shift. As a result, LIF velocity measurements should be made in the linear regime.

In a LIF velocity measurement, a tunable laser with frequency  $\nu_L$  illuminates the targeted particles (ions, atoms, radicals, molecules). The transition frequency of the particles is  $\nu_0$ , whereas the particles with a velocity component  $u$  away from (and parallel to) the laser beam can only absorb photons if they satisfy the Doppler shift condition. The magnitude of the frequency shift  $\Delta\nu$  is:

$$\Delta\nu = \nu_L - \nu_0 = \frac{u}{c}\nu_0 \quad (5.3)$$

The subsequent fluorescence emission from excited atoms is detected and recorded as a function of the laser frequency. The frequency (wavelength) distribution of the fluorescence intensity is broadened based on the velocity distribution. The dependence of the fluorescence intensity on laser frequency is obtained by scanning the laser frequency near the transition frequency of the absorbing species along the path of the laser. Note that owing to the collisionless environment, neither thermal broadening, pressure broadening,

nor collisional quenching come into play. Thus the velocity distribution can be derived from the fluorescence spectrum.

Figure 5.2 shows the selected boron atomic transition line and the corresponding fluorescence signal. It is very similar to the two level LIF model discussed above, although the ground state for boron atoms has two distinct levels:  $2p^2P_{1/2}$  (at 0 eV) and  $2p^2P_{3/2}$  (at 0.00189 eV). In this work, boron atoms are pumped from the ground state  $2p^2P_{3/2}$  to excited state  $3s^2S_{1/2}$  by a probing laser at  $\lambda_0 = 249.8$  nm. The excited state  $3s^2S_{1/2}$  has a radiative lifetime of 4 ns<sup>[96]</sup>. The wavelength of the fluorescence signal is the same or close to the probing laser wavelength, so called resonant fluorescence. In order to detect such weak LIF emission in the presence of intense background light (from both the pump laser and the plasma), a common method is to modulate the probing laser and employ phase synchronized detection, i.e., by using a lock-in amplifier.

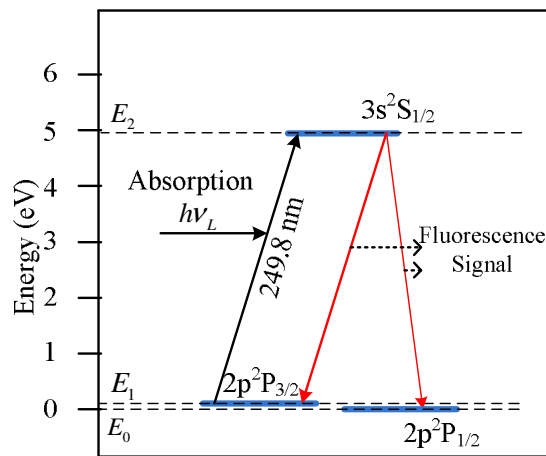


Figure 5.2: Selected boron transitional lines for LIF.

### 5.1.2. Velocity Distribution of Sputtered Particles

The velocity (energy) distributions of particles sputtered from polycrystalline samples subjected to keV ion bombardment have been reasonably well described by the Thompson-Sigmund theory<sup>[10-12]</sup>. The Thompson-Sigmund energy distribution can be obtained from linear cascade theory with an assumption of a planar surface binding energy  $U_b$ . The theoretical treatment of a random collision cascade results in an energy spectrum of the moving atoms in the cascade inside the target scaling with  $1/E^{3-2m}$ <sup>[10]</sup>, where  $m$  is an energy-dependent parameter in the differential cross-section used for a screened Coulomb potential. Based on this fact, the probability of number density based energy spectrum for sputtered particles  $f(E, \theta)$  is shown as:

$$f(E, \theta) = \frac{C \cdot E}{(E + U_b)^{3-2m}} \cos \theta \quad (5.4)$$

where  $E$  is the energy of the ejected particles,  $\theta$  is the exit angle as measured from the surface normal, and  $C$  is a normalizing constant. The surface binding energy  $U_b$  is the energy needed to remove an atom from the surface. It is a very important parameter for understanding the sputtering behavior of a material. The estimated binding energy depends strongly on the cross-section parameter  $m$ <sup>[99]</sup>, for which a variety of choices have been suggested in the literature. The value of  $m$  varies from 0 to 0.3 for low incident ion energies ( $< \sim 1$

keV)<sup>[10, 12]</sup>. The (flux based) velocity distribution of sputtered atoms flux  $f(u, \theta)$  can be also obtained from the relation between velocity and energy:

$$f(u, \theta) = \frac{C \cdot u^3}{(u^2 + v_b^2)^{3 \cdot 2m}} \cos \theta \quad (5.5)$$

where  $v_b$  is the atomic velocity corresponding to  $U_b$ , and  $u$  is the velocity of sputtered atoms. The values of both  $v_b$  and  $m$  can be computed by fitting the measured velocity distribution.

## 5.2. LIF Experiment Apparatus

The tunable laser used to excite sputtered boron atoms is the same ECDL system as was used for the BN CW-CRDS erosion sensor discussed in Chapter 4. A test beam at 1  $\mu\text{m}$  from the ECDL system was used along with a wavemeter to check the frequency (wavelength) of the laser. The laser frequency measurement resolution at 1  $\mu\text{m}$  was 0.1 GHz, which corresponds to a resolution of  $\pm 0.4$  GHz ( $\pm 100$  m/s) for the 250 nm UV beam. The absolute frequency (“zero” of the distribution) was also checked with a hollow cathode lamp (HCL) as will be described below. The UV laser beam was capable of tuning approximately 200 GHz around  $\lambda_0$  by changing both the voltage of the piezo-electric stack in the external cavity and the temperature of the laser diode. In the present experiments, the frequency of laser was manually tuned across the targeted wavelength range.

Figure 5.3 shows a diagram of the experimental set-up for boron LIF measurements.

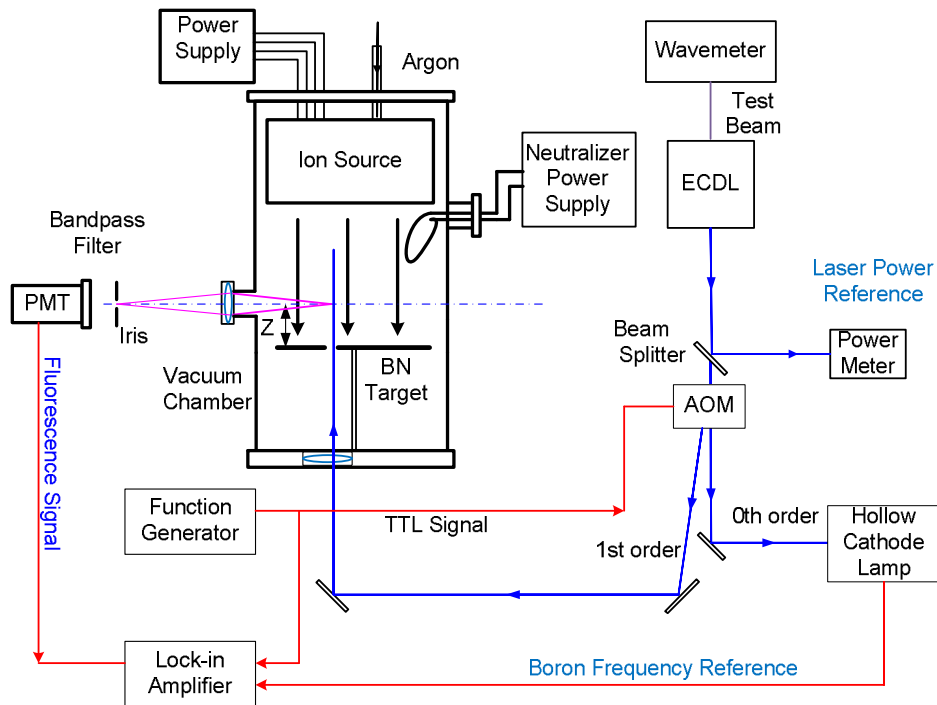


**Figure 5.3: Experimental setup for boron LIF measurements.**

Initial measurements failed to detect the LIF signal against the strong light background so, as will be described below, a modulated beam with lock-in amplifier detection was introduced. At the exit of the ECDL, a beam splitter directed  $\sim 10\%$  of the beam into a power meter to monitor the laser power output. The remainder of the beam was directed to an AOM which was used as a fast optical switch and controlled by a function generator. The zero'th order beam from the AOM was directed to a commercial boron hollow cathode lamp (HCL) for a frequency reference, whereas the first order beam was delivered into the vacuum chamber with a fused silica window and weakly focused in front of the target. The boron HCL spectrum and LIF spectrum were both acquired with the lock-in amplifier, but at different times.

Either high-purity argon (Ar) gas or xenon (Xe) gas was used as the working gas for the ion source. The flow rates were controlled by a thermal mass-flow controller. The ion beam was normally incident to a 14 mm by 14 mm sputter target with a ~6 mm diameter center bore for the beam to pass through, which was held by an adjustable post. The fluorescence light was collected by a 2.53 cm diameter fused silica lens at a position  $Z=55$  mm above the target. The sputtered boron from the BN targets had a slightly under-cosine angular distribution (differential sputter yield profile)<sup>[80]</sup>, with a significant number of particles ejected normal to the target surface. The distance  $Z$  in the experiments was chosen to be much larger than the dimension of the target. As a result, the target can be considered a point source in the model for fitting the experimental data. The point source assumption is quite valid as a result of the small  $\theta$  angle ( $7^\circ$  maximum) from the detection point to the target boundary ( $\cos\theta = 0.99$  between the velocity vector and the illuminated laser direction). The light was imaged onto a photomultiplier tube (PMT, Hamamatsu R3896) with a dielectric interference filter (center wavelength of 250 nm and a transmission bandwidth of 30 nm). The PMT was operated at 1000 V with a 8 k $\Omega$  trans-impedance resistor connected to its output.

When the ion source was on, there was strong background light from both the neutralizer filaments and the ion beam. In addition, BN has a low sputter yield and our laser has relatively low power. This resulted in a fluorescence signal that was much weaker than the background noise (and

undetectable). Therefore, a lock-in detection technique with a chopped laser beam was used to detect the fluorescence signal and improve the signal-to-noise ratio (S:N). A function generator produced a 500 Hz TTL square-wave signal to modulate the AOM, which chopped the laser. The PMT's voltage signal was filtered and amplified by a dual phase lock-in amplifier (EG&G 5210) with a reference TTL signal and a time constant of 10 s or 30 s. The lock-in time constant was selected to be slow enough to achieve high S:N. The use of the lock-in configuration resulted in a final S:N ratio of ~30-150 depending on the ion beam energy and current.

### **5.3. Boron Reference Spectrum from Hollow Cathode Lamp**

The LIF velocity measurements require accurate determination of the frequency shifts shown in eqn. 5.2 including properly locating the zero of the frequency axis (i.e. the frequency corresponding to stationary atoms). In this study, a reference spectrum of boron atoms was obtained using a HCL through the opto-galvanic effect and used to set (or “zero”) the absolute frequency,  $\nu_0$ , and velocity axes.

The opto-galvanic technique can be considered as an alternative to absorption or fluorescence technique<sup>[100]</sup>. Briefly speaking, the opto-galvanic effect is observed as a perturbation in the conductivity of a self-sustained gaseous discharge when the discharge is illuminated by light resonant with the species within. Its mechanism involves laser enhancement or suppression of the ionization rates of a particular species present in the plasma. It gives a

simple and economical way to obtain an atomic or molecular spectrum and can be used in a wide range of applications including spectroscopy, small-concentration detection, isotopic analysis, laser calibration, and laser stabilization<sup>[100]</sup>.

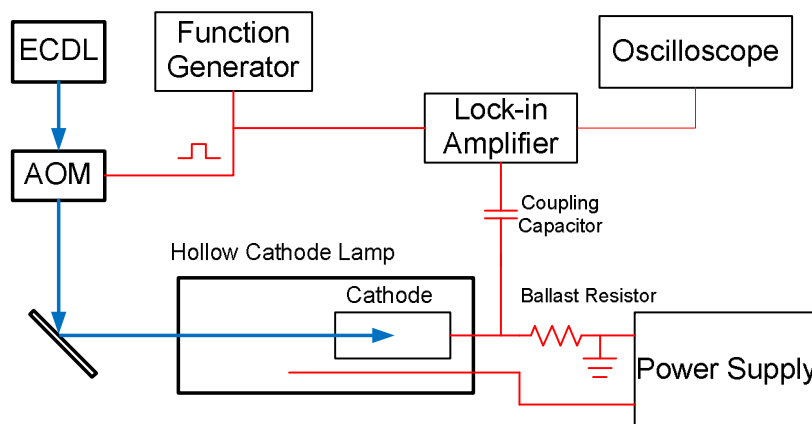


**Figure 5.4: HCL frequency reference.**

Figure 5.4 shows the detailed diagram of the HCL setup for obtaining the reference boron spectrum. A commercial HCL with a boron layer on the hollow cathode provides a glow discharge of boron with an enlargement of the negative glow region. The lamp tube has been filled with 133 Pa of Ne gas. When connected to a DC power supply, a gaseous discharge of Ne occurs within the HCL and produces positive Ne ions, which then bombard the cathode surface and sputter a portion of the cathode material (boron) to the gas phase. The sputtered boron atoms are also ionized by the discharge. Illumination of this HCL with laser radiation at the wavelength corresponding to the boron atomic transition ( $\sim 250$  nm) causes perturbations to the steady-state boron population of the related two levels. This, in turn, causes a change in the

electrical properties of the discharge inside the HCL. By scanning the laser frequency through the resonance frequency of the boron atomic transition, the boron absorption spectrum can be obtained. The pressure and mean free path of boron in the HCL ensure that its spectrum is centered at the zero velocity position. During the experiment, about 5 mW of laser power from the AOM was directed into the negative glow region of the HCL through a fused silica window. The HCL was operated at ~6 mA of discharge current. A 0.47 mF capacitor was used to couple the signal and isolate the high voltage. Opto-galvanic signals were detected across a ballast resistor of 30 k $\Omega$ . The lock-in amplifier filtered and amplified the signal. The beam (AOM) and lock-in amplifier were modulated with a TTL frequency reference signal from a function generator. A digital oscilloscope was used to record the signal. The modulation and lock-in parameters were similar to those used in the LIF experiments. During the measurement, the laser was manually scanned across the resonance frequency and adjusted to maintain the same laser power with the help of a power meter. One measured opto-galvanic spectrum of boron atoms from HCL is shown in Fig. 5.5. The center frequency of this spectrum corresponds to the zero velocity position in the frequency axis of sputtered boron atoms velocity distribution. This position was recorded with the wavemeter as a reference for velocity distribution measurements. The center was located within  $\pm 0.01$  GHz uncertainty (approximately 40 times better precision than is possible with our wavemeter for the UV beam).

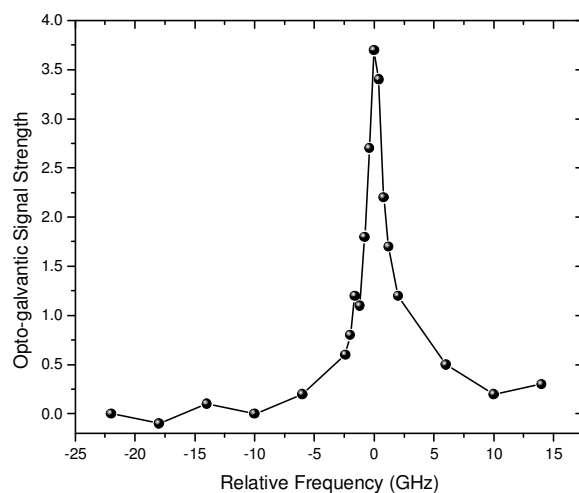


**Figure 5.5: Boron opto-galvanic spectrum from boron hollow cathode lamp.**

## 5.4. Results and Analysis of LIF Measurements

### 5.4.1. Demonstrative Measurement

Prior to measurements with a BN target, velocity profiles were performed for a pure boron target (~99.9% purity) to validate the experiment setup and method. Figure 5.6 shows the LIF spectrum from pure boron sputtered by an argon ion beam (1200 V, 30 mA) as well as the wavelength reference signal of the boron opto-galvanic HCL spectrum. A Sigmund-Thompson profile, which best fits the experimental LIF curve, gives  $m = 0 \pm 0.02$  and  $v_b = 10,000 \pm 300$  m/s ( $E_b = 5.7 \pm 0.3$  eV). The error bars are based on 95% confidence bounds from fitting. The measured  $E_b$  agrees with the sublimation energy of boron ( $E_b = 5.73$  eV) from the computer code *Srim and Trim*<sup>[101]</sup> and the experimental result of Ito et al. (6 eV)<sup>[97]</sup>.

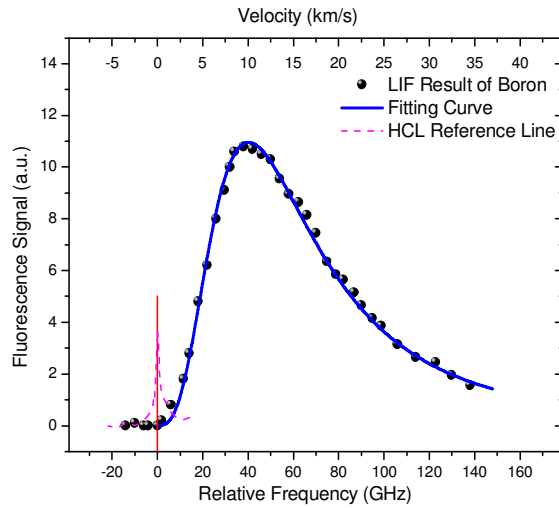


**Figure 5.6: Boron LIF spectrum and fit for Ar ions at 1200 eV.**

As discussed above, the LIF velocity measurement should be performed in the linear regime, where the fluorescence signal is linearly proportional to the induced laser power. The input laser power of 250 nm was about 10 mW. The laser beam was focused to a beam diameter of 0.6 cm in front of the target. In a rough calculation, this gave the laser irradiance to be  $35.3 \text{ W/cm}^2$ . Based on eqn. 5.2 and a zero quenching condition, the saturated laser irradiance was calculated to be  $0.64 \text{ GW/cm}^2$  at the transitional peak. Therefore, we expect to be well within the linear regime, which is also consistent with other references<sup>[27, 28]</sup>. An experimental validation of the linearity of the fluorescence signal strength has been performed by varying the illuminated laser power manually with an ion beam of 600 eV and 30 mA as shown in Fig. 5.7. The experimental result of LIF signal was linearly proportional to the laser power with a linear correlation coefficient of 0.996. Thus it confirmed the LIF was performed in the linear regime.

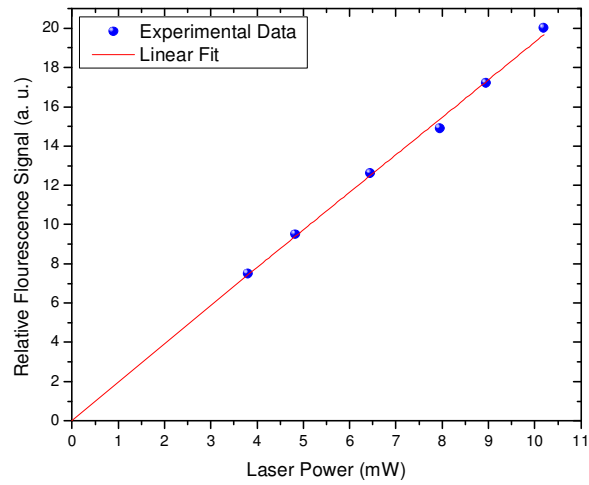


**Figure 5.7: LIF signal intensity versus illuminated laser power.**

#### **5.4.2. BN LIF Spectrum**

The LIF spectra of sputtered boron from a BN target (grade HBR, obtained from GE Advanced Materials) have been measured with both Ar and Xe ions. Three tests were first done with an Ar ion beam at energies of 300, 800, and 1200 eV, all at 30 mA. Figure 5.8 shows the three LIF spectra along with the corresponding fitted profiles.

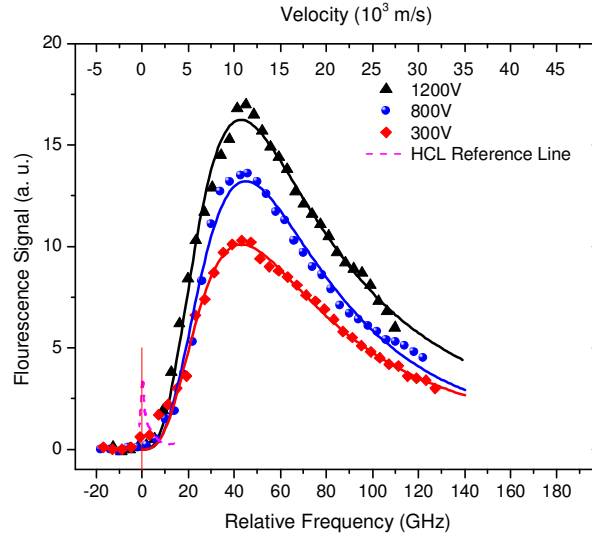


**Figure 5.8: BN LIF spectra and fits at different Ar ion energies.**

Table 5.1 shows the fitted values of  $m$ ,  $v_b$ , and corresponding  $E_b$ . All values of  $m$  are close to 0.2 and in the expected range of 0-0.3 for low energy ions. It is noteworthy that small changes in the  $m$  value have a large effect on the fit value of  $v_b$ . To illustrate this, Figure 5.9 shows best fit profiles for the BN experimental data for 800 eV Ar ion beam for different cases where  $m$  is fixed and  $v_b$  treated as the sole fit parameter. The best-fit values of  $v_b$  change from 11,300 m/s ( $E_b=7.2$  eV) to 8,200 m/s ( $E_b= 3.9$  eV) as  $m$  varies from 0 to 0.3.

**Table 5.1: Fitting results for LIF measurements with Ar ion beam.**

Ar Ion beam condition	$m$	$v_b$ (m/s)	$E_b$ (eV)
300 V	$0.20 \pm 0.04$	$9,200 \pm 300$	$4.8 \pm 0.3$
800 V	$0.19 \pm 0.02$	$9,200 \pm 400$	$4.8 \pm 0.4$
1200 V	$0.22 \pm 0.05$	$9,100 \pm 400$	$4.7 \pm 0.4$

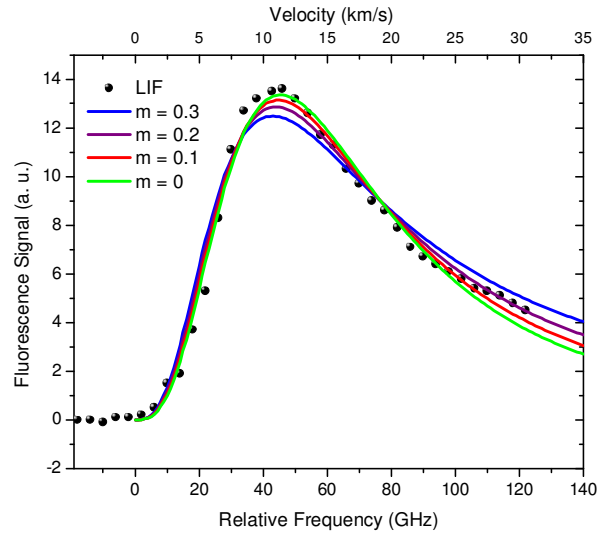


**Figure 5.9: Best fit profiles for several values of  $m$  for Ar ions at 800 eV.**

In Hall thrusters, the ions (Xe) that erode the BN wall material have typical average energy of  $\sim 70$  eV<sup>[95]</sup>, which may depend on the discharge voltage (normally 100 to 500 V). Figure 5.10 shows an experimental measurement of Xe ion energy involved in erosion in a Hall thruster with different discharge voltages<sup>[82]</sup>.

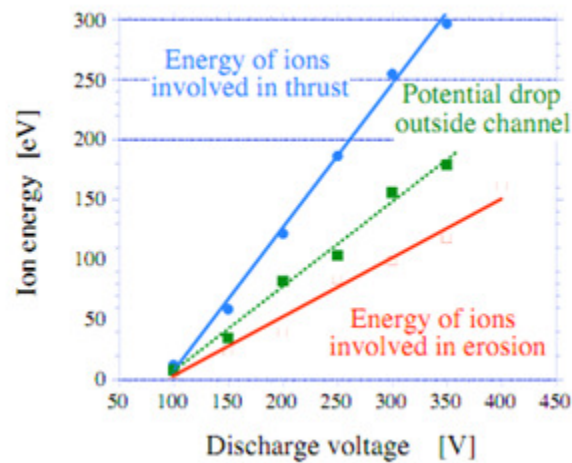


**Figure 5.10: Energy of Xe ions involved in thruster and in erosion versus discharge voltage<sup>[95]</sup>.**

Therefore, the sputtered boron velocity distribution from low energy Xe ion is of most interest for Hall thrusters. All the results shown above were done with Ar ion beam at relatively high energy. The simplest theoretical expectation is that the binding energy is material (target) dependent and thus does not (strongly) depend on the ion energy, species, or incidence angle<sup>[10]</sup>. In order to validate this idea, several tests were performed with a Xe ion beam at 100, 200, 300, and 1200 V. The lowest ion energy we have measured at (owing to the stability and beam quality of the ion source used) is 100 eV. In Fig. 5.11, the velocity distributions from the Ar ion beam test and the Xe ion beam test at 1200 V are drawn together after scaling to show the similarity.

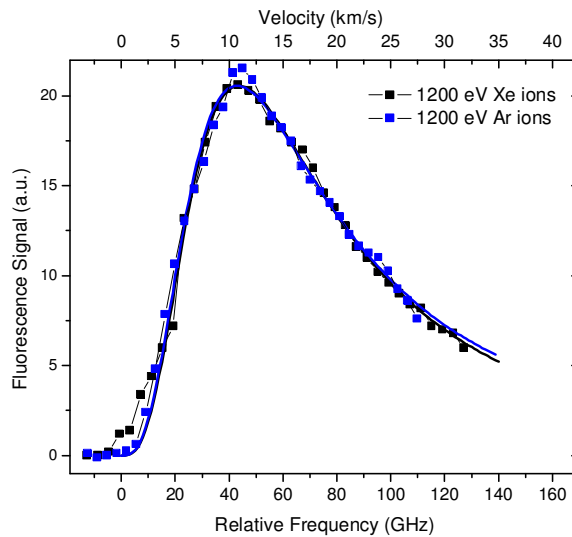


**Figure 5.11: BN LIF spectra and fits for Xe and Ar ions at 1200 eV.**

Figure 5.12 shows the fitting curves for one series of experimental results from the low energy Xe LIF experiments. In addition to the normal incident angle, two initial measurements were done with the target placed at

45° and 60° incident angle. Table 5.2 shows all the fitting results for Xe LIF experiments with  $m$  and  $V_b$  both as free parameters. The error bars were calculated based on 95% confidence bounds from fitting.

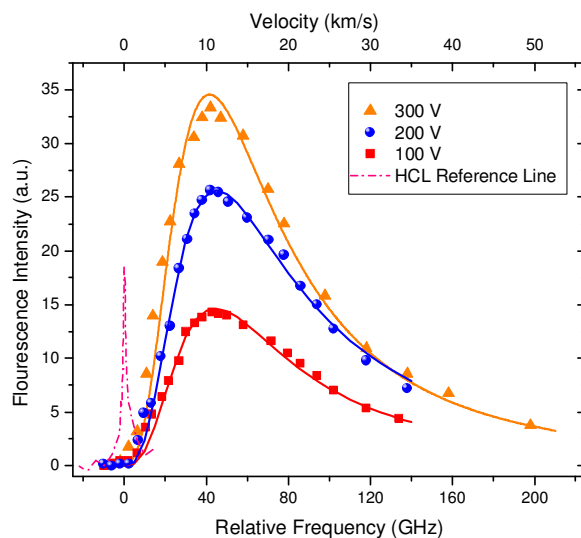


**Figure 5.12: BN LIF spectra and fits at different Xe ion energies.**

**Table 5.2: Fitting results for LIF measurements with Xe ion beam.**

Xe Ion beam condition		$m$	$v_b$ (m/s)	$E_b$ (eV)
100V	Test1	$0.23 \pm 0.04$	$9,000 \pm 500$	$4.5 \pm 0.6$
	Test2	$0.21 \pm 0.02$	$9,500 \pm 500$	$5.0 \pm 0.6$
200V	Test1	$0.24 \pm 0.02$	$9,200 \pm 300$	$4.8 \pm 0.3$
	Test2	$0.22 \pm 0.02$	$9,200 \pm 350$	$4.8 \pm 0.4$
300V	Test1	$0.20 \pm 0.03$	$9,100 \pm 350$	$4.6 \pm 0.4$
	Test2	$0.23 \pm 0.02$	$9,100 \pm 350$	$4.6 \pm 0.4$
1200V	Test1	$0.17 \pm 0.05$	$9,500 \pm 500$	$5.0 \pm 0.6$
300V	45° incidence	$0.21 \pm 0.03$	$8,700 \pm 500$	$4.3 \pm 0.4$
	60° incidence	$0.19 \pm 0.04$	$8,800 \pm 400$	$4.3 \pm 0.4$

Indeed, the measured binding energies due to Ar ions at different energies, as well as the Xe ion measurements, all appear self-consistent and

give a surface binding energy of boron (from BN target) of  $E_b=4.8\pm 0.2$  eV (based on averaging the measured data). Some past research, with other species and target materials, has shown weak dependences of the ejected velocity profiles on ion energy and incidence angle<sup>[10, 29-31, 102]</sup>, but the variations are relatively small compared to our experimental uncertainty and the accuracy needed for engineering analyses.

## 5.5. Summary

In this chapter, LIF measurements for determining the velocities of sputtered boron atoms from BN targets were presented. The illumination source was a frequency-quadrupled continuous-wave ECDL system in the vicinity of 250 nm. Opto-galvanic spectroscopy has been applied to obtain the boron thermal absorption spectrum which acts as a frequency reference for the LIF spectra. The weak fluorescence signals from excited boron atoms have been detected with a lock-in amplifier scheme. Boron LIF spectra due to argon ions incident on a pure boron target, as well as due to argon and xenon ions incident on a BN target, have been measured and fitted with Sigmund-Thompson distributions. The measured surface binding energy of pure boron was  $E_b=5.7\pm 0.3$  eV, which agrees with previous measurement results. The surface binding energy of boron from BN has been studied with both Ar and Xe ions at different energies and incidence angles yielding an averaged surface binding energy of  $E_b=4.8\pm 0.2$  eV. The binding energy (along with  $m$  parameter) provides a convenient means to characterize the overall velocity (energy)

profile. Binding energies generally depend on the target material but not (strongly) on the ion species, energy, or incidence angle, so that the value reported above should be reasonably applicable to ion sputtering conditions of the BN channel in Hall thrusters, in particular for linking number density (measured by the CRDS sensor) to fluxes of sputtered particles.

## **Chapter 6**

### **Conclusion and Future Work**

#### **6.1. Conclusion**

The finite lifetime of Hall thrusters, and lack of lifetime diagnostics limits future application of this promising EP device. The erosion of the BN acceleration channel wall is the major limiting factor of the lifetime of Hall thrusters. CRDS has been demonstrated as an ultra-sensitive diagnostic tool for quantitative studies of sputter erosion processes. Owing to its better sensitivity and compact configuration, CW-CRDS can provide a powerful non-intrusive erosion sensor that will strongly complement available techniques for measuring the lifetime of Hall thrusters and optimizing their operating conditions. This dissertation described two CW-CRDS erosion sensors.

The first CW-CRDS erosion sensor uses an ECDL in the vicinity of 403 nm as the light source to probe sputtered Mn atoms. The ring down signal is triggered by a custom threshold detection circuit, which monitors the signal strength of the PMT and generates a trigger pulse to switch off the laser with AOM. The ring down signal is digitalized via an AD acquisition board and processed in a custom Labview program. Demonstrative experiments for the

Mn erosion sensor were performed in a testbed, where a Mn/Fe target was bombarded by an ion beam in a vacuum chamber. Measurement of the Mn hyperfine spectrum and Mn atom number density dependences studies have been presented to validate the sensor. A potential industrial application is to use this sensor for real-time end-point detection when sputtering multi-layer targets as presented in the dissertation. Finally, the Mn CW-CRDS erosion sensor along with a custom optical rail system was employed to measure the erosion from an anode layer Hall thruster with a stainless steel channel wall in a large vacuum facility. The test results are very encouraging and demonstrate the capability of *in situ* erosion measurement for Hall thrusters. The performance of the Mn erosion sensor shows sufficient time response and spectral resolution for the targeted applications

The ultimate goal of the present research is to enable sensors for real time *in situ* detection of the erosion of BN, which is the primary channel material used in Hall thrusters. Therefore, a BN CW-CRDS erosion sensor has been developed based on the experience of the Mn erosion sensor. A more complicated laser (frequency-quadrupled ECDL) system was used to probe sputtered boron atoms from BN erosion at the wavelength of ~250 nm. Fiber delivery of single-mode UV laser light has been achieved with a photonic crystal fiber for flexible implementation in different vacuum chambers. Demonstrative boron spectra were obtained in our testbed sputtering apparatus. A minimum detectable absorbance of 0.6 ppm boron atoms in 20 s

measurement time, which is adequate for erosion studies of Hall thrusters, was achieved.

One also needs the velocity profiles of the sputtered boron atoms in order to calculate the flux (and erosion rate) from the measured path-integrated particle number density. Chapter 5 presented the LIF measurements for the velocity distribution of sputtered boron atoms at different ion energies. A lock-in amplifier was used to extract the fluorescence signal from the larger background. Opto-galvanic spectroscopy was used to provide a frequency reference. The measured binding energy of  $4.8 \pm 0.2$  eV provides a convenient means to characterize the overall velocity (energy) profile of sputtered boron atoms from BN.

## **6.2. Future Work**

### **6.2.1. Improvements to BN Erosion Sensor**

The initial demonstration of the BN CW-CRDS erosion sensor was largely successful; however, steps can be taken to improve the sensor in terms of sensitivity, stability and long term operation. One can attach a PZT to a cavity mirror, so that the length of the optical cavity can be modulated. In this way, one can increase the frequency of ring down signal generation (single ingestion rate), which helps to increase the SNR in the same collection time. The PCF used for laser delivery at 250 nm has a limited working duration due to UV damage to the fiber material. A possible improvement is to use a step-index UV enhanced

multimode fiber to deliver the laser, which can higher damage threshold (longer operating time) and is inexpensive.

The major limiting factor for the sensitivity of the existing BN erosion sensor is the reflectivity of the dielectric mirrors. Dielectric mirrors in the 249 nm region have maximum reflectivity of about 0.998, corresponding to 2000 ppm loss from a single mirror. In addition, the reflectivity of dielectric mirrors drops when being exposed in intense UV radiation. An alternative approach to using dielectric mirrors in CRDS involves the use of an optical cavity based upon a pair of Brewster Angle prisms as retro-reflectors. As shown in Fig. 6.1, retro-reflection is achieved when light enters a prism at or very near Brewster's angle (where there is very low loss for p-polarized light), undergoes two total internal reflections and leaves parallel to the input beam<sup>[103]</sup>. Calcium fluoride ( $\text{CaF}_2$ ) is particularly promising UV material owing to low scattering loss and absorption in the UV<sup>[104]</sup>. A predicted loss of around ~500 ppm from the prism cavity could be obtained at 249 nm, nearly one order of magnitude lower than the total cavity loss caused by dielectric mirrors. The use of such a prism cavity would provide significant sensitivity improvement.



**Figure 6.1: Schematic of Brewster prism cavity.**

### 6.2.2. Hall Thruster Testing

The Hall thruster test with the BN CW-CRDS erosion sensor is a desired next step. We have attempted on a preliminary test of BN erosion sensor as presented in Chapter 4. Tests have also been started in the Plasmadynamics and Electric Propulsion Laboratory (PEPL) at the University of Michigan, which collaborates with our group. Sputter erosion measurements from the BN acceleration channel wall in Hall thrusters are much more complicated than the validation experiments done with an ion source due to the geometrical complexity and the broad energy and angular distribution of collided ions. In addition, the environment around a working Hall thruster is filled with dense plasma, radiation and vibration. As a consequence, the performance of the BN sensor will be significantly challenged.

The path-integrated boron atom number density measured by CW-CRDS erosion sensor should be roughly proportional to the actual erosion rate of the BN channel wall. In the Hall thruster tests, the erosion sensor will be moved on a translation stage in order to probe different chords . A radial distribution of the sputtered boron atoms in the exit of the Hall thruster can be computed via spatial inversion (Abel inversion). The BN erosion sensor can also be used to study the dependence of erosion on Hall thruster operating conditions. The erosion sensor will be linked with numerical modeling ( of the full thruster, including erosion) as a means to determine erosion rate and lifetime. Validation against traditional methods, such as weight loss and

profilometry , will also be performed. Ultimately, the combination of the erosion sensor and modeling will allow understanding of the erosion physics of Hall thrusters devices.

## Bibliography

- [1] C. E. Garner, *et al.*, "A 5730-Hr Cyclic Endurance Test of the SPT-100," IEPC-95-179, in *the 24th IEPC*, Moscow, 1995.
- [2] D. M. Goebel and I. Katz, *Fundamentals of Electric Propulsion: Ion and Hall Thrusters*: Wiley, 2008.
- [3] J. T. Yim, "Computational Modeling of Hall Thruster Channel Wall Erosion," Doctor of Philosophy, Aerospace Engineering, University of Michigan, Ann Arbor, 2008.
- [4] M. Tajmar, *Advanced Space Propulsion Systems*. New York: Springer, 2003.
- [5] R. G. Jahn and E. Y. Choueiri, "Electric Propulsion," in *Encyclopedia of Physical Science and Technology*. vol. 5, R. A. Meyers, Ed., Thrid Edition ed: Academic Press, 2002, pp. 125-141.
- [6] H. Kuninaka, *et al.*, "Asteroid Rendezvous of HAYABUSA Explorer Using Microwave Discharge Ion Engines," IEPC-2005-10, in *29th International Electric Propulsion Conference*, Princeton Univerisity, 2005.
- [7] V. Kim, *et al.*, "History of the Hall Thrusters Development in USSR," IEPC-2007-142, in *the 30th International Electric Propulsion Conference*, Florence, Italy, 2007.
- [8] E. Y. Choueiri, "Fundamental Difference Between the Two Hall Thruster Variants," *Physics of Plasmas*, vol. 8, pp. 5025-5033, 2001.
- [9] V. V. Zhurin, *et al.*, "Physics of Closed Drift Thrusters," *Plasma Sources Science and Technology*, vol. 8, pp. R1-R20, 1999.
- [10] G. Betz and K. Wien, "Energy and Angular-Distributions of Sputtered Particles," *International Journal of Mass Spectrometry and Ion Processes*, vol. 140, pp. 1-110, 1994.
- [11] R. Behrisch, *Sputtering by Particle Bombardment I: Physical Sputtering of Single-Element Solids*. vol. 47. New York: Springer-Verlag, 1981.
- [12] P. Sigmund and Kongelige Danske videnskabernes selskab., *Fundamental processes in sputtering of atoms and molecules (SPUT92) : symposium on the occasion of the 250th anniversary of the Royal Danish Academy of Sciences and Letters, Copenhagen, 30 August - 4 September, 1992 : invited reviews*. Copenhagen: Kongelige Danske videnskabernes selskab, 1993.
- [13] J. R. Anderson, *et al.*, "Results of an On-going Long Duration Ground Test of the DS-1 Flight Space Engine," AIAA 99-2857, in *the 35th Joint Propulsion Conference*, Los Angeles, CA, 1999.

- [14] C. E. Garner, *et al.*, "Performance Evaluation and Life Testing of the SPT-100," AIAA-94-2856, in *the 30th Joint Propulsion Conference*, Indianapolis, IN, 1994.
- [15] V. Kim, "Main Physical Features and Processes Determining the Performance of Stationary Plasma Thrusters," *Journal of Propulsion and Power*, vol. 14, pp. 736-743, 1998.
- [16] D. Yu, *et al.*, "Ion Sputtering Erosion of Channel Wall Corners in Hall Thrusters," *Journal of Physics D: Applied Physics*, vol. 39, pp. 2205-2211, 2006.
- [17] V. V. Abashkin, *et al.*, "Analysis of Ceramic Erosion Characteristic in Hall-Effect Thruster with Higher Specific Impulse," IEPC-2007-133, in *the 30th International Electric Propulsion Conference*, Florence Italy, 2007.
- [18] H. Tsuge and S. Esho, "Angular Distribution of Sputtered Atoms from Polycrystalline Metal Targets," *Journal of Applied Physics*, vol. 52, pp. 4391-4395, 1981.
- [19] J. L. Topper, *et al.*, "Preliminary Results of Low Energy Sputter Yields of Boron Nitride due to Xenon Ion Bombardment," AIAA-2008-5092, in *the 44th AIAA Joint Propulsion Conference*, 2008.
- [20] R. D. Kolasinski, *et al.*, "Carbon Sputtering Yield Measurements at Grazing Incidence," AIAA-2006-4337, in *the 42nd Joint Propulsion Conference*, Sacramento, CA, 2006.
- [21] S. Kundu, *et al.*, "The Angular Distribution of Sputtered Silver Atoms," *Nuclear Instruments and Methods in Physics Research B*, vol. 12, pp. 352-357, 1985.
- [22] A. Wucher and W. Reuter, "Angular Distribution of Particles Sputtered From Metals And Alloys," *Journal of Vacuum Science & Technology A: Vacuum, Surfaces, and Films*, vol. 6, pp. 2316-2318, 1988.
- [23] V. Shutthananda, *et al.*, "On the Measurement of Low-energy Sputtering Yield Using Rutherford Backscattering Spectrometry," IEPC-97-069, in *the 25th International Electric Propulsion Conference*, Cleveland, OH, 1997.
- [24] R. P. Doerner, *et al.*, "Sputtering Yield Measurements During Low Energy Xenon Plasma Bombardment," *Journal of Applied Physics*, vol. 93, pp. 5816-5823, 2003.
- [25] N. Anderson, *et al.*, "Atomic Excitations in Sputtering Processes," *Radiation Effects and Defects in Solids*, vol. 60, pp. 119-127, 1982.
- [26] M. Celik, *et al.*, "Use of Emission Spectroscopy for Real-time Assessment of Relative Wall Erosion Rate of BHT-200 Hall Thruster for Various Regimes of Operation," *Vacuum*, vol. 84, pp. 1085-1091, 2010.
- [27] E. Pasch, *et al.*, "Sputtering of Amorphous C-H and C/B-H Layers by Argon Ions," *Journal of Nuclear Materials*, vol. 196, pp. 1065-1068, Dec 1992.
- [28] M. Rowekamp, *et al.*, "Diagnostics of Sputtering Processes of Carbon and Carbides by Laser-Induced Fluorescence Spectroscopy in the VUV at

- 166-nm," *Applied Physics a-Materials Science & Processing*, vol. 54, pp. 61-67, Jan 1992.
- [29] H. L. Bay, "Laser-Induced Fluorescence as a Techniques for Inverstigations of Sputtering Phenomena," *Nuclear Instruments & Methods in Physics Research Section B-Beam Interactions with Materials and Atoms*, vol. 18, pp. 430-445, Feb 1987.
- [30] C. E. Young, *et al.*, "Velocity and electronic State Distributions of Sputtered Fe Atoms by Laser-Induced Fluorsecence Spectroscopy," *Journal of Vacuum Science & Technology a-Vacuum Surfaces and Films*, vol. 2, pp. 693-697, 1984.
- [31] M. J. Pellin, *et al.*, "Laser Fluoresecence Spectroscopy of Sputtered Zirconium Atoms," *Journal of Chemical Physics*, vol. 74, pp. 6448-6457, 1981.
- [32] N. Yamamoto, *et al.*, "Measurement of erosion rate by absorption spectroscopy in a Hall thruster," *Review of Scientific Instruments*, vol. 76, 2005.
- [33] M. P. Arroyo, *et al.*, "Diode-laser Absorption Technique for Simultaneous Measurements of Multiple Gasdynamic Parameters in High-speed Flows Containing Water Vapor," *Applied Optics*, vol. 33, pp. 3296-3307, 1994.
- [34] D. Pagnon, *et al.*, "Control of the Ceramic Erosion by Optical Emission Spectroscopy: Parmametric Studies of PPS1350-G and SPT 100-ML," in *40th Joint Propulsion Conference*, Fort Lauderdale, FL, 2004.
- [35] D. Manzella, *et al.*, "predicting Hall thruster operational lifetime," AIAA-2004-3953, in *the 40th Joint Propulsion Conference*, Fort Lauderdale, FL, 2004.
- [36] J. P. Boeuf and L. Garrigues, "Low Frequency Oscillations in a Stationary Plasma Thruster," *Journal of Applied Physics*, vol. 84, pp. 3541-3554, 1998.
- [37] M. Hirakawa and Y. Arakawa, "Numerical Simulation of Plasmas Particle Behavior in a Hall Thruster," presented at the 32nd Joint Propulsion Conference, Lake Buena Vista, California, 1996.
- [38] J. M. Fife, *et al.*, "A Numerical Study of Low-Frequency Discharge Oscillations in Hall Thrusters," AIAA-97-3052, in *the 33rd Joint Propulsion Conference*, Seattle, Washington, 1997.
- [39] J. T. Yim, *et al.*, "Modeling Low Energy Sputtering of Hexagonal Boron Nitride by Xenon Ions," *Journal of Applied Physics*, vol. 104, pp. 123507-13507-6, 2008.
- [40] W. E. Eagle, *et al.*, "The Erosion Prediction Impact on Current Hall Thruster Model Development," in *AIAA-2008-5087, 44th Joint Propulsion Conference & Exhibit*, Hartford, CT, 2008.
- [41] K. W. Busch and M. A. Busch, *Cavity-ringdown Spectroscopy : an Ultratrace-Absorption Measurement Technique*. Oxford University Press , Washington, DC 1999.

- [42] B. A. Paldus and A. A. Kachanov, "An Historical Overview of Cavity-enhanced Methods," *Canadian Journal of Physics*, vol. 83, pp. 975-999, 2005.
- [43] C. Vallance, "Innovations In Cavity Ringdown Spectroscopy," *New Journal of Chemistry*, vol. 29, pp. 867-874, 2005.
- [44] G. Berden, *et al.*, "Cavity Ring-down Spectroscopy: Experimental Schemes and Applications," *International Reviews in Physical Chemistry*, vol. 19, pp. 565-607, 2000.
- [45] J. M. Herbelin, *et al.*, "Sensitive Measurement of Photon Lifetime and True Reflectances in an Optical Cavity by a Phase-Shift Method," *Applied Optics*, vol. 19, pp. 144-147, 1980.
- [46] D. Z. Anderson, *et al.*, "Mirror Reflectometer Based on Optical Cavity Decay time," *Applied Optics*, vol. 23, pp. 1238-1245, 1984.
- [47] A. O'Keefe and D. A. G. Deacon, "Cavity Ring-Down Optical Spectrometer for Absorption Measurements Using Pulsed Laser Sources," *Review Scientific Instruments*, vol. 59, pp. 2544-2551, 1988.
- [48] R. Engeln and G. Meijer, "A Fourier Transform Cavity Ring Down Spectrometer," *Review of Scientific Instruments*, vol. 67, pp. 2708-2713, 1996.
- [49] R. Engeln, *et al.*, "Polarization Dependent Cavity Ring Down Spectroscopy," *Journal of Chemical Physics*, vol. 107, pp. 4458-4467, 1997.
- [50] Y. Le Grand and A. Le Floch, "Measurement of Residual Reflectivities Using the Two Eigenstates of a Passive Cavity," *Applied Optics*, vol. 27, pp. 4925-4930, 1988.
- [51] Y. Le Grand, *et al.*, "Sensitive Diffraction-Loss Measurements of Transverse Modes of Optical Cavities by the Decay-Time Method," *Journal of the Optical Society of America B: Optical Physics*, vol. 7, pp. 1251-1253, 1990.
- [52] D. Romanini, *et al.*, "CW Cavity Ring Down Spectroscopy," *Chemical Physics Letters*, vol. 264, pp. 316-322, 1997.
- [53] A. P. Yalin, *et al.*, "Application of Cavity Ring-Down Spectroscopy to Sputter Erosion Measurements," in *Laser Applications to Chemical and Environmental Analysis*, *Optical Society of America*, Annapolis, MD, 2004.
- [54] V. Surla, *et al.*, "Sputter Erosion Measurements of Titanium and Molybdenum by Cavity Ring-Down Spectroscopy," *Review of Scientific Instruments*, vol. 75, pp. 3025-3030, 2004.
- [55] A. P. Yalin, *et al.*, "Detection of Sputtered Metals Using Cavity Ring-Down Spectroscopy," *Applied Optics*, vol. 44, pp. 6496-6505, 2005.
- [56] A. P. Yalin, *et al.*, "Sputtering Studies of Multi-Component Materials by Weight Loss and Cavity Ring-Down Spectroscopy," AIAA-2006-4338, in *the 42nd AIAA Joint Propulsion Conference*, Sacramento, CA, 2006.
- [57] A. P. Yalin and V. Surla, "Velocity Measurements by Cavity Ring-Down Spectroscopy," *Optics Letters*, vol. 30, pp. 3219-3221, 2005.

- [58] V. K. Surla and Colorado State University. Dept. of Mechanical Engineering., "Cavity ring down spectroscopy : a Method to Measure Sputter Erosion for EP Applications," Thesis (Ph D ), Colorado State University, 2007., 2007.
- [59] V. Surla and A. P. Yalin, "Differential Sputter Yield Measurements Using Cavity Ringdown Spectroscopy," *Applied Optics*, vol. 46, pp. 3987-3994, Jul 2007.
- [60] H. Kogelnik and T. Li, "Laser Beams and Resonators," *Applied Optics*, vol. 5, pp. 1550-1567, 1966.
- [61] P. Zalicki and R. N. Zare, "Cavity Ring-Down Spectroscopy for Quantitative Absorption Measurements," *Journal of Chemical Physics*, vol. 102, pp. 2708-2717, 1995.
- [62] G. Meijer, *et al.*, "Coherent Cavity Ring Down Spectroscopy," *Chemical Physics Letters*, vol. 217, pp. 112-116, 1994.
- [63] J. T. Hodges, *et al.*, "Laser Bandwidth Effects in Quantitative Cavity Ring-Down Spectroscopy," *Applied Optics*, vol. 35, pp. 4112-4116, 1996.
- [64] H. Huang and K. K. Lehmann, "Noise in Cavity Ring-Down Spectroscopy Caused by Transverse Mode Coupling," *Optics Express*, vol. 15, pp. 8745-8759, 2007.
- [65] R. D. van Zee, *et al.*, "Pulsed, Single-Mode Cavity Ringdown Spectroscopy," *Applied Optics*, vol. 38, pp. 3951-3960, 1999.
- [66] D. H. Lee, *et al.*, "Optimization of the Mode Matching in Pulsed Cavity Ringdown Spectroscopy by Monitoring Non-degenerate Transverse Mode Beating," *Applied Physics B: Lasers and Optics*, vol. 74, pp. 435-440, 2002.
- [67] R. W. P. Drever, *et al.*, "Laser Phase and Frequency Stabilization Using an Optical Resonator," *Applied Physics B*, vol. 31, 1983.
- [68] R. van Zee and J. P. Looney, *Cavity-Enhanced Spectroscopies* vol. 40: Academic Press, 2002.
- [69] N. J. van Leeuwen, *et al.*, "Periodically Locked Continuous-Wave Cavity Ringdown Spectroscopy," *Applied Optics*, vol. 42, pp. 3670-3677, 2003.
- [70] T. G. Spence, *et al.*, "A Laser-Locked Cavity Ring-Down Spectrometer Employing an Analog Detection Scheme," *Review of Scientific Instruments*, vol. 71, pp. 347-353, 2000.
- [71] National institute of standards and technology atomic spectral database [http://physics.nist.gov/cgi-bin/AtData/main\\_asd](http://physics.nist.gov/cgi-bin/AtData/main_asd), [Online].
- [72] C. J. Hawthorn, *et al.*, "Littrow Configuration Tunable External Cavity Diode Laser with Fixed Direction Output Beam," *Review of Scientific Instruments*, vol. 72, pp. 4477-4479, 2001.
- [73] N. Wongdamnern, *et al.*, "Comparative Studies of Dynamic Hysteresis Responses in Hard and Soft PZT Ceramics," *Ceramics International*, vol. 34, pp. 731-734, 2008.

- [74] A. J. Booth, *et al.*, "Hyperfine Structure Measurements for Lines of Astrophysical Interest in Mn I," *Royal Astronomical Society, Monthly Notices*, vol. 205, pp. 191-205, 1983.
- [75] L. Tao, *et al.*, "Cavity Ring-down Spectroscopy Sensor for Ion Beam Etch Monitoring and End-point Detection of Multilayer Structures," *Review of Scientific Instruments*, vol. 79, Nov 2008.
- [76] Y. Yamamura and H. Tawara, "Energy Dependence of Ion-Induced Sputter Yields from Monatomic Solids at Normal Incidence," *Atomic Data and Nuclear Data Tables*, vol. 62, pp. 149-253, 1996.
- [77] Wee Bee Carbon Fiber Rods Material Properties Comparison, <http://users.hargray.com/weebee/Carbonfiber.html>
- [78] N. Yamamoto, *et al.*, "Sputter Erosion Sensor for Anode Layer-Type Hall Thrusters Using Cavity Ring-Down Spectroscopy," *Journal of Propulsion and Power*, vol. 26, pp. 142-148, Jan-Feb 2010.
- [79] N. Yamamoto, *et al.*, "Development of Real-time Boron Nitride Erosion Monitoring System for Hall Thrusters by Cavity Ring-Down Spectroscopy," *Transactions of the Japan Society for Aeronautical and Space Sciences, Space Technology Japan*, vol. 7, pp. Pb\_1-Pb\_6, 2009.
- [80] B. Rubin, *et al.*, "Total and Differential Sputter Yields of Boron Nitride Measured by Quartz Crystal Microbalance," *Journal of Physics D-Applied Physics*, vol. 42, Oct 2009.
- [81] J. L. Topper, *et al.*, "Preliminary Results of Low Energy Sputter Yields of Boron Nitride due to Xenon Ion Bombardment," AIAA-2008-5092, in *the 44th AIAA/ASME/SAE/ASEE Joint Propulsion Conference and Exhibit*, 2008.
- [82] D. Pagnon and M. Touzeau, "Control of the Ceramic Erosion by Optical Emission Spectroscopy: Parametric Studies of SPT100-ML," in *40th Joint Propulsion Conference*, Fort Lauderdale, FL, 2004.
- [83] E. Vandeweert, *et al.*, "Measurements of the Population Partitions and State-Selected Flight-Time Distributions of keV Ion-Beam-Sputtered Metastable Atoms," *Physical Review B: Condensed Matter and Materials Physics*, vol. 64, 2001.
- [84] R. J. Bartular, *et al.*, "Generation of Ultraviolet Broadband Light in a Single-Mode Fiber," *Applied Physics B: Lasers and Optics*, vol. 84, pp. 395-400, 2006.
- [85] N. Yamamoto, *et al.*, "Single-mode Delivery of 250 nm Light Using a Large Mode Area Photonic Crystal Fiber," *Optics Express*, vol. 17, pp. 16933-16940, 2009.
- [86] A. Bjarklev, *et al.*, "Photonic Crystal Fibers," Kluwer Academic Publishers, Springer, 2003.
- [87] Crystal Fiber, <http://www.nktpotonics.com/files/files/LMA-10-UV-070627.pdf>, [Online].

- [88] N. Mortensen and J. Folkenberg, "Near-Field to Far-Field Transition of Photonic Crystal Fibers: Symmetries and Interference Phenomena," *Optics Express*, vol. 10, pp. 475-481, 2002.
- [89] J. A. Buck, *Fundamentals of Optical Fibers*: Wiley-Interscience, 2004.
- [90] R. Kitamura, *et al.*, "Optical Constants of Silica Glass from Extreme Ultraviolet to Far Infrared at Near Room Temperature," *Applied Optics*, vol. 46, pp. 8118-8133, 2007.
- [91] R. Schenker, *et al.*, "Deep-Ultraviolet Damage to Fused Silica," *Journal of Vacuum Science & Technology B: Microelectronics and Nanometer Structures*, vol. 12, pp. 3275-3279, 1994.
- [92] W. P. Leung, *et al.*, "Effect of Intense and Prolonged 248 nm Pulsed-Laser Irradiation on the Properties of Ultraviolet-Grade Fused Silica," *Applied Physics Letters*, vol. 58, pp. 551-553, 1991.
- [93] R. S. Taylor, *et al.*, "Dependence of the Damage and Transmission Properties of Fused Silica Fibers on the Excimer Wavelength," *Applied Optics*, vol. 27, pp. 3124-3134, 1988.
- [94] *j-Ultrasol Fiber*. <http://www.j-fiber.com/index.php/8ed80fde5a4457444ca1651635e512b6/2/1/download/1326>, [Online].
- [95] E. Aheda, *et al.*, "Simulation of Wall Erosion in Hall Thrusters," IEPC-2007-067, in *the 30th International Electric Propulsion Conference*, Florence, Italy, 2007.
- [96] T. R. Obrian and J. E. Lawler, "Radiative Lifetimes in B-I Using Ultraviolet and Vacuum-Ultraviolet Laser-Induced Fluorescence," *Astronomy and Astrophysics*, vol. 255, pp. 420-426, 1992.
- [97] Y. Ito, *et al.*, "Spectroscopic Measurement of Kinetic Energy of Sputtered Boron in Electron Ccyclotron Resonance Plasma," *Journal of Nuclear Materials*, vol. 241, pp. 1122-1126, 1997.
- [98] E. Scime, *et al.*, "Laser Induced Fluorescence in a Pulsed Argon Plasma," *Review of Scientific Instruments*, vol. 76, 2005.
- [99] M. Stepanova and S. K. Dew, "Estimates of Differential Sputtering Yields for Deposition Applications," *Journal of Vacuum Science & Technology A*, vol. 19, pp. 2805-2816, 2001.
- [100] B. Barbieri, *et al.*, "Optogalvanic Spectroscopy," *Reviews of Modern Physics*, vol. 62, pp. 603-644, 1990.
- [101] J. F. Ziegler. SRIM-2008.04 <http://www.srim.org>, [Online].
- [102] A. Goehlich, *et al.*, "An Experimental Investigation of Angular Resolved Energy Distribution of Atoms Sputtered from Evaporated Aluminum Films," vol. 179. *Nuclear Instruments and Methods in Physics Research B*, 2001, pp. 351-363.
- [103] P. S. Johnston and K. K. Lehmann, "Cavity Enhanced Absorption Spectroscopy Using a Broadband Prism Cavity and a Supercontinuum Source," *Optics Express*, vol. 16, pp. 15013-15023, 2008.

- [104] B. Lee, *et al.*, "Optical Loss Characterization of CaF<sub>2</sub> in the Ultraviolet Region for Prism Retroreflectors," in *Conference on Lasers and Electro Optics*, San Jose, CA, 2010.